FOSSIL ENERGY

DOE/BC/15205-1
(OSTI ID: 790847)

CHARACTERIZATION OF MIXED WETTABILITY AT DIFFERENT SCALES AND ITS IMPACT ON OIL RECOVERY EFFICIENCY

Annual Report
August 4, 2000-August 31, 2001

By:
Mukul M. Sharma
George J. Hirasaki

Date Published: January 2002

Work Performed Under Contract No. DE-AC26-98BC15205

University of Texas at Austin
Austin, Texas

National Energy Technology Laboratory
National Petroleum Technology Office
U.S. DEPARTMENT OF ENERGY
Tulsa, Oklahoma

DOE/BC/15205-1
Distribution Category UC-122

Characterization of Mixed Wettability at Different Scales and Its Impact on Oil Recovery Efficiency

By
Mukul M. Sharma
George J. Hirasaki

January 2002

Work Performed Under DE-AC26-98BC15205

Prepared for
U.S. Department of Energy
Assistant Secretary for Fossil Energy

Purna Halder, Project Manager
National Petroleum Technology Office
P.O. Box 3628
Tulsa, OK 74101

Prepared by
The University of Texas at Austin and
William Marsh Rice University
P.O. Box 7726
CPE2.502
Austin, TX 78713

TABLE OF CONTENTS

LIST OF FIGURES

LIST OF TABLES

EXECUTIVE SUMMARY

1. PROJECT OBJECTIVES

The objectives of the this research project are to:

- Quantify the pore scale mechanisms that determine the wettability state of a reservoir,
- Study the effect of crude oil, brine and mineral compositions in the establishment of mixed wet states,
- Clarify the effect of mixed - wettability on oil displacement efficiency in waterfloods,
- Develop a new tracer technique to measure wettability, fluid distributions, residual saturations and relative permeabilities.
- Develop methods for properly incorporating wettability in up-scaling from pore to core to reservoir scales.

2. PROJECT TASKS

The project tasks are summarized below.

Task 1. Mechanisms of Establishment of Mixed-Wetting States

Task 2: Stability of Wetting Films and its Impact on Mixed Wetting States

Task 3: Effect of Wettability on Displacement Efficiency and Imbibition Behavior

Task 4: Use of Interfacial Tracers to Characterize Mixed Wet States

Task 5: Wettability Up-Scaling

Significant progress has been made in Tasks 1 to 4 and Task 5 which was initiated this year. A summary of the accomplishments for this reporting period and an abstract of each of the chapters in this report is presented below.

3. ACCOMPLISHMENTS

The DOE contract with the University of Texas was signed in August and the subcontract with Rice University was finalized and signed in October 1999. The following accomplishments are noteworthy for this reporting period.

- ✓ An experimental study has been conducted to measure the wettability alteration in marble in presence of cationic surfactant. The objective of the study was to improve the imbibition of brine into carbonate by changing the wettability and reducing the interfacial tension. Alkaline –surfactant flooding can significantly achieve this and in return increase the residual oil recovery.
- ✓ A model for asphaltene precipitation was developed that agrees well with experimental observations on asphaltene solubility. The precipitation of asphaltenes was modeled with the statistical associating fluid theory (SAFT) and impact of asphaltene aggregation on precipitation has been experimentally studied.
- ✓ A SAFT equation of state model was formulated to estimate the phase behavior and interfacial tension of mixtures of associating (polar) molecules. The SAFT equation of state has been integrated into UTCOMP, a compositional reservoir simulator. SAFT has been tested for several binary non-polar and polar mixtures and has been compared with Peng-Robinson equation of state.
- ✓ A manuscript for publication in the Journal of Water Resources Research on "Determination of liquid-liquid interfacial area and relative permeability in glass columns as a function of wetting phase saturation and wettability", has been prepared.
- ✓ Experiments were conducted using interfacial tracers to measure oil/water interfacial areas in porous media (water wet and oil wet glass beads). Interfacial area and relative permeability was measured during primary and secondary drainage cycles.
- ✓ A rock ultra-centrifuge equipped with a video camera to record early time production from centrifuge displacement tests was used to measure drainage and imbibition capillary pressure curves and relative permeabilities.

- ✓ Centrifuge coreflow tests (Berea Sandstone and Texas Cream Limestone) were performed with a range of fluids under different conditions to identify the factors influencing the residual wetting and non-wetting phase saturations and oil recovery.
- ✓ Abstracts on centrifuge research have been submitted for presentation to 7th International Symposium on Reservoir Wettability, 12-14 March 2002, Tasmania, Australia and SPE/DOE, Thirteenth Symposium on Improved Oil Recovery, 13 - 17 April 2002, Tulsa, Oklahoma.
- ✓ Core flood experiments were conducted on Berea sandstone to measure the transient pressure drop during drainage and imbibition in two-phase systems. Decane and 3% brine are used in the experiments. Pressure drop across the cylindrical oil-wet core was measured at different time intervals and the data history-matched by a mathematical model. A comparison of the water-wet and oil-wet pressure drop transients show a difference that can be used to characterize the wettability of a given rock.

4. WETTABILITY ALTERATION IN MARBLE WITH A CATIONIC SURFACTANT

Oil recovery from fractured carbonate formation is challenging because the formation is usually mixed-wet or oil-wet. These wettability conditions tend to make oil recovery by spontaneous imbibition poor. Cationic surfactants have been reported to alter the wettability of carbonate formations to more water-wet conditions and thus enhance spontaneous imbibition. Some wettability and interfacial tension measurements were made for a surfactant system ($C_{12}TAB$) reported in the literature. The wettability was altered by the surfactant but a significant factor in the oil displacement was due to reduction of the interfacial tension.

5. ALKALINE-ANIONIC SURFACTANT SYSTEM FOR FRACTURED CARBONATES

An alkali – anionic surfactant system was formulated to alter wettability and reduce the interfacial tension. Interfacial tension as low as 3×10^{-3} dyne/cm was measured for this system. Oil displacement from a 15-micron gap between a calcite plate and the cell wall was

observed. With brine as the aqueous phase, no displacement occurred. Rapid spontaneous imbibition was observed with the alkaline – anionic surfactant system.

6. PREDICTION OF ASPHALTENE SOLVENCY AND PRECIPITATION

We hypothesize that the asphaltene solvation and precipitation is dominated by van der Waals interactions. If this hypothesis is correct, the solvency of the crude oil for asphaltene can be estimated from the refractive index of the stock tank oil, solution gas/oil ratio, and density. The aggregation behavior and phase separation of asphaltene is investigated with the statistical associating fluid theory. With this model, we can investigate the effect of pressure, temperature, and composition on the aggregation behavior and phase separation of asphaltene.

The precipitation of asphaltenes was modeled with the statistical associating fluid theory (SAFT). The asphaltenes were characterized by data on the precipitation refractive index with different alkanes. Predictions were made with SAFT using other alkanes such as methane to simulate live oil. The onset of asphaltene precipitation for different methane content and pressure occur at nearly the same solubility parameter and refractive index.

7. OBSERVATION OF ASPHALTENE AGGREGATE SIZE NEAR ONSET OF PRECIPITATION

The molecular weight is an important parameter in the solubility of macromolecules. Asphaltene in solution exists as aggregates above some small, critical concentration. Thus one expects that the aggregate size may be an important factor in the onset of precipitation. The aggregate size of asphaltenes in crude oils with added heptane was measured with dynamic light scattering. In one crude oil a rapid increase in aggregate size with time is observed for conditions where aggregates are visible by microscopy.

8. PREDICTION OF BULK AND INTERFACIAL THERMODYNAMIC PROPERTIES OF POLAR MIXTURES BY STATISTICAL ASSOCIATING FLUID THEORY

A general purpose fortran code has been developed which implements a Statistical Associating Fluid Theory (SAFT) model in conjunction with a Rachford-Rice flash

algorithm. The SAFT equation of state has been integrated into UTCOMP, a compositional reservoir simulator. The phase stability and the flash algorithms of UTCOMP are now available with SAFT equation of state. SAFT has been tested for several binary non-polar and polar mixtures and has been compared with Peng-Robinson equation of state. SAFT has been shown to do particularly well for polar mixtures. We have tested SAFT for certain ternary mixtures and we are currently testing several other ternary three-phase systems. In this study we propose to extend some of these recent developments in the theory of hydrogen bonding into thermodynamic models, to predict the bulk and interfacial thermodynamic properties multicomponent mixtures of interest in oil field technology.

9. EFFECT OF WETTABILITY ON DISPLACEMENT EFFICIENCY AND IMBIBITION BEHAVIOR

Oil recovery in petroleum reservoirs is greatly affected by fluid –rock and fluid-fluid interactions. These surface chemical interactions directly control rock wettability, capillary pressure curves and relative permeabilities. Centrifuge coreflow tests (Berea sandstone and Texas Cream limestone) were performed with a range of fluids under different conditions to identify the factors influencing the residual wetting and non-wetting phase saturations and oil recovery. Results of the tests conducted with Prudhoe Bay and Moutray crude oil show that remaining water (S_{wr}) and residual oil saturation vary systematically with Bond number for both sandstone and limestone samples. Differences in the shape of the wetting phase capillary desaturation curves are observed during primary and secondary drainage. This suggests that the distribution of fluids in the rock during secondary drainage is different from primary drainage due to a change in wettability of the core from a water-wet state to mixed-wet state. These trends were not observed with decane. Both limestone and sandstone cores become more susceptible to wettability alteration as the salinity is increased. Aging the samples for 20-30 days with Moutray crude oil results in a change in the wettability of the cores. The results show that with time the crude oil changes the wettability of the core from strongly water wet to mixed wet, which leads to a higher oil recovery.

10. DETERMINATION OF LIQUID-LIQUID INTERFACIAL AREA AND RELATIVE PERMEABILITY AS A FUNCTION OF WETTING PHASE SATURATION AND WETTABILITY

The knowledge of the interfacial area is important to better understand and quantify many flow and transport processes in unsaturated/saturated porous media. The objective of this research was to develop a tracer technique to characterize the wettability of porous mediums over a wide range, by measuring specific liquid-liquid interfacial area. Interfacial tracers can be used to measure the specific oil-water interfacial area in a porous media. Because so little data is available for interfacial area, this research presents a series of experiments with interfacial tracers (compounds that adsorb to the oil/water interface) in order to better define the possible range of interfacial areas over different saturations for varying type (water wet and oil wet) of porous medium. The results indicate that the liquid-liquid interfacial area increases as water saturation decreases. The measurement of the interfacial area includes the area due to the presence of thin films on porous medium. However, thin films were absent during the measurement of interfacial area during primary drainage in oil wet beads and hence the interfacial area reaches a maximum and then decreases at residual water saturation.

11. USING TRANSIENT PRESSURE DROP MEASUREMENTS AS AN INDICATOR OF WETTABILITY

Core flood experiments were conducted on Berea sandstone to measure the transient pressure drop during drainage and imbibition in two-phase systems. Decane and 3% brine are used in the experiments. The pressure drop across water-wet core is measured, as a function of time and the data is history matched by a mathematical model. In the second phase of experiments, pressure drop across the cylindrical oil-wet core is measured at different time intervals and the data is history-matched by a mathematical model. The results of the history-match for both the water-wet and the oil-wet cases show a good fit. The relative permeability to oil and water can be obtained from the pressure drop transient by estimating the model parameters. A comparison of the water-wet and oil-wet pressure drop transients show a difference that can be used to characterize the wettability of a given rock.

1. Wettability Alteration in Marble with a Cationic Surfactant

ABSTRACT

This investigation is to enhance oil recovery in fractured carbonate formation. We present an experimental study of using surfactant $C_{12}TAB$ to change the wettability of a calcite plate. Three kinds of experiments were done to show the wettability alteration of surfactant. Oil film displacement experiments gave a general idea about how efficient and fast oil recovery could became by adding proper surfactants. Advancing contact angle decreased significantly, and contact angle hysteresis almost disappeared. By measuring zeta potential of brine-oil and brine-calcite, an electrostatic interaction explanation was given, as well as quotes from some papers.

INTRODUCTION

Wettability is usually described as the tendency of one fluid to wet a solid surface in the presence of another fluid. Put it in simple words, wettability is the preference of rock to oil or water [13]. In this sense, rock is usually divided into 3 categories: water-wet, intermediate or mix-wet, and oil-wet. If the advancing contact angle is large, whereas the receding contact angle is small, the rock is considered mix-wet. The wetting properties of a reservoir are determined by the interactions between rock and fluids. For a given reservoir, fluid composition, pH and temperature are important factors.

Injection of water into oil reservoirs is an important and inexpensive method to improve the oil recovery. But if fractured reservoirs are oil-wet, spontaneous imbibition of water is not possible. In this case, the injected water will follow the fractures from the injection well to the production well without displacing any significant amount of oil [2].

The MY1 oil we used is from a reservoir in Texas. Gravity drainage is the dominant producing mechanism for the entire field. It is believed to be oil-wet to mix-wet. In order to recover more oil, it may be desirable to alter the wettability of the formation.

Recently, it was demonstrated by laboratory experiments that some surface-active materials added to the brine were able to change the wettability of a rock [2,3,4,5,6,7,8,9,10,11,12]. Both the type and the concentration of the surfactant used are very important. According to Austad et al [11], for nearly oil-wet chalk, spontaneous imbibition of water could be achieved by adding cationic surfactant. Additional oil was also recovered from mixed-wet chalk material using the cationic surfactant $C_{12}TAB$. They thought it was caused by the change in wettability toward a more water-wet state.

The objective of the present paper is to summarize the experimental results aiming to improve the imbibition of brine into carbonate by using the cationic surfactant $C_{12}TAB$.

EXPERIMENTAL SETUP, RESULTS AND DISCUSSION

Materials

Oil: MY1 stock tank oil.

Brine: 0.1M NaCl at two different pH levels: pH 6.5, and pH 9.5 (pH was measured after equilibrium of brine-marble was achieved, and pH6.5 was adjusted by adding HCl).

Surfactant: wt 1% $C_{12}TAB$ in the two different kinds of brines. $C_{12}TAB$: (n-Dodecyl)trimethylamonium Bromide

Carbonate: Marble plate polished by diamond lap. Dimension: 1.2"×0.9"×0.2".

Oil film displacement Oil film displacement experiments were conducted to observe the effectiveness of surfactant in displacing oil.

Procedure:

- Two well-polished an cleaned marble substrates were put in pH6.5 brine, and aged for at least 24 hours at room temperature.
- Cleaning procedure: after contact with oil, use Toluene, then 1-propanol and de ionized water to clean.

- After shaking off brine on the surface, the substrates were put in MY1 crude oil, and aged for 1day and 3 days respectively.
- The substrate aged for 1 day was put in the pH6 brine, and the one for 3 days in 1% wt. C_{12}TAB pH6.5 solution. The experiment set-up was shown in Fig. 1.1.

1) Oil film displacement in brine

The results were shown in Fig. 1.2. Images were taken for 28 hours continuously, and no more change after the last picture. From the pictures, we can see some change, but images changed slowly, and it is believed to be caused by gravity (buoyancy) effect. From the figure, we can see that the oil patches grew blur at their border, from which we can infer that at this condition, advancing contact angle must be greater.

2) Oil film displacement in surfactant

The results were shown in Fig. 1.3. No more change after the last picture. From this figure, we can see that the change was much faster and more dramatic. From the pictures, we can also see that contact angle changed from greater than 90° at first to less than 90° with time going on.

Contact angle of MY1/brine/marble

Procedure [3]:

- Well cleaned and polished marble substrates were put in 2 different brines and the corresponding surfactant solutions, and aged for at least 24 hours at room temperature.
- The aged substrates were put in a glass cell, and advancing and receding contact angle was measured with goniometer (model # 100-00-115). First form a drop of oil against the substrate, then adjusted the microsyringe to make contact line move, once no significant move of contact line (about 5 minutes after) and made advancing and receding contact angle measurements (as shown in Fig. 1.4).

Wettability is usually described quantitatively with contact angle measurements. The larger the advancing contact angle, the more oil-wet the rock is.

The result of contact angle (average) in different solution can be summarized in Table 1.1, from which we can see three trends: 1) for every pH level, the advancing contact angle made with brine is much larger than that made with surfactant, i.e. surfactant $C_{12}TAB$ can significantly reduce the advancing contact angle, and change the rock from oil-wet or mix-wet to much more water-wet. 2) Contact angle hysteresis almost disappears by adding surfactant. 3) In the same surfactant condition (both with and without surfactant), advancing contact angle increases while pH decreases.

Table 1.1. Advancing and receding contact angles on calcite

	pH 6.5		pH 9.5	
	Brine	$C_{12}TAB$	Brine	$C_{12}TAB$
Advancing Angle/°	154	21	74	22
Receding Angle/°	18	20	16	21

Standnes and Austad [2] proposed the following imbibition mechanism of cationic surfactant $C_{12}TAB$, as shown in Fig. 1.5. The figure illustrates a pore, and in the aqueous zone we have surfactant micelles and monomers in equilibrium. Due to electrostatic forces, the cationic monomers will interact with adsorbed anionic materials from the crude oil. The adsorbed material at the interface between oil, water and rock will be desorbed by forming an ion-pair between the cationic surfactant and the negatively charged adsorbed material, mostly carboxylic groups. In addition to electrostatic interactions, the ion-pair is stabilized by hydrophobic interactions. The ion-pair is not soluble in the water phase but it will be dissolved in the micelles. In this way, water will penetrate into the pore system, and oil will be expelled from the core through connected pores with high oil saturation in a so-called counter-current flow mode. The imbibition of water is in fact governed by capillary forces. So, marble becomes much more water-wet by adding the cationic surfactant, and significantly reduces the contact angle hysteresis.

In their paper, Standnes and Austad [2] also mentioned the consumption of the cationic surfactant. Because of $CaCO_3$ dissolution in water, "The loss of cationic surfactant during the wettability alteration process in chalk due to adsorption must by very low provided that the brine contains sufficient amounts of Ca^{2+}."

The explanation of the effect of pH will be discussed in the 4th section.

Sessile drop

Procedure:

- An oil drop was made on a marble plate surrounded by 0.1M brine, as shown in the first picture in Fig. 1.6 (To make the oil drop, force an oil drop was made against marble like in contact angle measurements, then the drop was withdrew, and a small patch of oil was left behind. That is the " original oil drop" we called below). The change of the oil drop was recorded for one hour.
- 2%wt. C12TAB in 0.1M brine of the same volume with the original brine was added into the cell (so that the C12TAB concentration was reduced to 1%wt., and change was recorded.

When the sessile drop was only in brine, nothing happened in an hour. But after surfactant solution was added, as shown in Fig. 1.6, the oil drop changed with time. In about 5 minutes, the most of the oil drop lifted off.

But the question is if the dramatic change happened because of wettability alteration, or reduction of interfacial tension. The diameter of the lifting off oil drop should be about the same as the capillary constant. The interfacial tension (IFT) of brine/MY1 is 12 dyne/cm, while that of 1% C12TAB/MY1 is 0.475 dyne/cm, thus the The diameter of the lifting off oil drop should be about the same as the capillary constant. The interfacial tension (IFT) of brine/MY1 is 12 dyne/cm, while that of 1% C12TAB/MY1 is 0.475 dyne/cm, thus the capillary constants are 0.325cm and 0.090cm respectively. The diameter of the original oil drop was about the same as the diameter of the micro-syringe, which is 0.410cm, so oil did not lift off. But after adding surfactant, the IFT was reduced, and so was the capillary constant. The diameter of the remaining oil

drop is about 0.09cm, similar to the capillary constant with surfactant. So the oil drop may have lifted off due only to the reduction of IFT.

Zeta potential

Procedure:

- After 30 seconds's dispersion using ultrasonic probe, followed by another 20 minutes, zeta potential of brine/MY1, brine/calcite was measured with Delsa 440. The calcite used here is powdered sodium carbonate (certified A.C.S.), and pH was adjusted by HCl or NaOH.

Interfacial electrical properties of the oil/brine and brine/mineral interfaces determine wettability through electrostatic interaction contribution in surface force. By measuring zeta potential at different pH, we can easily explain why the contact angle decreases as pH increases.

The zeta potential of brine/MY1 and brine/calcite at different pH was measured mainly by Anna Tsargorodskaya in our lab, and was drawn in Fig. 1.7. From the figure, we can see that zeta potential of both brine/calcite and brine/Yates oil decreases as pH increases. The iso-electric points of MY1/brine is 2.5, and that of brine/calcite is 8.6. At pH 6.5, zeta potential of brine/MY1 is negative, while that of brine/calcite is positive. Due to the attracting force between surfaces of opposite potential, oil-water interface is attracted to the mineral-water interface. Instability of the water film will result. At pH 9.5, zeta potential of both brine/MY1 and brine/calcite are negative, therefor there'll be repelling forces between the two interfaces, which makes marble more water-wet. Thus, the advancing contact angle at pH 9.5 is expected to be much less than that at pH 6.5.

Thompson and Pownall [16] said "The well-established dependence of the calcite zeta potential on solution pH almost certainly arises from the influence of pH on the solution concentrations of the lattice ions.The formation of new surface material which modifies the physical and electrical properties of calcite crystal surface dispersions."

CONCLUSION

1. At the same pH, adding cationic surfactant $C_{12}TAB$ can change the wettability from oil-wet or mix-wet to much more water-wet, and greatly decrease the advancing contact angle of the system. So adding this kind of cationic surfactant is an effective way for wettability alteration in carbonate formation.
2. Contact angle decreases as pH increases, so does zeta potential, which are caused by electrostatic interaction.
3. Sessile oil drop will lift off by adding C12TAB, but much of it attributes to the reduction of IFT

ACKNOWLEDGEMENT

Anna Tsargorodskaya, who made most zeta potential measurements, and taught me how to use the Delsa apparatus.

REFERENCE

1. Tinker, S. W., and Mruk, D. H., *Reservoir Characterization of a Permian Giant: Yates Field,* West Texas, Marathon Oil Company, 1996.
2. Standnes, D. C., and Austad, T., *Wettability Alteration in Low-permeable Chalk. Mechanism for Wettability Alteration from Oil-wet to Wet-wet Using Surfactants*, 6th International Symposium on Reservoir Wettability and Its Effect on Oil Recovery, Sep, 2000, Socorro, NM.
3. Kowalewski, E., Holt, T., and Torsaeter, O., *Wettability Alterations due to an Oil Soluble Additive*, 6th International Symposium on Reservoir Wettability and Its Effect on Oil Recovery, Sep, 2000, Socorro, NM.

4. Ashayer, R., Grattoni, C. A., and Luckham, P. F., *Wettability Changes due to Surfactant Adsorption*, 6th International Symposium on Reservoir Wettability and Its Effect on Oil Recovery, Sep, 2000, Socorro, NM.

5. Chen, H. L., Lucas, L. R., Nogaret, A. D., Yang, H. D., and Kenyon, D. E., *Laboratory Monitoring of Surfactant Imbibition Using Computerized Tomography,* SPE 59006, 2000.

6. Spinler, E. A., Zornes, D. R., Tobola, D. P., and Moradi-Araghi, A., *Enhancement of Oil Recovery Using a Low concentration of Surfactant to Improve Spontaneous and Forced Imbibition in Chalk*, SPE 59290, 2000.

7. Yang, H. D., and Wadleigh, E. E., *Dilute Surfactant IOR-Design Improvement for Massive, Fractured Carbonate*, SPE 59009, 2000.

8. Austad, T., and Milter, J, *Spontaneous Imbition of water Into Low Permeable chalk at Different Wettabilities Using Surfactants*, SPE 37236, 1997.

9. Michels, A.M., Djojosoeparto, R. S., Haas, H., Mattern, R.B., van der Weg, P. B. and Schulte, W. M., *Enhanced Water Flooding Design Using Dilute Surfactant Concentrations for North Sea Conditions,* SPE/DOE 35372, 1996.

10. Milter, J., and Austad, T., *Chemical Flooding of Oil Reservoirs 6. Evaluation of the Mechanism for Oil Expulsion by Spontaneous Imbibition of Brine with and without Surfactant in Water-wet, Low-permeable, Chalk Material*, Colloids and Surfaces A., 113, (1996), 269-278.

11. Austad, T., Matre, B., Milter, J., Sævareid, A., and yno, L., *Chemical Flooding of Oil Reservoirs 8, Spontaneous Oil Expulsion from Oil- and Water-wet Low Permeable Chalk Material by Imbibition of Aqueous Surfactant Solutions*, Colloids and Surfaces A., 137, (1998), 117-129.

12. Austad, T., Ekrann, S., Fjelde, I., and Taugbøl, K., *Chemical Flooding of Oil Reservoirs 9, Dynamic Adsorption of Surfactant onto sandstone Cores from Injection Water with and without Polymer Present*, Colloids and Surfaces A., 127, (1997), 69-82.

13. Yang, S. S., *Mechanisms of Wettability for Crude Oil/Brine/Mica System*, Ph.D. thesis, 2000.

14. Siffert, B., and Fimbel, P., *A Study of the Parameters Affecting the Sign and Intensity of the Electrokinetic Potential of Calcite*, Collect. Colloq. Semin., Inst. Fr. Pet. 42, (1985), 187-202.

15. Thompson, D. W., Pownall, P. G., Surface Electrical Properties of Calcite, J. Colloid and Interface Sci., 131, (1989), 74-82.

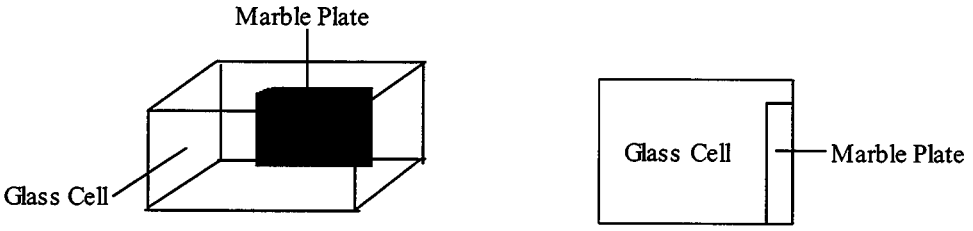

Fig. 1a. Front View

Fig. 1b. Side View

Figure 1.1 Experimental Set-up for Oil Film Drainage

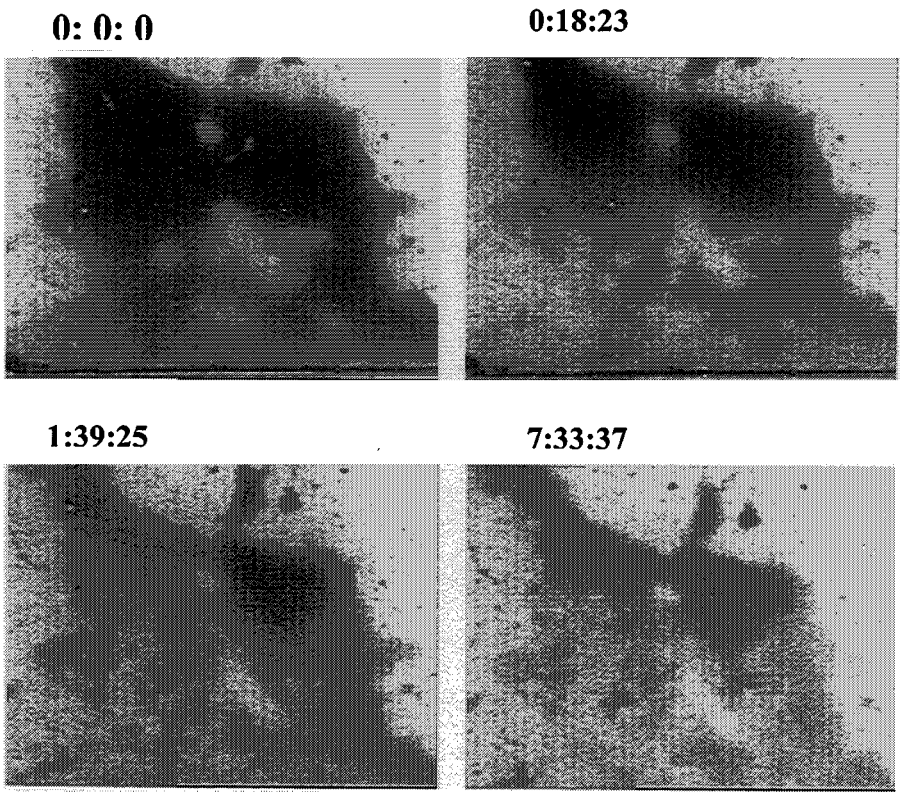

Figure 1.2. Oil Film Displacement in Brine

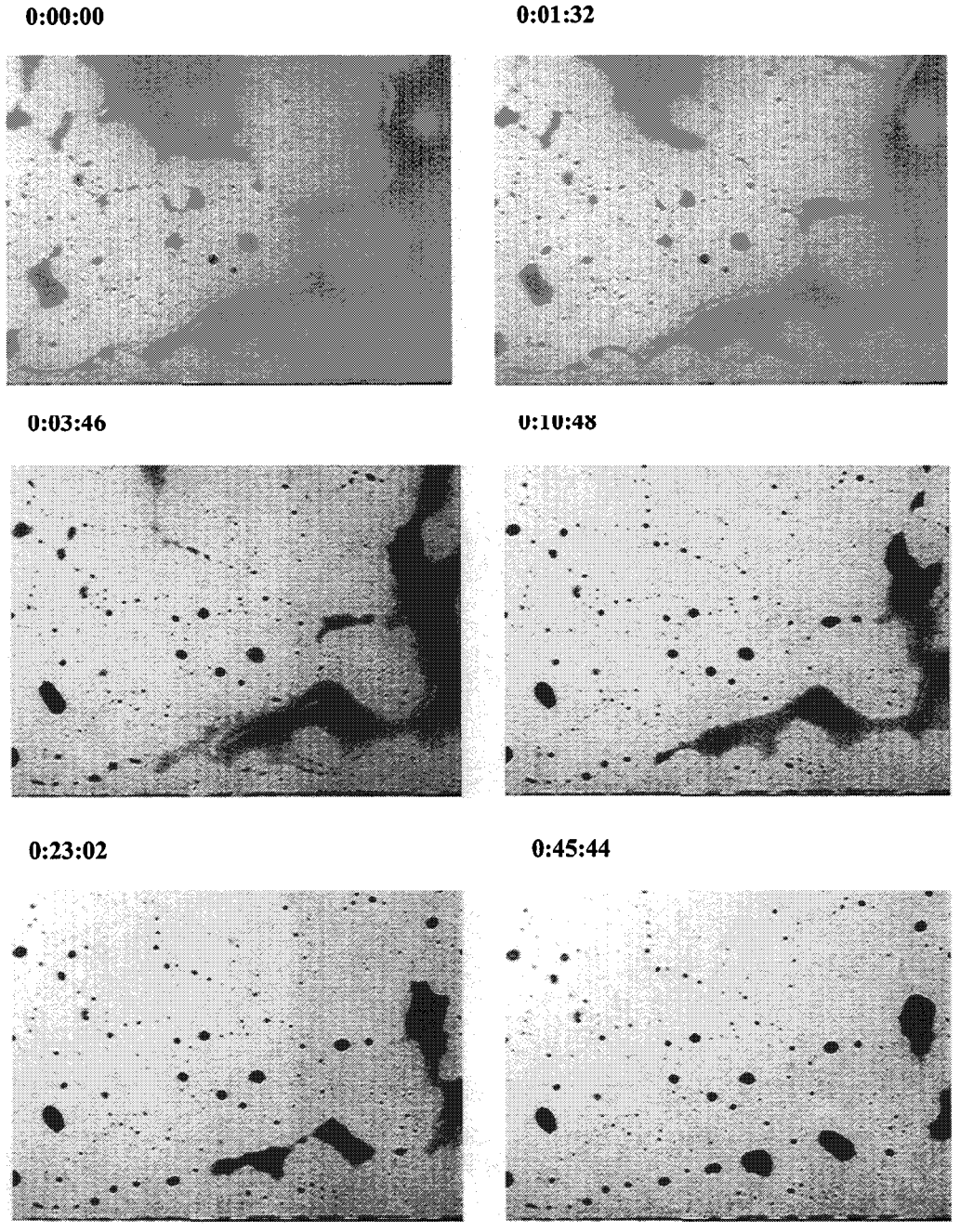

Figure 1.3. Oil Film Displacement in C12TAB

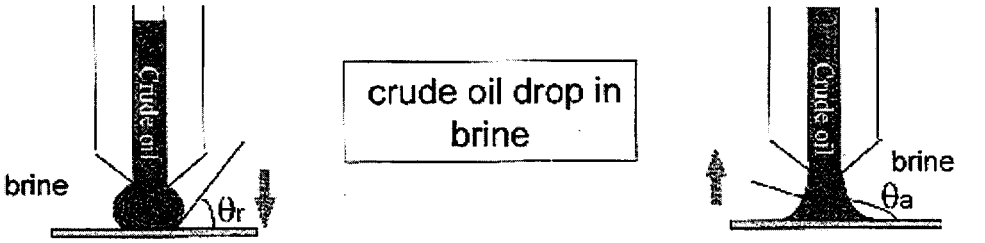

Receding Contact Angle

Advancing Contact Angle

Figure 1.4. Contact Angle Measurement with Crude Oil as Probe Fluid

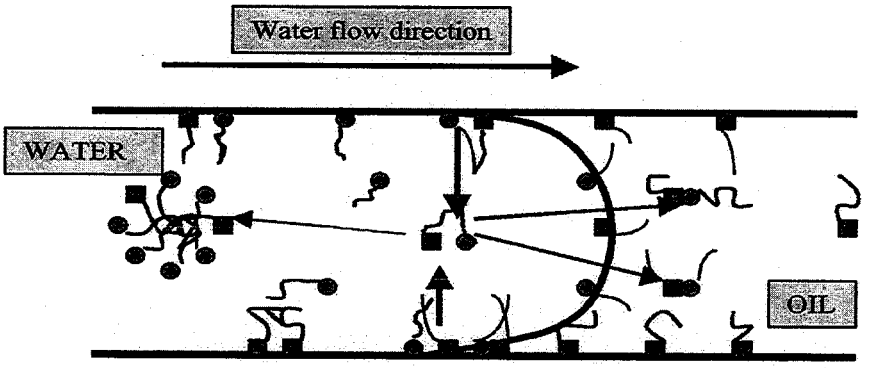

Figure 1.5 Schematic Model of Mechanism for Wettability Alteration Caused by $C_{12}TAB$ in a Pore.

represents cationic surfactant

represents anionic surface active organic materials present in oil

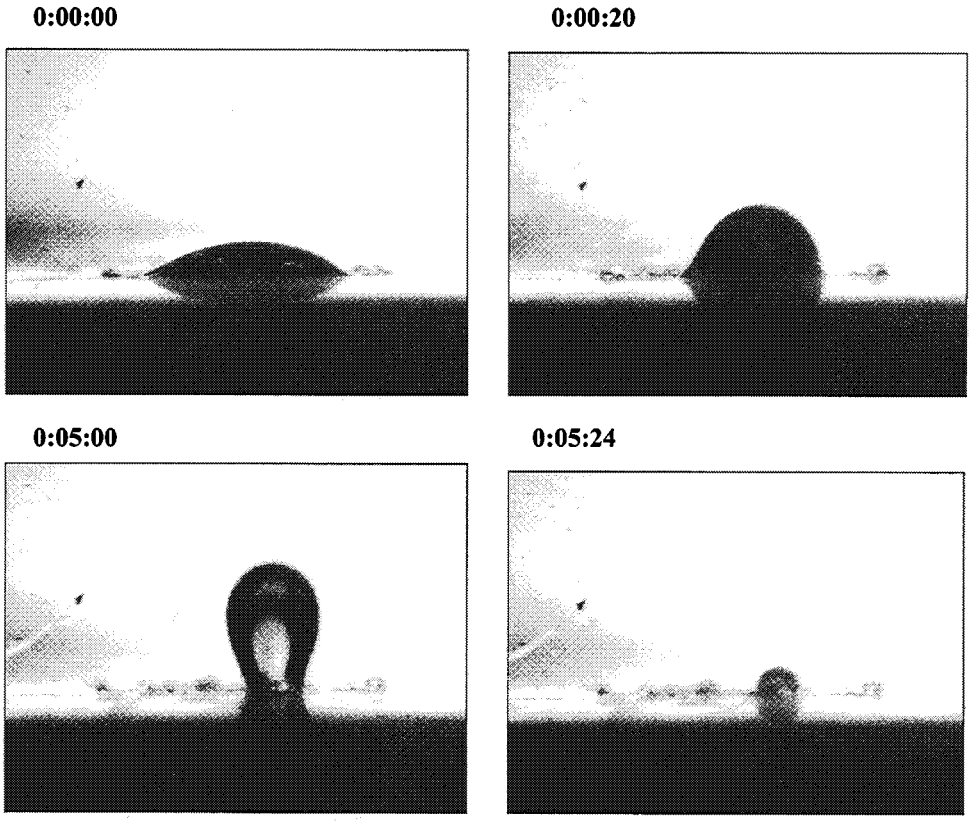

Figure 1.6. Effect of Surfactant C12TAB on Sessile Drop

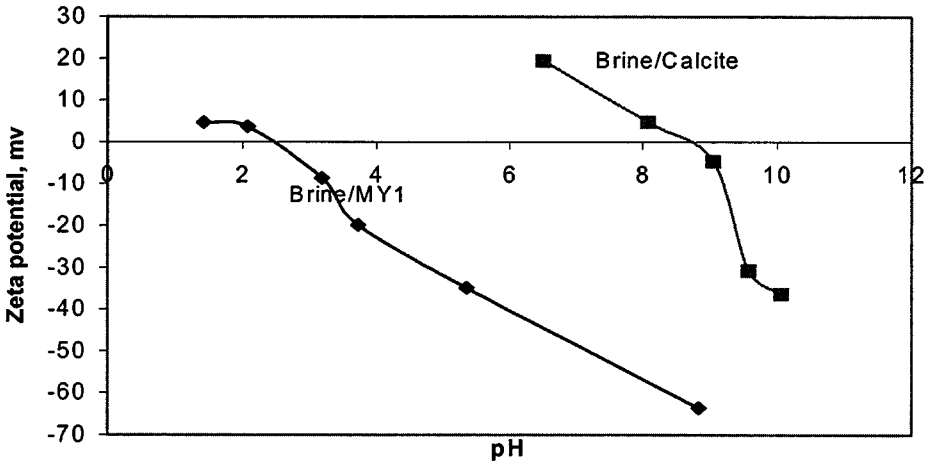

Figure 1.7. Zeta potential of brine/MY1 and brine/calcite

2. Alkaline—Anionic Surfactant System for Fractured Carbonates

ABSTRACT

Alkaline-surfactant flooding can significantly reduce interfacial tension and thus recover residual oil. In this paper three kinds of experiments and their results are described and discussed. By using sodium carbonate and C-330, interfacial tension was reduced by different degree depending on the composition of alkali-surfactant. A calcite plate experiment was done to find that 0.03M sodium carbonate 0.05% active CS-330 could spontaneously imbibe into pores as small as 15 microns. Thus demonstrated that alkaline-surfactant flooding could be a good method for oil recovery.

INTRODUCTION

The objective of alkaline-surfactant flooding is to increase oil recovery by reducing residual oil, which is achieved due to both reduced interfacial tension and wettability reversal. Cationic surfactants [6] can greatly increase oil production by spontaneous imbibition in carbonate formations, but because of the concentration and price of the surfactants, the cost is expensive (eg. 1% C_{12}TAB). Alkaline-surfactant flooding is an alternative way because its cost is low and it is effective.

The practice of alkaline-surfactant flooding can be dated back to Reisberg and Doscher (1956)[1] who used non-ionic surfactants in their experiments. In late 70's and early 80's, there were a number of studies [1,2,3,4] regarding this method because of the high price of oil then. This idea has again become popular [5,7-14] due to the higher oil price now. Alkali-surfactant flooding has been applied to many oil fields, and for many of them, the results were good [5,7-14].

To illustrate the effect of alkaline-surfactant flooding, three kinds of experiments are discussed here.

EXPERIMENTAL SETUP, RESULTS AND DISCUSSION

In this section, three experiments: "emulsion screening test" [1], followed by spinning drop measurements, and calcite plate experiment was described. In all of the experiments, we used crude oil MY1, sodium carbonate as alkali and Stepan's STEOL CS-330 [$CH_3(CH_2)_{10}CH_2(OCH_2CH_2)_3OSO_3Na$] as surfactant. Sodium hydroxide, sodium silicate and sodium carbonate can all be used as alkali, but sodium carbonate is the least expensive, and does the least damage to the mineral, so sodium carbonate is chosen as alkali. In Nelson et al.'s paper [1], there is a detailed discussion about the comparison of several alkalis. All experiments were done under room temperature.

Emulsion screening test This test is used to show phase behavior of mixture of oil and alkali or alkali with surfactant in glass vials. Based on the observation, the optimal alkaline-surfactant composition is found. This method was first used by Stegemier in 1960, and modified by Hill et al. [1]

The procedure of the test is to put alkali or alkali plus surfactant of different composition and equal volume of crude oil in glass vials. The vials are shaken several times a day during the first 2-3 days, then allowed to equilibrate.

We found that the lower phases in the vials went from clear to cloudy and to clear again as sodium carbonate concentration increased (as shown in Fig. 2.1), which means phase behavior went from under-optimum to optimum and at last to near over-optimum. For the experiments with surfactant, the phase behavior has the same trend, but the lower phases were colored, and the optimum sodium carbonate concentration is different (as shown is Fig. 2.2).

From Fig. 2.2, we see that by adding surfactant, the active region moves to that of higher carbonate concentration.

Fig. 2.3 shows change in phase behavior of MY1/0.3M Na_2CO_3 simply by adding different amount of surfactant CS-330.

pH measurements for oil/alkali (Fig. 2.4.) showed that after 0.04M sodium carbonate concentration, the initial and equilibrium pH curve of aqueous phase almost become one, which indicate that alkalinity is enough to react with the acids in the crude oil.

Phase behavior can be changed not only by adding surfactant and electrolyte, but also by changing water/oil ratio (W/O). Figure 2.5 shows the change of phase behavior of MY1/0.3M Na_2CO_3 with decreasing w/o ratio. This tells us that W/O ratio is a very important parameter. In reality, w/o changes continuously with time, which makes the problem more complicated.

Spinning drop measurements Spinning drop is a widely used method for measuring ultra-low interfacial tension. The equilibrated lower and upper phases in the vials were taken to do the experiments.

Through spinning drop measurements, interfacial tension between the upper and lower phase can be plotted as a function of both sodium carbonate concentration and surfactant concentration, as shown in figure 2.6.

The interfacial tension of MY1/ Na_2CO_3 and MY1/Na_2CO_3 and CS-330 is about the same at low carbonate concentration (0-0.2M), but has big difference at higher carbonate concentration. From the curves, we can find out the optimal electrolyte concentration. For the 0.05% C-330 and W/O=1 curve, interfacial tension has a minimum around 0.3M Na_2CO_3concentration. If we hold the carbonate concentration to 0.3M, but change the surfactant concentration, we can also find the optimal surfactant concentration.

Fig. 2.7 shows the change of interfacial tension with C-330 concentration while the concentration of sodium carbonate is fixed (0.3M). The optimal surfactant concentration is around 0.025%. Fig. 2.8 shows the effect of W/O ratio on IFT. At W/O

of 1, the IFT is well below 0.01 dyne/cm, while at W/O of 100, IFT increases more than 10 fold.

Calcite Plate Experiment The experiment is done as an analog to alkaline-surfactant in porous carbonate rock.

A piece of marble plate was aged in crude oil for more than 24 hours. Two small pieces of plastic wrap (Saran Cling Plus), whose thickness is 15 microns, were put on two sides of the front surface of the marble plate as spacers. Then the plate was pressed against the front wall of a glass cell. The cell was coated with C16TAB solution. (The schematic graph of the experiment set-up is shown in Fig. 2.9.) After that, 0.1M NaCl was added in to the cell and video pictures were taken for one hour. Then the brine was replaced with 0.3M Na_2CO_3 with 0.05% active CS-330, and video images are taken until no changes are visible.

When without surfactant, the 15 micron oil film between the calcite plate and glass did not change during one hour of observation (Fig. 2.10), and we do not expect it to change in even much longer time. This is because both the calcite plate and the glass cell wall were oil-wet and the interfacial tension between oil and brine was so large that brine could not spontaneously imbibe into the "pore" (gap between marble and the treated glass wall of the cell, spaced by 15 micron plastic sheet). Thus brine could not displace oil, and the oil film remained unchanged. But once the brine was replaced by 0.05% CS-330, 0.3M Na_2CO_3 solution, the interfacial tension became so low that the aqueous phase spontaneously imbibed into the pore and displaced oil (Fig. 2.11). From the last picture in Fig. 2.11, we see that the oil/aqueous phase contact angle also changed, which means the wettability was altered. In the experiment we also found that in bulk aqueous phase, the displaced oil drops on the top surface of the calcite plate were rather large, which implies that the interfacial tension there was not low. The interfacial tension was probably higher because it is a function of W/O ratio.

In Fig 2.10 and 2.11, the size of the view is about 16mm long, and all the numbers are time, in the form of hour: minute: second.

CONCLUSION

1. By adding sodium carbonate-C330, interfacial tension can be reduced to as low as 0.003 dyne/cm.
2. At 0.05% C-330 concentration, the optimal sodium carbonate concentration is fairly wide, which makes it easy to control.
3. W/O ratio is an important parameter. For W/O is equal to or greater than 1, interfacial tension increases with increasing W/O ratio.
4. By using sodium-C330, oil in a 15 microns gap between a calcite plate and an oil-wet glass can be displaced, which is the result of low interfacial tension and wettability reversal.

REFERENCE

1. Nelson, R. C., Lawson, J. B., Thigpen, D. R., and Stegemeier, G. L., "*Cosurfactant-Enhanced Alkaline Flooding*", SPE/DOE 12672, 1984.
2. Castor, T. P., et al., "*Recovery Mechanisms of Alkaline Flooding*", Surface Phenomena in Enhanced Oil Recovery, shah, D. O. (ed.), Plenum Press, NY, 1981.
3. Jennings, H. Y. Jr., "*A Study of Caustic Solution-Crude Oil Interfacial Tensions*", Soc. Pet. Eng. J. 197-202, June 1975.
4. Johnson, C. E. Jr., "*Status of Caustic and Emulsion methods*", SPE 5561, 1975.
5. Vargo, et al., *"Alkaline-Surfactant-Polymer Flooding of the Cambridge Minnelusa Field*", SPE 55633.
6. Standnes, D. C., and Austad, T., "*Wettability Alteration in Low-Permeable chalk. Mechanism for Wettability Alteration from Oil-wet to Water-Wet Using Surfactants*", 6th International Symposium on Reservoir Wettability and its Effect on Oil Recovery, 27-28 September 2000, Socorro, NM.
7. Gu, Hongjun, et al., "*Study on Reservoir Engineering: ASP Flooding Pilot Test in Karamay Oilfield*", SPE 50918, 1998.

8. Qiao, Q., et al., "*The Pilot Test of ASP Combination Flooding in Karamay Oil Field*", SPE 64726, 2000.

9. Gao, S., et al., "Alkaline/Surfactant/Polymer Pilot Performance of the West Central Saertu, Daqing Oil Field", SPE Reservoir Engineering, 1996.

10. Wang, D., et al, "An Alkaline Bio-Surfactant Polymer Flooding Pilots in Daqing Oil Field", SPE 57304, 1999.

11. Wang, D., et al, "Summary of ASP Pilots in Daqing Oil Field", SPE 57288, 1999.

12. Qu, Z., et al, "A Successful ASP Flooding Pilot in Gudong Oil Field", SPE 39613, 1998.

13. Delshad, M., et al, " Alkaline/Surfactant/Polymer Flood Predictions for the Karamay Oil Field", SPE 39610, 1998.

14. Wang, C., et al, "Application and Design of Alkaline-Surfactant-Polymer System to Close Well Spacing Pilot Gudong Oilfield", SPE 38321, 1997.

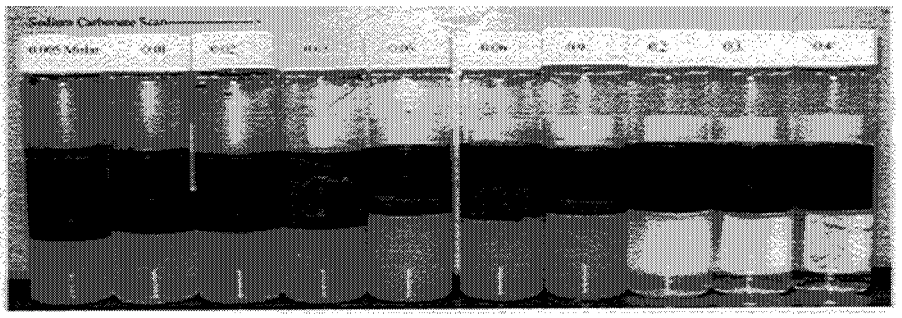

Figure 2.1. Phase Behavior of MY1/Na_2CO_3
(All numbers on vials are sodium carbonate concentration, unit: M[mole/liter])

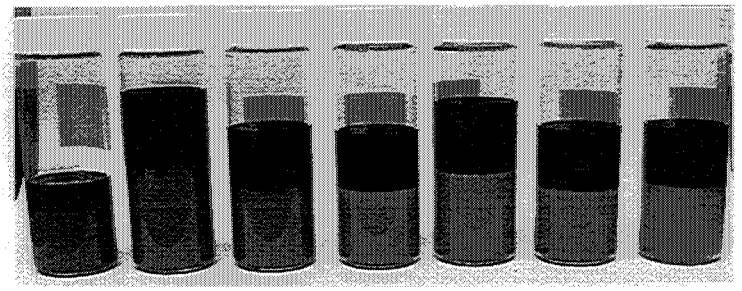

0.08 0.12 0.15 0.20 0.25 0.30 0.40

Figure 2.2. Phase Behavior of MY1/Na_2CO_3 at 0.05% CS-330

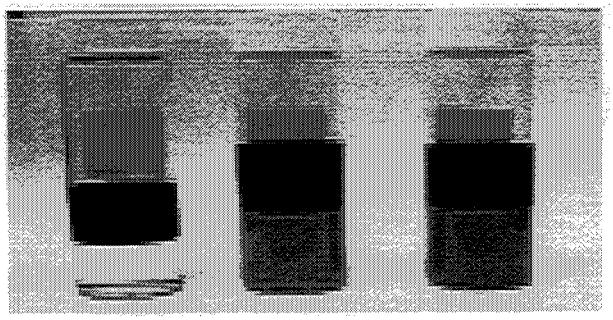

0 0.05% 0.1%

Figure 2.3. Phase Behavior of MY1/0.3MNa_2CO_3 with increasing CS-

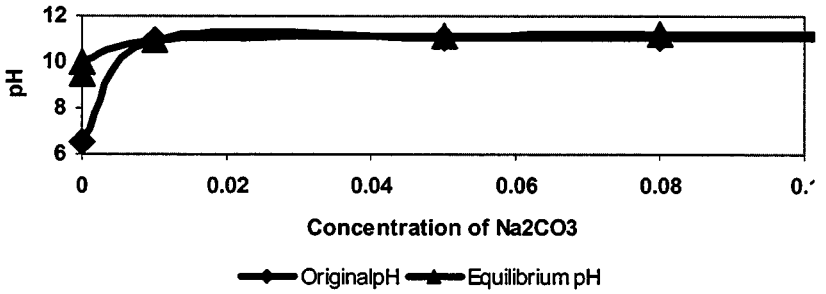

Figure 2. 4. pH change of Aqueous Phase

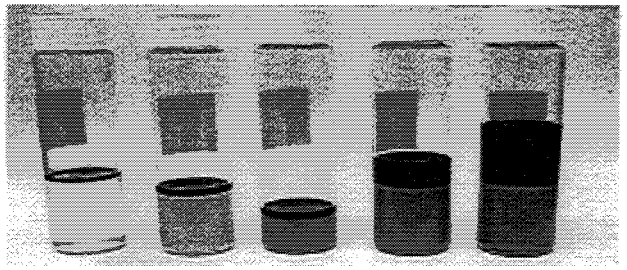

Figure 2.5. Phase behavior of MY1/0.3M Na_2CO_3 with decreasing W/O ratio

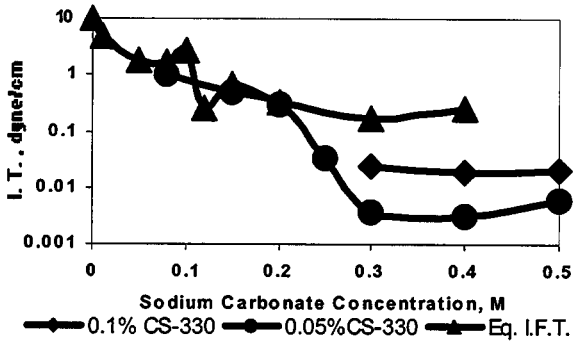

Figure 2.6. IFT of MY1/ Na_2CO_3 or Na_2CO_3 and CS-330, W/O=1:1

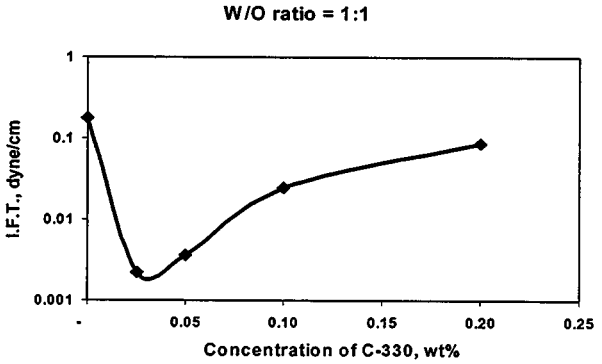

Figure 2.7. Interfacial Tension of MY1/0.3M Na_2CO_3 with increasing CS-330 concentration

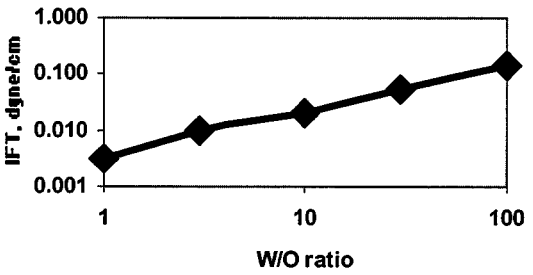

Figure 2.8. Interfacial Tension of MY1/0.3M Na_2CO_3 with increasing W/O ratio

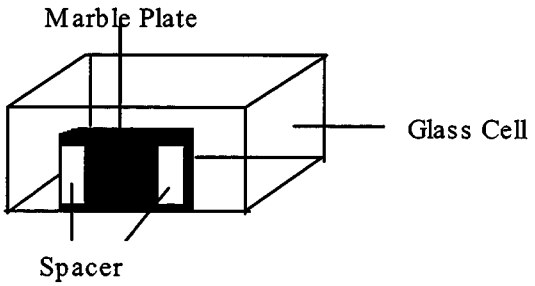

Figure 2.9a. Front View

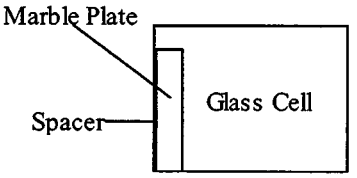

Figure 2.9b. Side View

Figure 2.9. Schematic Setup of Marble Plate Experiment

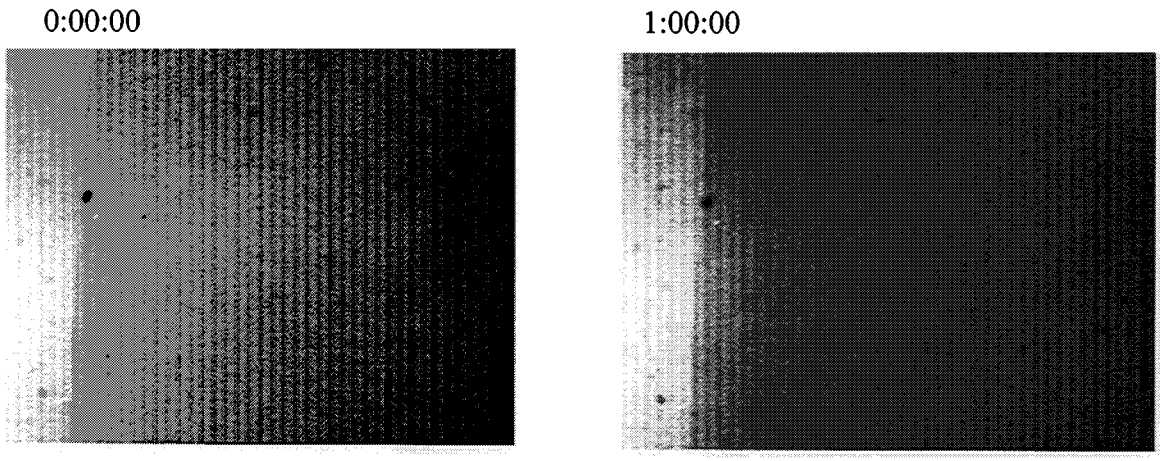

Figure 2.10. Oil Film in brine

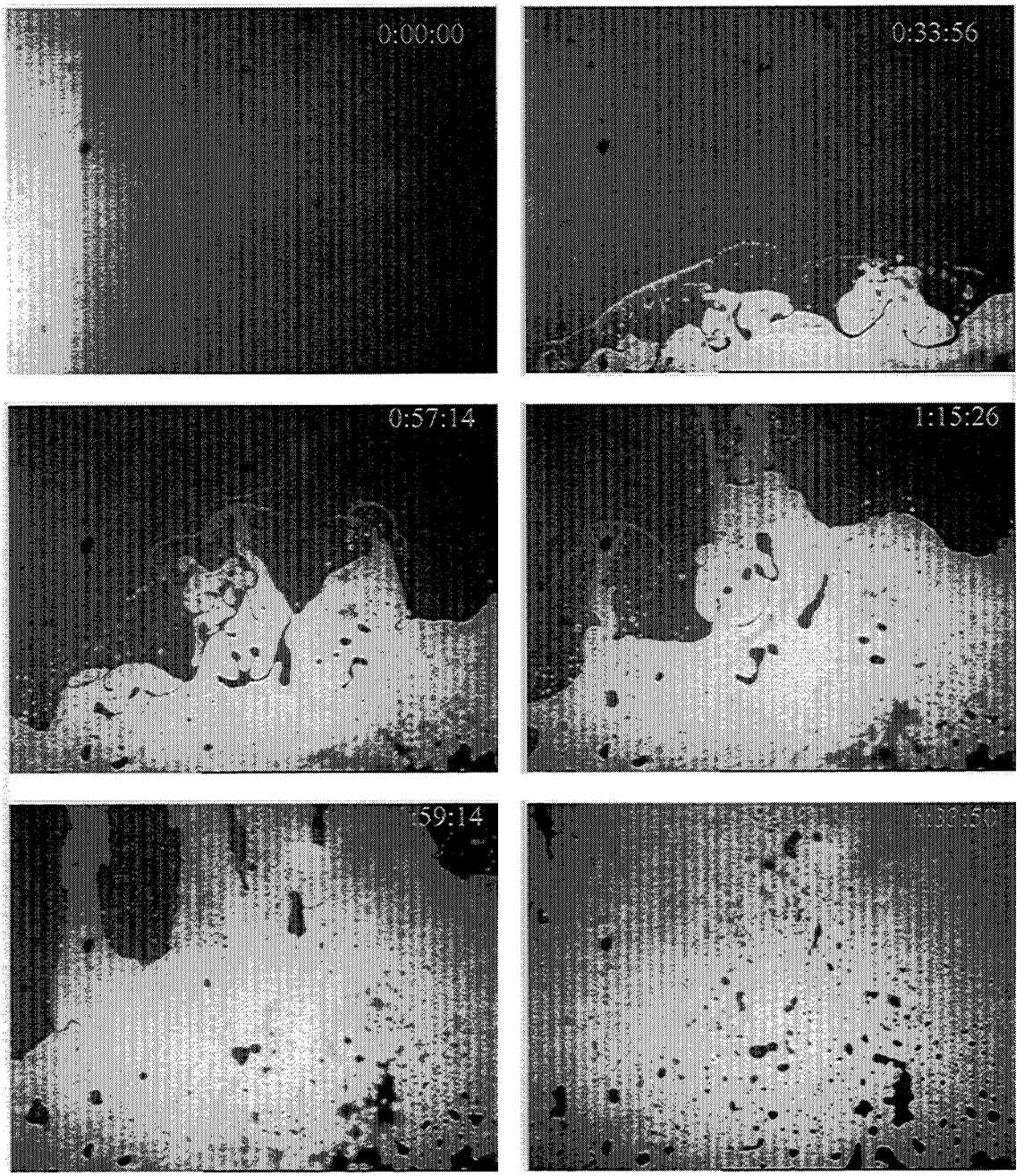

Figure 2.11. Oil displacement in alkali-surfactant solution

3. PREDICTION OF ASPHALTENE SOLVENCY AND PRECIPITATION

ASPHALTENE CHARACTERISTICS AND PHASE BEHAVIOR

Asphaltenes are a collection of polydisperse molecules consisting mostly of polynuclear aromatics with varying proportions of aliphatic and alicyclic moieties and small amounts of heteroatoms (oxygen, nitrogen, sulfur, vanadium, etc.). Most asphaltenes have solubility parameters between 19 and 24 $MPa^{0.5}$ (Hirschberg, *et. al.* 1984; Burke, *et.al.*, 1988; Speight and Plancher, 1991; Wiehe, 1996; Wang, 2000) and mass densities of between 1.13 and 1.20 g/mL at room conditions (Wang, 2000). Problems of asphaltene flocculation and deposition in recovery and refining operations are due primarily to their molecular size and self-aggregation. Asphaltenes can associate into aggregates with changes in crude temperature, pressure, and composition and isolated asphaltenes may exist as colloidal aggregates even in very good solvents. Because of this, molecular weights from as low as 500 and higher than 100,000 g/mol have been reported. (Wang, 2000)

Field experiences show that pressure contribution to asphaltene flocculation is most pronounced for light oil just above the bubble point. Asphaltenes are usually stable in highly undersaturated crude oils because of increasing asphaltene solubility with density due to the high pressure. And at low pressures, asphaltenes tend to be stable because most of the precipitants (i.e. methane and ethane) are vapor at lower pressures and hence escaped from the liquid phase. Compositional changes that drastically alter the oil mass density and polarizability result in asphaltene precipitation (i.e. addition of known asphaltene precipitants), while addition of species similar in polarizability disturb the system only minimally. The effect of temperature on asphaltene flocculation is much less pronounced than that of pressure and composition. Conflicting behavior from temperature information alone are often observed.

APPROACH & HYPOTHESIS

The basis of our approach is the hypothesis that van der Waals (nonpolar) interactions dominate asphaltene aggregation. This hypothesis is supported both by the

molecular structures of representative asphaltenes and by solubility measurements that polar interaction models cannot explain. For example, the contrasting solvating and precipitation behaviors of non-polar molecules such as carbon disulfide/carbon dioxide and toluene/heptane, and solubility parameter mapping studies (Wiehe and Liang, 1996) all point to the importance of van der Waals interactions in determining asphaltene phase behavior.

Currently, both the micellar and the classical thermodynamics approaches are used to model asphaltenes, albeit with limited success due to limitations in the theories. (Hirschberg, 1984; Burke, *et al.*, 1990; MacMillan, *et al.*, 1995; Wang, 2000; Leontaritis and Mansoori, 1987, 1989; Pan and Firoozabadi, 1998; Prausnitz, Lichtenthaler, and de Azevedo, 1999) The micellar models (including the various fractal aggregation and steric colloidal models) are limited by the assumption that asphaltene-resin polar interactions dominate asphaltene precipitation. The classical models (i.e. Flory-Huggins-regular-solution and cubic equation of states models) assume that van der Waals interaction dominate asphaltene behavior but are limited by other constraints in the theories. For instance the cubic equations of state cannot reproduce accurately the phase behavior of systems with large molecular size disparities. Flory-Huggins-regular-solution theory cannot easily reproduce certain classes of phase behaviors and may be difficult to extend to reservoir conditions.

We will model the thermodynamic behavior of asphaltenes using Statistical Associating Fluid Theory (SAFT). More specifically, we will first investigate its phase behavior using preassociated monodisperse asphaltene particles as our fundamental unit and then include the effects of polydispersity and asphaltene association. There is strong evidence that a certain degree of association has already taken place in the reservoir and hence most asphaltenes exist as small associated particles even in their native environment.

STATISTICAL ASSOCIATING FLUID THEORY & SAFT CORRELATIONS

SAFT is a statistical mechanical equation of state (EOS) based on a first order perturbation of the Helmholtz free energy A about a spherical reference fluid. (Wertheim, 1986, 1987; Joslin, *et. al.* 1987; Chapman, Jackson, and Gubbins, 1988; Jackson,

Chapman, and Gubbins, 1988; Chapman, et. al. 1990) It has a similar form to group contribution theories in that the fluid of interest is initially considered to be a mixture of independent segments that are bonded to form chains. The change in free energy due to bonding these segments to form chain-like molecules and the change in free energy due to association of molecules is predicted by the SAFT approach (Figure. 3.1). The dispersion interactions between molecules are calculated using a perturbation theory. In the SAFT framework, asphaltenes are modeled as chains of spheres in a fluid populated by other spheres/chains (of various sizes) representing other crude oil components. Since a first order perturbation on the chain formation is used, SAFT does not allow the formation of ring structures (only branched chains).

The Huang and Radosz (HRSAFT; 1990, 1991) formulation of SAFT was used in our earlier works while the Gross and Sadowski (PCSAFT; 2001) formulation of SAFT is used in current investigations. Both approaches use the same chain, association, and hard sphere contribution to the free energy. Whereas hard-sphere molecules serve as the reference for the perturbation theory used to calculate the dispersion contribution in HRSAFT, hard-chain molecules serve as the reference used to calculate the dispersion contribution in PCSAFT. In mixtures containing alkanes, PCSAFT in general performs quantitatively better than HRSAFT. The two approaches give qualitatively similar results. Unless stated otherwise, in this report, comments and references to SAFT pertain to both PCSAFT and HRSAFT.

In SAFT (both HRSAFT and PCSAFT), three parameters are required for each non-associating species. These correspond to the segment volume (v^{00}), the segment dispersion energy (u^0/k), and the number of segments in a molecule (m). For associating species, two additional parameters analogous to association strength (ε) and association volume (κ) are needed. Pure component parameters correlations exist in both approaches that allow us to extrapolate component parameters without much thermodynamic data. (Huang and Radosz, 1990; Gross and Sadowski, 2001) Figure 3.2 shows plots of HRSAFT parameters as functions of molecular weight for n-alkanes and polynuclear aromatics. Similar relationships are found for PCSAFT parameters. Species with both aromatic and aliphatic characteristics lie in between the aromatic and n-alkane curves in a

systematic manner dependent on their degrees of aromaticity. These correlations will be used to extrapolate SAFT parameters for asphaltenes and for our model oils.

To obtain accurate mixture behavior, an EOS should give the correct pure component solubility parameters and densities (they play important roles in determining mixture partitioning). A comparison between calculated and experimental solubility parameters for various classes of compounds at 298K and 1 bar (Figure 3.3) shows that SAFT (both PCSAFT and HRSAFT) reproduces pure component solubility parameters well. A comparison between SAFT, Peng-Robinson EOS, and experimental densities for n-alkanes from dodecane to hexatriacontane (Figure 3.4) at 372K and 1 bar shows that SAFT reproduces component liquid densities very well in the investigated size range. Although volume translation techniques can be used to improve a cubic EOS's fits to liquid densities, they do not affect fugacity calculations and hence do not affect phase equilibrium calculations.

MODEL SYSTEMS INVESTIGATIONS

An equation of state used in asphaltene phase behavior modeling should be able to take into account the effects of size and aromaticity on mixture phase behaviors. The effects of asphaltene size on solubility are investigated first via the behavior of various molecular weight polystyrenes in hexane (Figure 3.5) and in toluene and ethane (Figure 3.6). Polystyrene is used as a nonassociating model compound because it shares structural similarities (i.e. aromaticity and size) with asphaltenes and interacts mainly through dispersion forces. From Figure 3.5, we see that HRSAFT correctly predicts the pressure and molecular weight effects. As the molecular weight of the polymer increases, so does the size of the two phase region. And at a given temperature, pressure increases would eventually move the system from a two phase region into a one phase region due to density effects. The peculiar temperature dependency (i.e. for a fixed pressure, lowering system temperature may sometimes move the mixture from a two phase to a one phase and then back to a two phase region) may explain some conflicting field observations on temperature effects.

Using a ternary mixture of polystyrene (model asphaltene) in toluene and ethane (Figure 3.6), we further observe qualitatively the pressure dependent separation of the

mixture into a polymer rich and a polymer lean phase. The minor phase that forms upon phase separation depends on the system concentration relative to the plait point. For asphaltene concentrations above the plaint point concentration, the minor phase is asphaltene lean. For low asphaltene concentration (below the plait point concentration), the minor phase is asphaltene rich. This indicates that oils with low asphaltene content are the best candidates of forming an asphaltene-rich phase.

A phenanthrene-decane-methane ternary system is used to test SAFT's ability to model the behavior of mixtures containing polynuclear aromatics, methane, and n-alkane (much like a model oil). Phenanthrene is a three-ring condensed aromatic compound similar to the cores of several proposed asphaltene structural models. In Figure 3.7, the composition of the solid-liquid-vapor (SLVE) coexisting points at various temperatures (350K to 362K) and three isobars (20, 40, and 60 atm.) are compared to experiment results given in Jacoby (1984). Once the temperature and pressure are fixed for this system, there is no more degree of freedom for SLVE (solid phenanthrene properties are obtained from literature data). Hence any initial composition inside the triangle vertices given by pure phenanthrene (100% phenanthrene), almost pure methane (>99.7% in all tested temperatures and pressures) and the shown SLV point would phase split into three coexisting phases with compositions given by these triangle vertices. All binary interaction parameters except that between phenanthrene and decane are obtained from vapor-liquid equilibrium (VLE) data. Because VLE data are not available for the phenanthrene-decane pair, their binary interaction parameter (0.012) was fitted to the SLVE point at 350K and 60 atm. As shown, PCSAFT captures the phase behavior of this polynuclear-aromatics containing SLV system very well.

SAFT ASPHALTENE CHARACTERIZATION

Since pressure-volume-temperature data are not available for asphaltenes, we will characterize the asphaltene SAFT parameters (for a monodisperse asphaltene) using its distinct precipitating refractive index (PRI) data. Essentially, asphaltene-toluene-precipitant ternary phase diagrams are generated at a given pressure and temperature. The phase split onset compositions and densities for a 1% (mass) asphaltene in toluene mixture are then used to calculate the mixture PRI. SAFT asphaltene parameters are

varied to reproduce experimental PRI data (Figure 3.8), with the binary interaction parameters set to zero between asphaltene and all other components and to a temperature independent universal value of 0.015 between toluene and all precipitants. The molecular weight of the asphaltene particles is assumed to be 3,000 for all oil sources. The calculated asphaltene parameters for three oils are given in Table 3.1.

From Figure 3.8, we see that HRSAFT adequately reproduces experimental PRI information. Calculated asphaltene densities (Table 3.1) agree well with experimental densities for these three asphaltenes. Furthermore, the calculated solubility parameters are within the range of asphaltene solubility parameters given in literature. It is interesting to note that the optimal HRSAFT parameters show that Tensleep n-C_7 asphaltene is structurally more aromatic and bulky than A95 n-C_7 asphaltene (which is less aromatic and consists of smaller diameter but longer chains). Since we assume a constant molecular weight of 3,000 for all the asphaltenes tested, aromaticity and molecular "bulk" can be gauged by examining the SAFT parameters' relative positions to the alkane and polynuclear aromatics' segment energy, segment number, and segment volume correlation curves.

A plot of SAFT predicted Tensleep asphaltene (1 % mass in α-methyl-naphthalene) PRI is compared with experimental PRI data in Figure 3.9. The agreement between the predicted and experimental PRIs are quite good, considering that a universal binary interaction parameter of zero was used between asphaltene and all other species and a single binary interaction parameter of 0.015 was used between all precipitants and α-methyl-naphthalene.

SAFT PREDICTIONS IN LIVE OIL SYSTEMS

To investigate asphaltene phase behavior under reservoir conditions, we used a methane-toluene-asphaltene system as our model "live oil". The global phase diagram of the methane-toluene binary system is shown in Figure 3.10 and was calculated with HRSAFT using a single temperature independent binary interaction parameter of 0.126. The methane-toluene-asphaltene isotherm of a monodisperse Tensleep asphaltene (1% mass in toluene) at 350K is shown in Figure 3.11. At this typical reservoir temperature,

three zones can be identified: a one-phase stable region, a region of liquid-liquid asphaltene instability, and a region of vapor-liquid instability.

In highly undersaturated conditions, the asphaltene-toluene-methane mixture exists as a one phase fluid. As pressure decreases (i.e. during reservoir depressurization at constant composition), the mixture will eventually split into a liquid asphaltene poor phase and an asphaltene rich phase (see Figure 3.11). Further depressurization brings the system to its bubble point, at which point vapor-liquid instability occurs and methane begins to bubble out of the mixture. Upon further depressurization, asphaltene would become stable again in the liquid as enough methane vaporizes. A plot of the mixture RI and solubility parameter during this depressurization process is shown in Figure 3.12. The initial decrease in mixture solubility parameter (and RI) with depressurization and the subsequent increase in solubility parameter (and RI) at pressures below the bubble point are as expected.

An analysis of the mixture RI and solubility parameter along the liquid-liquid asphaltene instability curve (Figures 3.13 & 3.11) reveals some interesting behaviors. The mixture solubility parameter (and RI) is essentially constant along this curve, signifying that the onset of asphaltene precipitation occurs at a constant solubility parameter (or RI) for this "oil" at constant temperature. When composition and/or densities are changed (at constant temperature), our predicted mixture will be stable as long as the solution is above a certain solubility parameter threshold.

CONCLUSIONS & CURRENT WORK

The strength of the SAFT equation of state (with either dispersion term) lies in its ability to successfully model mixtures with large structural and size disparities. SAFT has well defined parameter correlation for different classes of compounds and has been shown to reproduce pure component properties well. We investigated the effects of size on solubility using polystyrene as our model asphaltene in mixtures of hexane and toluene/ethane. A ternary mixture of phenanthrene-decane-methane was used to test SAFT's ability to model the behavior of polynuclear aromatics. In all three cases, SAFT models the phase behaviors of these "asphaltene" model systems well.

We have shown that SAFT can model the distinct PRI behavior of extracted asphaltenes in toluene/n-alkane mixtures. Since liquid densities and vapor pressures information are not available, PRI can be used to fit asphaltene's SAFT parameters. Using asphaltene parameters fitted to toluene/n-alkane PRI data, SAFT is able to predict its behavior in mixtures of alpha-methyl-naphthalene and n-alkane. Furthermore, the phase behavior of a model live oil (methane, toluene, and asphaltenes) calculated using these asphaltene parameters agrees well qualitatively with experimental observations. These calculations show the effects of changing system solubility parameter (via changes in composition and/or density) on asphaltene stability.

We are currently measuring the asphaltene stability boundaries for a model "live" oil (asphaltene-toluene-methane) as a function of pressure, temperature, and methane concentrations. The measured asphaltene phase behavior will be compared with SAFT predictions described above to test the validity of our approach.

REFERENCES

Barton, A.F.M. Handbook of Solubility Parameters and Other Cohesion Parameters, 2nd ed. CRC Press. USA (1991).

Burke, N.E., *et. al.* 63rd Annual Technical Conference and Exhibition of the SPE. Houston, TX. Oct. 2-5, 1988.

Burke, N.E, Hobbs, R.D., and Kashou, S.F. *JPT* (1990) 1440-1446.

Chapman, W.G., Jackson, G., and Gubbins, K.E. *Mol. Phys.* 65(1988), 1057-1079.

Chapman, W.G., *et. al. Ind. Eng. Chem. Res.* 29(1990), 1709-1721.

Gross, J. and Sadowski, G. *Ind. Eng. Chem. Res.* 40(2001), 1244-1260

Hirschberg, A., *et. al. SPE Journal.* (June 1984), 283-293.

Huang, S.H. and Radosz, M. *Ind. Eng. Chem. Res.* 29(1990), 2284-2294.

Huang, S.H. and Radosz, M. *Ind. Eng. Chem. Res.* 30(1991), 1994-2005.

Jackson, G., Chapman, W.G., and Gubbins, K.E. *Mol. Phys.* 65(1988), 1-31.

Jacoby, R.H.: "Phase Behavior of Heavy Oils with Application to Reservoir Recovery Process." in *Heavy Crude Oil Recovery*. edited by Okander, E. NATO ASI Series 76, 1984.

Joslin, C.G., *et. al.*: *Mol. Phys.* 62 (1987), 843-860.

Kiran, E. and Xiong, Y.: *Polymer.* 38(1997), 5185.

Leontaritis, K.J. and Mansoori, G.A. SPE International Symposium on Oilfield Chemistry. San Antonio, TX. Feb. 4-5, 1987.

Lin, H.M., *et. al.*: *J. Chem. Eng. Data.* 24 (1979), 146-149.

MacMillan, D.J., *et. al.*: SPE International Symposium on Oilfield Chemistry. San Antonio, TX. Feb. 14-17, 1995.

Pan, H. and Firoozabadi, A. ATCE. Denver, CO. Oct. 6-9, 1996.

Prausnitz, J.M., Lichtenthaler, R.N., and de Azevedo, E.G.: Molecular Thermodynamics of Fluid-Phase Equilibria. Prentice Hall Inc. New Jersey (1999).

Speight, J.G. and Plancher, H. *Proceedings of the International Symposium on the Chemistry of Bitumens* (1991), 154.

Wang, J. *Predicting Asphaltene Flocculation in Crude Oils.* Thesis. New Mexico Institute of Mining & Technology (2000).

Wertheim, M.S. *J. Stat. Phys.* 42 (1986), 459, 477.

Wertheim, M.S. *J. Chem. Phys.* 85 (1986), 2929.

Wertheim, M.S. *J. Chem. Phys.* 87 (1987), 7323.

Wiehe, I.A. *Fuel Sci. & Tech. Int'l.* 14 (1996), 289-312.

Wiehe, I.A. and Liang, K.S. *Fluid Phase Equilibria.* 117(1996), 201-210.

Xiong, Y. and Kiran, E. *Polymer.* 38 (1997), 5185-5193.

TABLES

Table 3.1. HRSAFT asphaltene parameters for Lagrave, Tensleep, and A95 n-C_7 asphaltenes. Experimental densities obtained from Wang (2000).

Source	SAFT Properties			SAFT Calculated Properties		
	m	v00	u0	Density (g/mL)	Solubility Param ($MPA^{0.5}$)	Exp. Density (g/mL)
Tensleep	85	19	408	1.15	23.9	1.16
Lagrave	85	19	400	1.15	23.6	1.17
A95	95	17	362	1.13	23.2	1.12

FIGURES

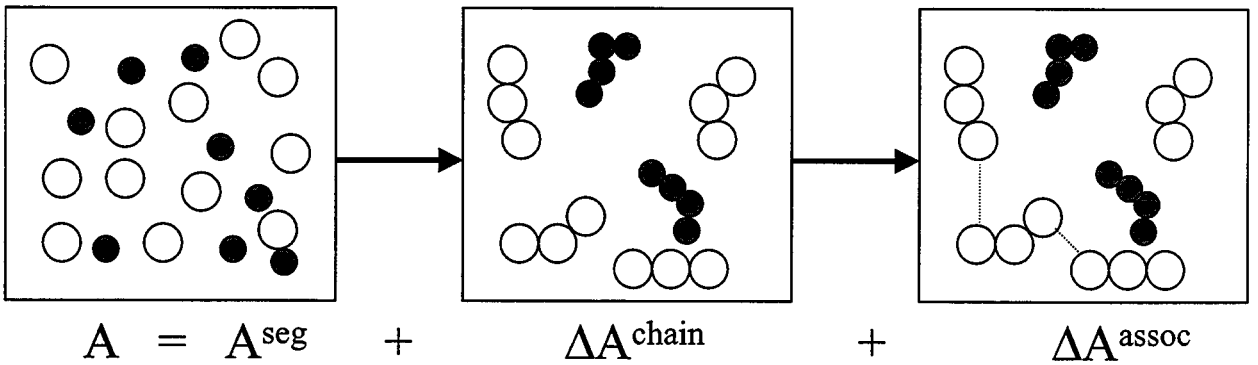

Figure 3.1. In SAFT, fluids are initially considered to be a mixture of independent segments which are then bonded to form chains.

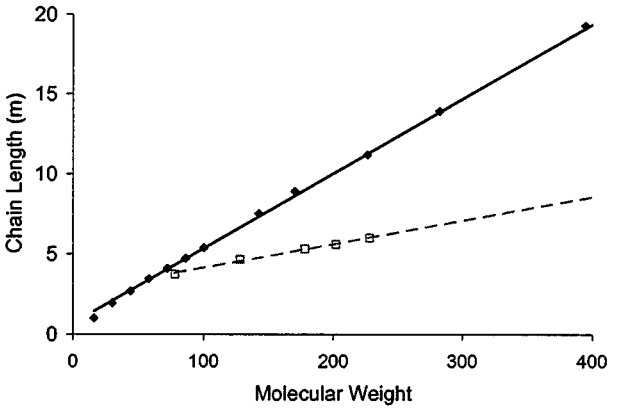

(a)

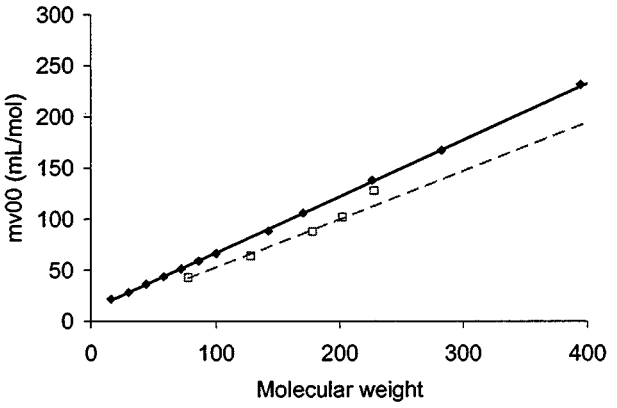

(b)

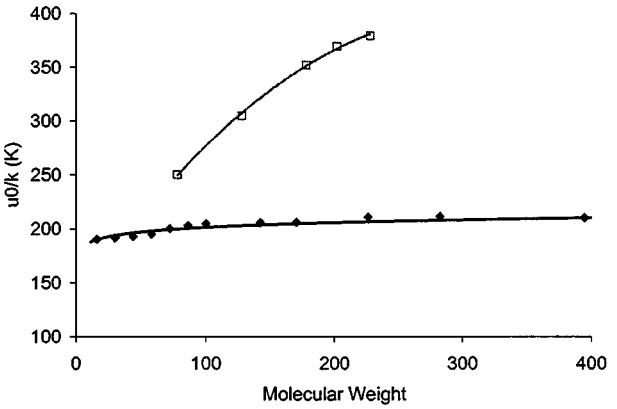

(c)

Figure 3.2. Well defined correlations exist for HRSAFT (shown here) as well as PCSAFT pure component parameters. (a) is a plot of molecular chain length (m) vs. molecular weight (MW), (b) a plot of molecular volume (mv^{00}) vs. MW, and (c) a plot of segment dispersion energy (u^0/k) vs. MW. The solid lines (solid diamonds) denote n-alkane parameters and the dashed lines (open boxes) denote polynuclear aromatics parameters. (Huang and Radosz, 1990) The parameters are fitted to a pure component's vapor pressures and liquid densities.

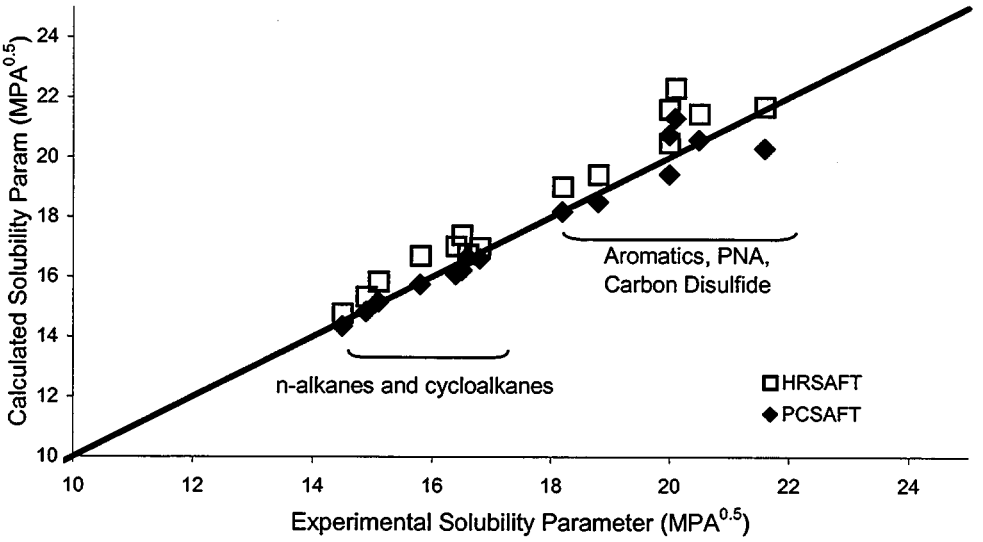

Figure 3.3. SAFT predicted (both PCSAFT and HRSAFT) vs. experimental solubility parameters for various classes of compounds at 298K and 1 bar. Experimental solubility parameters were obtained from Barton (1991).

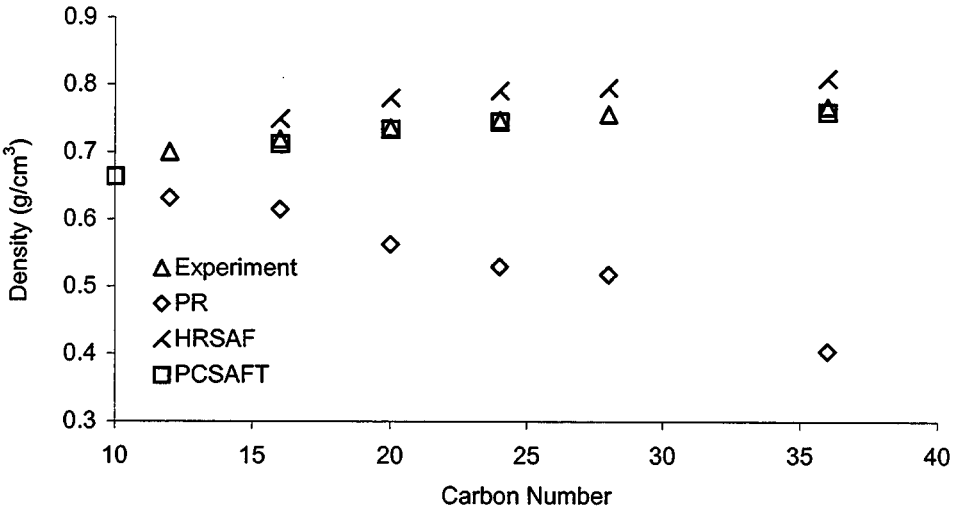

Figure 3.4. SAFT (PCSAFT and HRSAFT) and Peng-Robinson EOS calculated liquid densities for n-alkanes from dodecane to hexatriacontane at 372K and 1 bar.

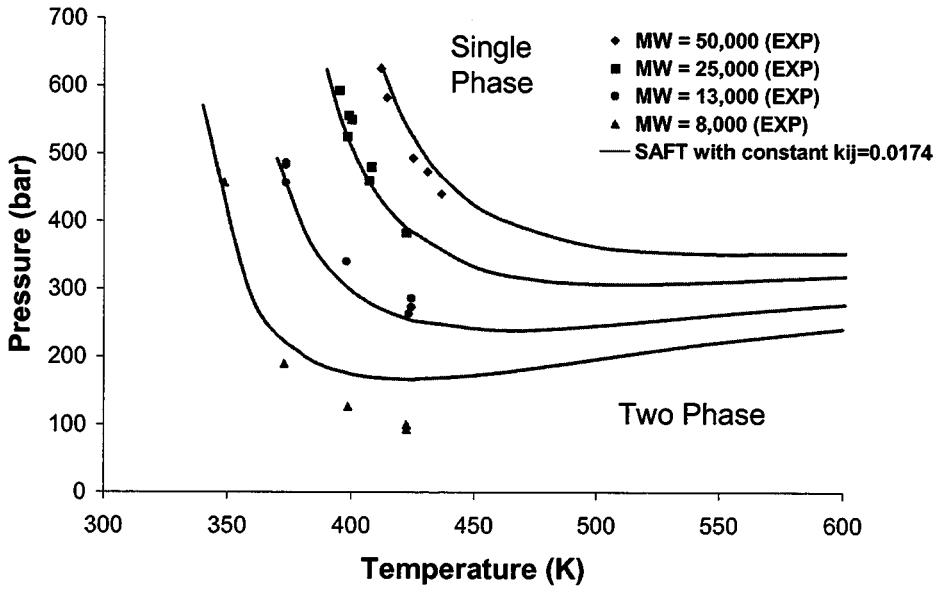

Figure 3.5. Cloud point pressures for 4% polystyrene solutions in n-hexane for various MW polystyrenes. The binary interaction parameter (k_{ij}) is kept constant in all HRSAFT calculations. Experimental data obtained from Xiong and Kiran (1997).

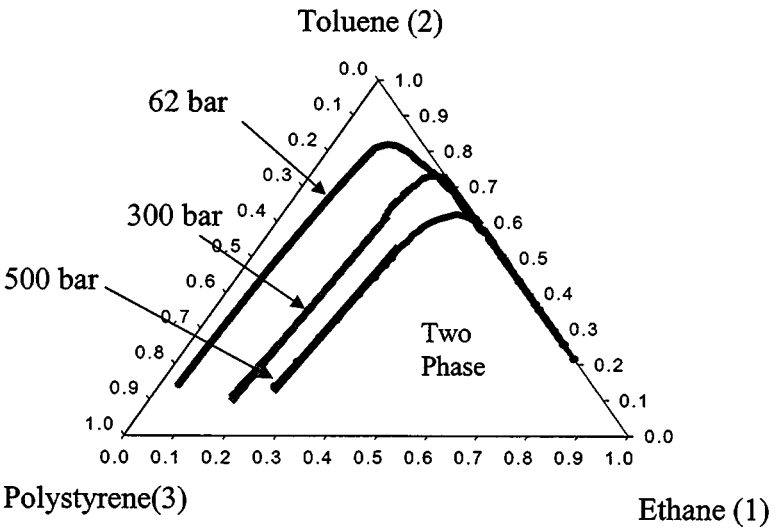

Figure 3.6. Pressure effects on a ternary system of polystyrene (MW=68,000), toluene, and ethane at 500K.

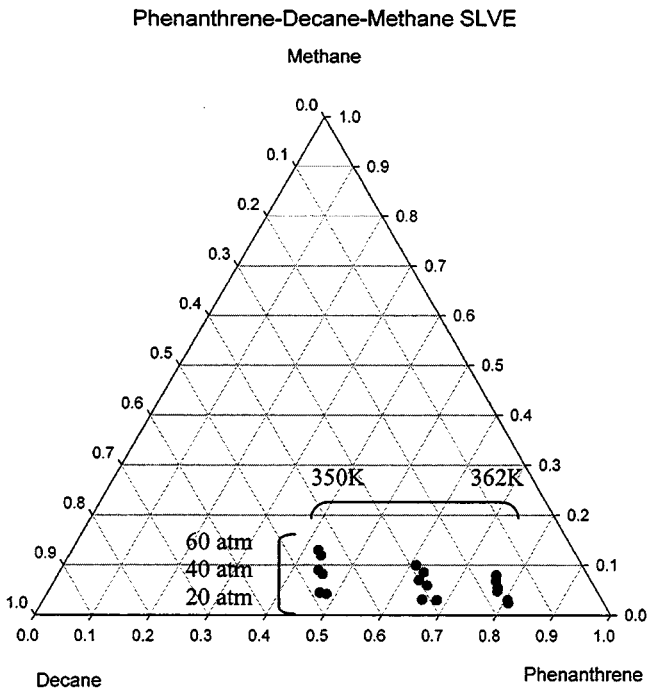

Figure 3.7. Experimental (solid circle) and PCSAFT (red circle) calculated solid-liquid-vapor equilibria points for a ternary system of phenanthrene, decane and methane for three isobars (20, 40, and 60 atms.) and temperatures between 350K and 362K. Experimental data obtained from Jacoby (1984).

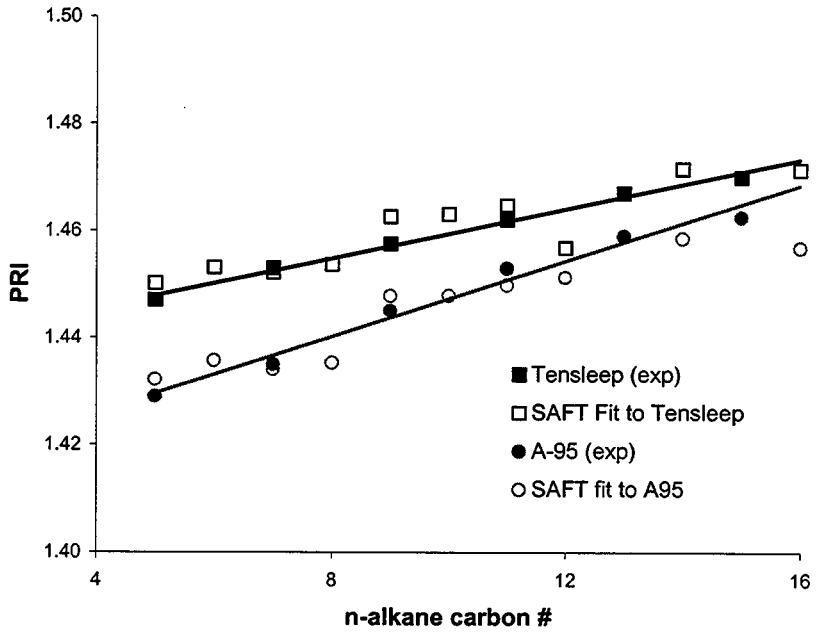

Figure 3.8. Experimental and fitted PRI for 1% (mass) Tensleep and A-95 n-C_7 asphaltenes in toluene and various n-alkane precipitants. Experimental PRI data were obtained from Wang (2000).

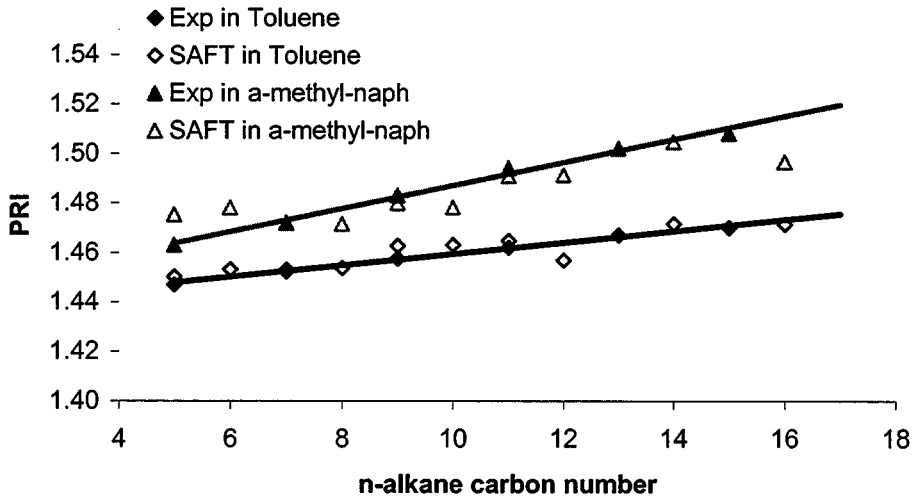

Figure 3.9. Plot of experimental and SAFT fitted PRI for asphaltene-toluene-precipitant systems and experimental and SAFT predicted PRI for asphaltene-toluene-alpha methyl naphthalene systems. Experimental PRI data were obtained from Wang (2000).

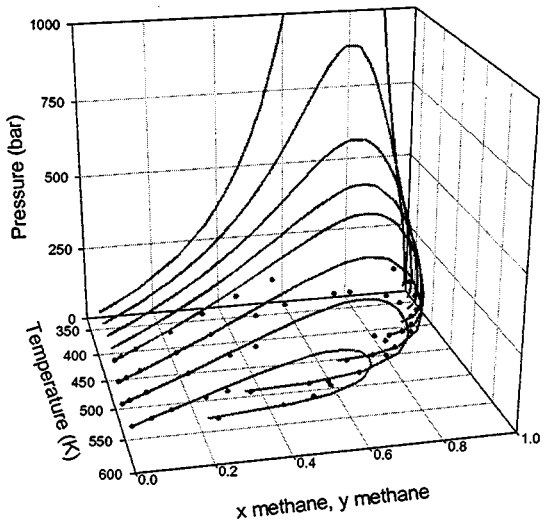

(a)

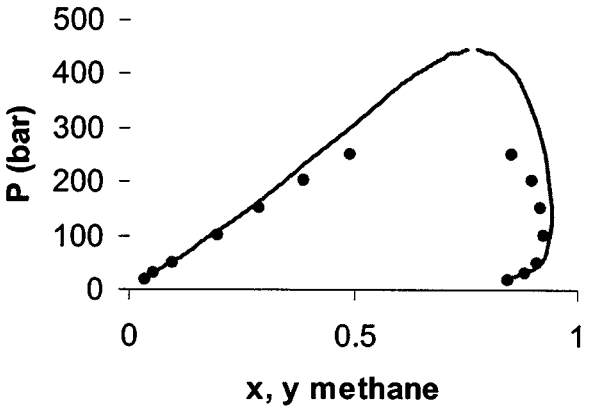

(b)

Figure 3.10. Experimental (dots) and HRSAFT calculated (lines) methane-toluene pressure-temperature-composition diagram (a). An isotherm on the global phase diagram is shown in (b) for T=422.5K. A constant temperature independent binary interaction parameter of 0.126 is used. Experimental data were obtained from Lin, *et. al.*, (1979).

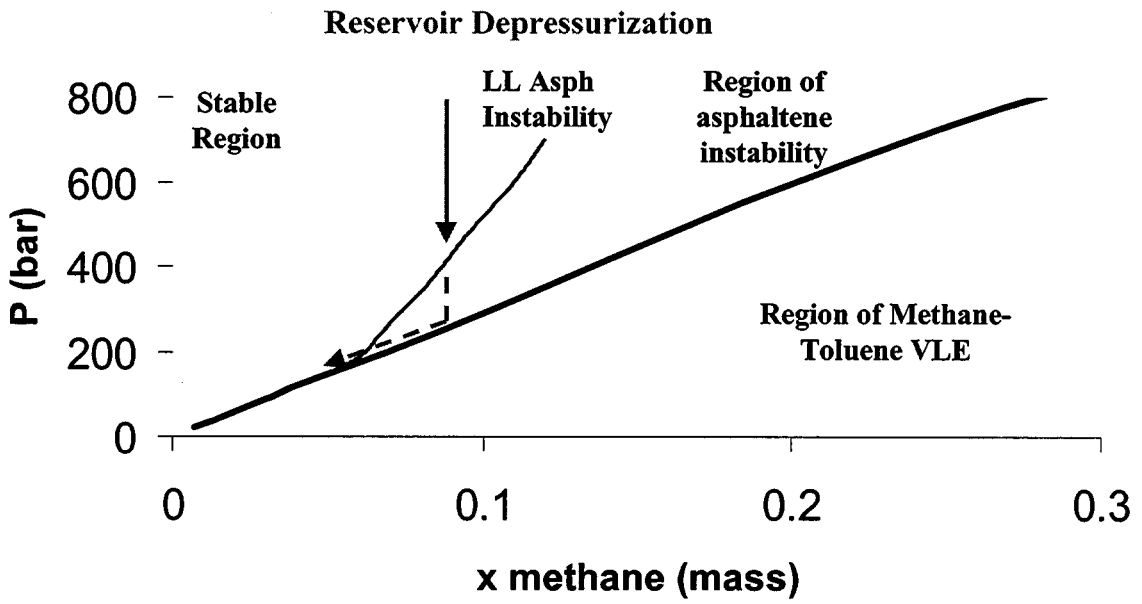

Figure 3.11. Methane-toluene-asphaltene isotherm at T=350°K for a 1% (mass in toluene) Tensleep asphaltene mixture.

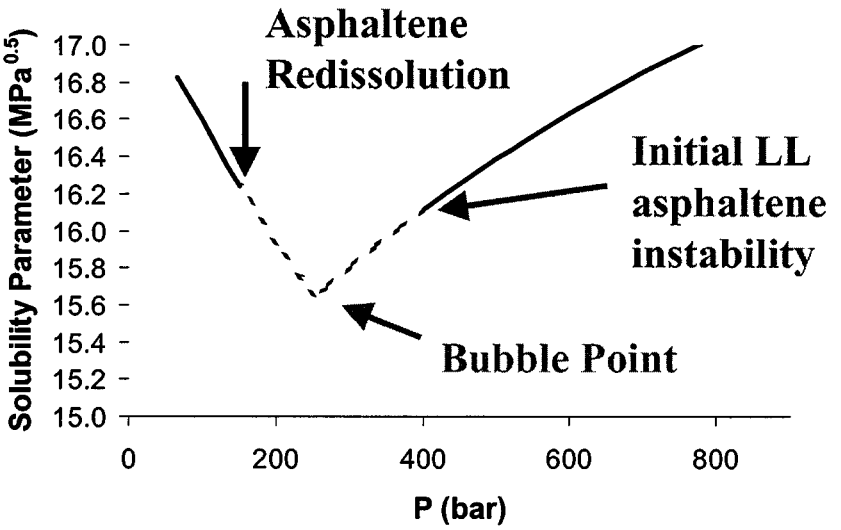

(a)

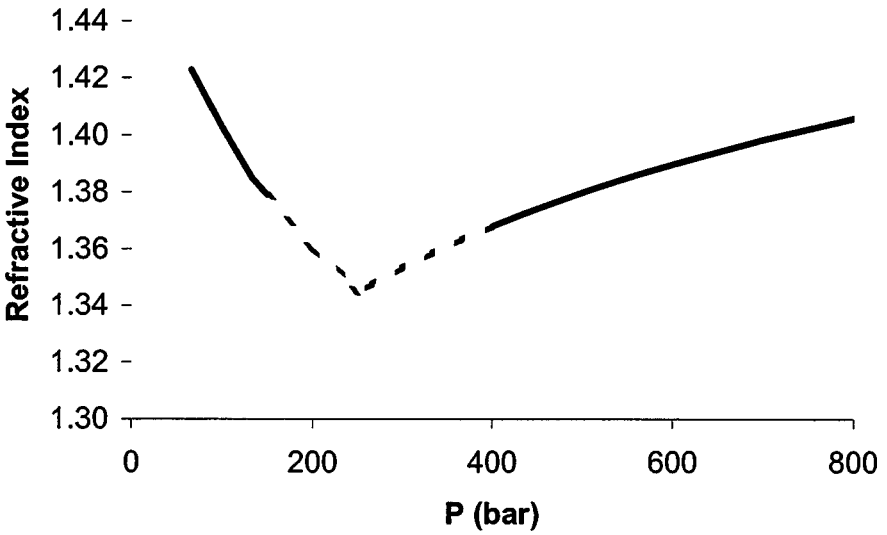

(b)

Figure 3.12. Changes in mixture solubility parameter (a) and refractive index (b) as a function of pressure during a typical reservoir depressurization experiment past its bubble point. The "live oil" used is a mixture of Tensleep asphaltenes (1% mass in toluene), toluene, and methane at T=350°K

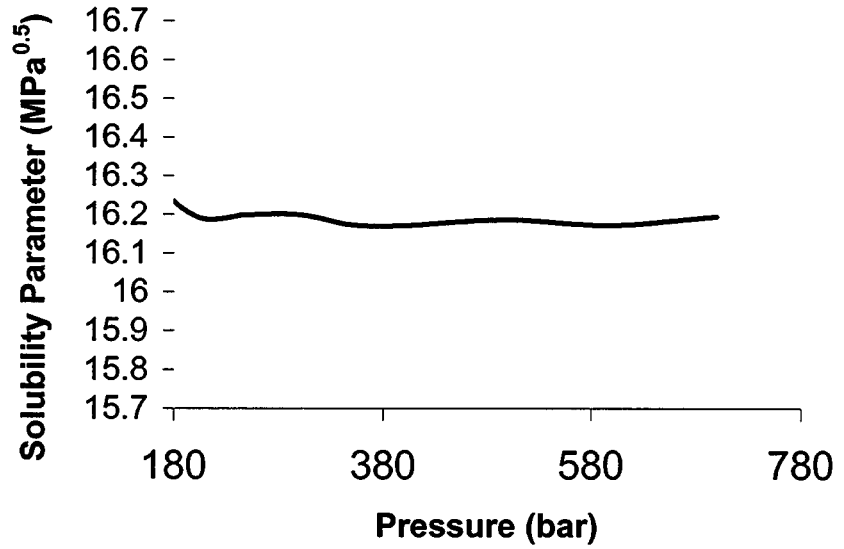

(a)

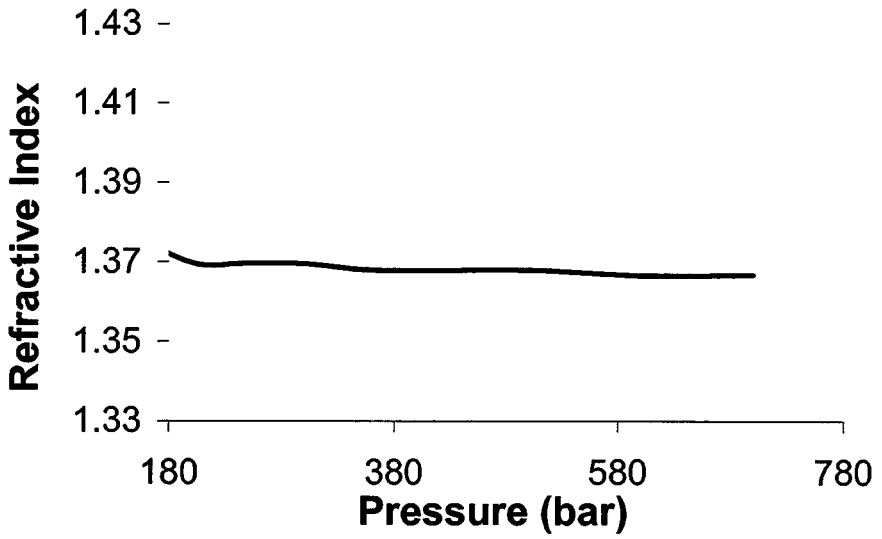

(b)

Figure 3.13. Changes in solubility parameter (a) and refractive index (b) as a function of pressure along the asphaltene liquid-liquid instability onset curve of a Tensleep asphaltene (1% mass in toluene)-toluene-methane "live oil" mixture at 350°K.

4. Observation of Asphaltene Aggregate Size near Onset of Precipitation

Introduction

The problem of asphaltene aggregation is very important in oil production. It is necessary to predict and prevent the aggregation and deposition of asphaltene from crude oil. However, the mechanics of asphaltene aggregation still remain unclear because of the complexity of both the asphaltene and crude oil. In this study, investigation is focus on the asphaltene aggregation resulting from the addition of n-heptane near onset of precipitation.

In general, there are two main thermodynamics models based on Flory-Hoggins polymer theory, lyophilic and lyophobic[1]. The lyophilic model is more preferable since it is simpler and easier to handle. It assumes that asphaltene in oil is solvated (lyophilic) and phase separation occurs when the solubility is lower than asphaltene concentration. The solubility can be obtained by minimizing the Gibbs free energy change upon mixing. When aggregation occurs, the solution changes into an asphaltene-poor phase and an asphaltene-rich phase. The stable region, metastable region and unstable region under certain concentration of precipitant can be calculated according to the Flory-Hoggins polymer theory [1].

Experimental observation on the same asphaltene solution can show quite different results with different aging time. This is caused by the change of aggregate size that affects the chemical potential of the asphaltene-rich phase. The objective of this study is to observe the change of crude oil – heptane system with aging time and to find out the relationship between aggregate size, aging time and precipitant concentration.

Most thermodynamic models do not include aggregate size as a thermodynamic variable. However, asphaltenes are known to aggregate even in good solvents. The observed onset of asphaltene precipitation or flocculation may be the condition where the aggregate size becomes large enough for observation by the usual optical methods. Dynamic light scattering may quantify the size of the aggregates before the onset of precipitation.

Method I Microscopic Observation

Experimental Reagents:

Crude Oils: Terra Cotta and Mars Pink

Precipitant: n-Heptane

Experimental Method:

First, mixtures with oil fractions from 0.2 to 0.8 were examined in increments of 0.1. Then mixtures were examined in increments of 0.05 and 0.01.

Experimental Steps:

Each mixture of crude oil with n-heptane was prepared in a 4 ml vial.

1. A measured amount of crude oil was delivered into the vial with a 1 ml plastic, disposable syringe that was accurate to 0.01 ml.
2. A measured amount of n-heptane was added into the vial with a 1 ml glass syringe that was accurate to 0.01 ml.
3. The vial was sealed immediately and was well shaken.
4. After the vial remained still for 1, 2, 4, 8, 12, 24 hour, a sample of the liquid mixture was observed under a microscope (lens magnification: 12.5×).
5. Symbols were used to express the microscopic observation. The results are below:

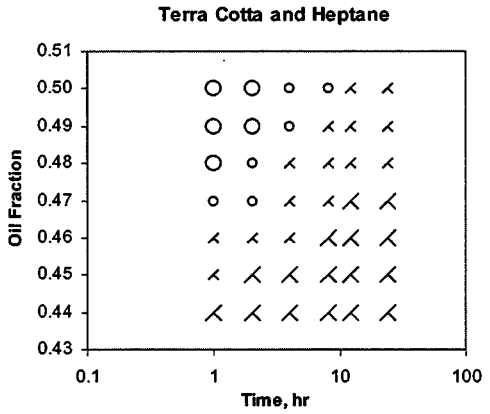

Fig. 4.1. (a)

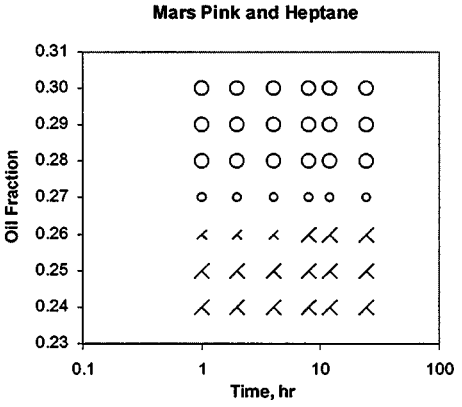

Fig. 4.1. (b)

Fig. 4.1. Microscopic observation of mixture of crude oil with n-heptane after aging time of 1, 2, 4, 8, 12, 24 hour. "Oil fraction" means the volume fraction of crude oil in the mixture.

O – Nothing could be seen; o – Fine particles; x – Tiny aggregation; X – Large aggregation.

Four photos (lens magnification: 12.5×) are showed below in order to illustrate the 4 symbols:

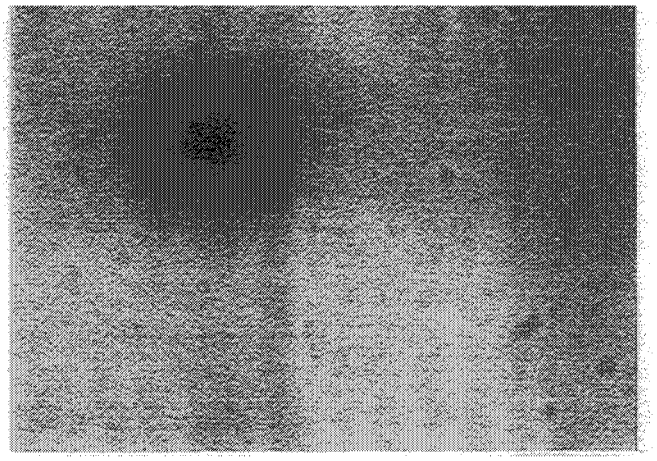

Fig. 4.2. (a) O – Nothing could be seen

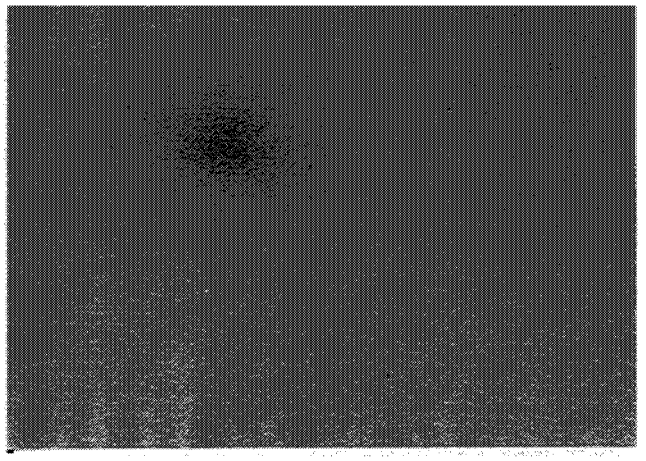

Fig. 4.2. (b) o – Fine particles

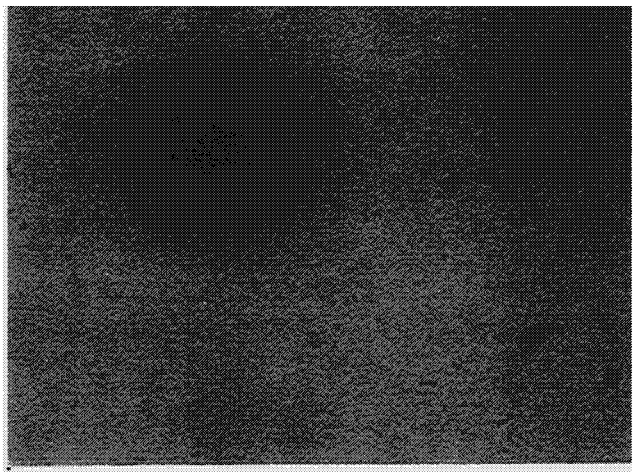

Fig. 4.2. (c) x – Tiny aggregation

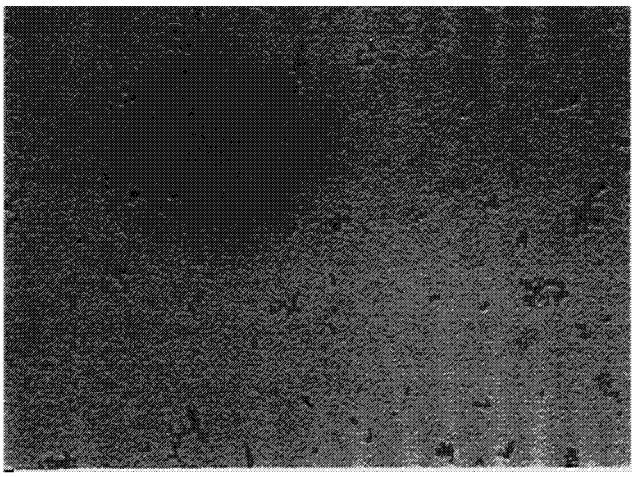

Fig. 4.2. (d) X – Large aggregation

Fig. 4.2. Microscopic photos of different states of asphaltene aggregation

Analysis and Conclusion

There was a clear onset in precipitation in mixtures of Mars Pink with n-heptane. With oil fraction that was above 0.27, no significant precipitation could be seen in 24 hrs. With oil fraction that was below 0.27, precipitation could be seen almost immediately. However, the precipitation processes of mixtures of Mars Terra Cotta with n-heptane were more gradual. At oil fraction of 0.47 to 0.50, no particles could be seen at the beginning but particles appeared after some time.

Method II Light Scattering

Principles:

Disperse particles in a suspension undergo Browian motion. This motion causes fluctuations of the local concentration of the particles and causes fluctuations of the intensity of scattered light. Such fluctuations can be determined and correlated to obtain the size distribution of the particles. The fluctuations of local concentration causes local inhomogeneities of the refractive index and lead to Rayleigh scattering spectrum with linewidth Γ [2], which is expressed as: $\Gamma = 2Dk^2$ (4.1)

where $k = (4\pi n/\lambda)\sin(\Theta/2)$, D is the diffusion coefficient, n is the refractive index, λ is the laser wavelength, and Θ is the scattering angle.

Assuming the particles to be spherical and non-interacting, one can obtain the mean radius r: $r = k_B T / 6\pi\eta D$ (4.2)

where k_B is Boltzmann's constant, T is the temperature, and η is the shear viscosity.

Particles smaller than 1 micron are difficult to be observed under a microscope. The range of light scattering measurement is about 0.01~1 micron. The crude oil-heptane system is opaque, that is to say, it is highly absorbent of light. Backscattering[3] geometry (see Fig. 3.) has been used to investigate the opaque system. The position of the scattering volume can be adjusted to measure light scattering near the wall (in this study, approximately 0.15 mm away from the wall). Y. G. Burya and etc.[3] have measured the mean radius of aggregates for some crude oils on adding n-heptane as a function of time.

Experiments

Experimental device: PhotoCor Complex spectrometer with PhotoCor-SP correlator;

square glass cells;glass capillary Cannon-Fenske routine viscometer

This PhotoCor Complex spectrometer was special because it had been scheduled to handle opaque systems. The length that the laser beam went through the suspension was only 0.15 mm. All the devices belong to M. A. Anisimov's lab, Univ. of Maryland.

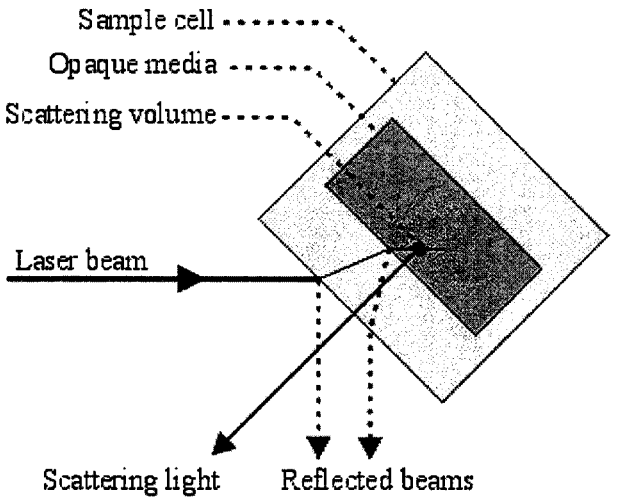

Fig. 4.3. Light-backscattering geometry

Experimental Steps:

1. A measured amount of crude oil was delivered into the cell with a 1 ml plastic, disposable syringe that was accurate to 0.01 ml.
2. A measured amount of n-heptane was added into the cell with a 1 ml glass syringe that was accurate to 0.01 ml.
3. The cell was sealed immediately, well shaken, and was put in the device.
4. The light in the room was switched off and the measurement was begun.
5. The viscosity of the sample was measured with a viscometer.
6. The density of each crude oil was measured with a balance that is accurate to 0.001g.

Results

Table 4.1 Viscosity of Samples

	Terra Cotta			Mars Pink	
Oil Fraction	0.45	0.47	0.50	0.25	0.27
Viscosity(cP)	2.11	2.31	2.59	1.08	1.14

Calculation of Refractive Index:

Denote the volume fraction of oil as ϕ_{oil} , the RI of mixture of oil with heptane can be expressed as: $RI_{mix} = \phi_{oil} \times RI_{oil} + (1-\phi_{oil}) \times RI_{hep}$

Table 4.2 Density and RI of Crude Oils and n-Heptane

	n-Heptane	Terra Cotta	Mars Pink
RI	1.388	1.51	1.538
Density(g/ml)	0.684	0.900	0.964

The results of light scattering are below:

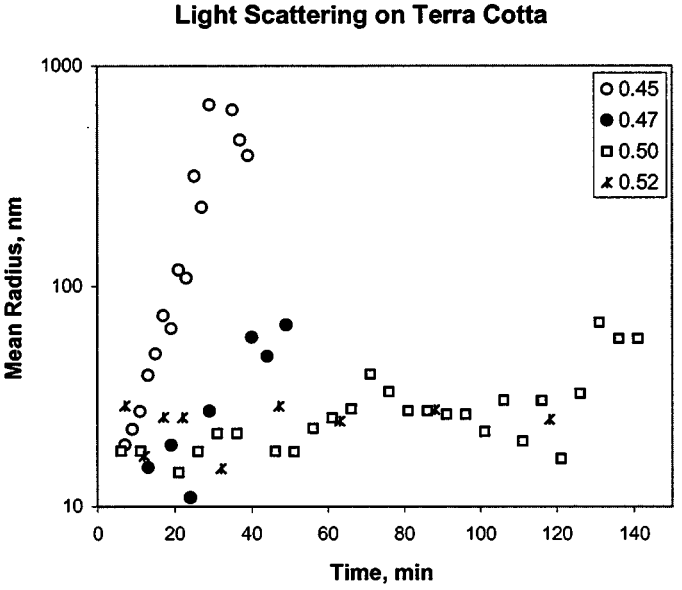

Fig. 4.4. (a) Mean radius of the aggregates plotted as a function of time for Mars Terra Cotta on adding heptane

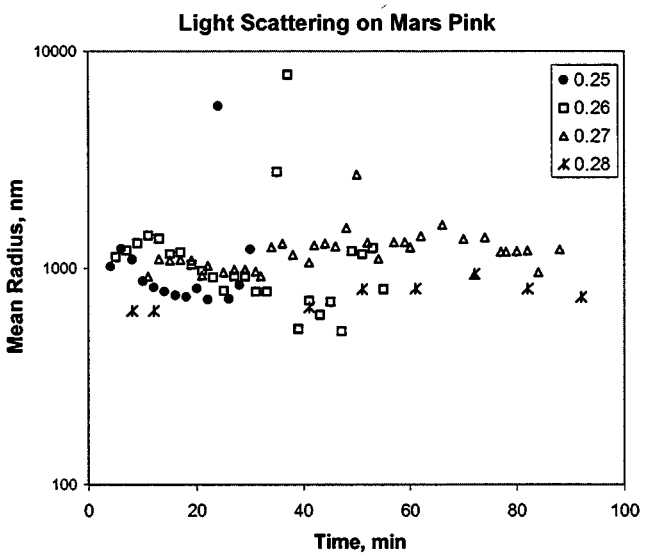

Fig. 4.4. (b) Mean radius of the aggregates plotted as a function of time for Mars Pink on adding heptane

Analysis

There were two parts of correlation function in the light scattering measurement. One could be refer to as "constant" part, while the other as "time-dependent" part. The latter correlated the oscillation of the transient intensity of light in a very short time period that was related to the Browian motion and local inhomogeneities in suspension. This part of correlation function was the basis of the calculation of the mean radius and was generally an exponential curve.

Both crude oils without n-heptane showed no correlation function at all, thus, there were no particles in both crude oils. The particles that suspended in the mixture of Terra Cotta with n-heptane grew up during the measurement at oil fractions of 0.45 and 0.47. However, there were no significant growing at oil fractions of 0.50 and 0.52. Maybe in such cases the concentration of precipitant was too low to keep the particles growing. Comparing the observation by light scattering with that by microscope, we can see that they accord with each other. With oil fraction of 0.45, the particle size went up to about 1 micron in 40 min, and small aggregate (about 1-3 micron) could be observed after 1 hr of aging. With oil fraction of 0.50 and 0.52, the sizes of particles were smaller that 0.1 micron after 2 hr, thus could not be observed under a microscope.

However, the particles that suspended in the mixture of Mars Pink with n-heptane did not show any growing in any of the four oil fractions. The sizes of particles were rather large (about 1 micron) almost immediately and stopped growing. Such results were some kind of strange. With oil fraction of 0.25, large aggregate was observed after 1 hr, while nothing could be seen with oil fraction of 0.28 after 1 hr. However, the observation by light scattering in these two concentrations gave almost the same results. With oil fraction of 0.30, no particles could be observed by either method.

For every sample, the "time-dependent" part of correlation function became rather weak and irregular (no longer exponential or similar) in 1 or 2 hrs. The mean radius that the calculation gave became quite unstable and the measurement had to be stopped. Such things did not occur in the measurement of latex in black ink. It might be caused by the sedimentation of the particles that were also observed in measurements with the microscope. During the measurement, the intensity of scattered light passed through maximum and then decreased. This suggests that sedimentation did occur. However,

mere sedimentation could not explain the strange correlation function in late period of measurements. Moreover, the suspensions of Terra Cotta and heptane with oil fraction of 0.50 and 0.52, had particles smaller than 50nm. Such small particles should not settle.

Another probable reason might be called "wall effect" since the length that incident light went through the liquid was only 0.15 mm. Some particles may stick to the wall of the cell and thus disturb the measurement. The "time-dependent" part of correlation function was no longer exponential in late period of measurements. Such cases may happen in gels. It was probable that gels were formed near the walls. However, these speculations have not been verified.

Conclusion

1. Both of microscopic observation and light scattering showed that the aggregation of mixture of Mars Terra Cotta and heptane was a gradual process. The precipitant concentration needed for aggregation was different with aging time. The aggregates were growing during aging.
2. Both of the two methods showed that the aggregation of mixture of Mars Pink and heptane was more or less an immediate process. The light scattering measurement showed no growing of aggregates.

Reference:

1. Jianxin Wang, "Predicting asphaltene flocculation in crude oils", New Mexico Institute of Mining & Technology, 2000.
2. I. K. Yudin, G. L. Nikolaenko, V. I. Kosov, V. A. Agayan, M. A. Anisimov, and J. V. Sengers, "A compact photon-correlation spectrometer for research and education," Int. J. Thermophys. **18**, 1237-1248(1997) .
3. Y. G. Burya, L.K. Yudin, V. A. Dechabo, V. I. Kosov, and M. A. Anisimov, "Light-scattering study of petroleum asphaltene aggregation," Applied Optics-LP, **40**, 4028-4035(2001).

5. Prediction of Bulk and Interfacial Thermodynamic Properties of Polar Mixtures by Statistical Associating Fluid Theory

ABSTRACT

A general purpose fortran code has been developed which implements a Statistical Associating Fluid Theory (SAFT) model in conjunction with a Rachford-Rice flash algorithm. The SAFT equation of state has been integrated into UTCOMP, a compositional reservoir simulator. The phase stability and the flash algorithms of UTCOMP are now available with SAFT equation of state. SAFT has been tested for several binary non-polar and polar mixtures and has been compared with Peng-Robinson equation of state. SAFT has been shown to do particularly well for polar mixtures.. We have tested SAFT for certain ternary mixtures and we are currently testing several other ternary three-phase systems. In this study we propose to extend some of these recent developments in the theory of hydrogen bonding into thermodynamic models, to predict the bulk and interfacial thermodynamic properties multicomponent mixtures of interest in oil field technology.

INTRODUCTION

Polar, associating molecules play a very important role in diverse physical systems such as molecular biology, polymer blends, oil recovery and microelectronics. Only recently has it been possible to include association effects in molecular models for predicting bulk thermodynamic properties. Chapman et al.,[32] have proposed a theoretically based equation of state, Statistical Associating Fluid Theory (SAFT) which accounts for associating molecules. Their approach is to use a reference fluid that incorporates, both the chain length (molecular size and shape) and molecular association, in place of the much simpler hard sphere reference fluid. The prediction of the interfacial behavior of these systems is also dependent on the understanding of the associating effect of these systems. There has been relatively little work done to develop models for

predicting the interfacial behavior of two-phase multicomponent systems containing associating molecules.

In this study we propose to extend some of these recent developments in the theory of hydrogen bonding into thermodynamic models, to predict the bulk and interfacial thermodynamic properties multicomponent mixtures of interest in oil field technology. As part of this work, so far, we have successfully implemented a Statistical Associating Fluid theory (SAFT) model for multicomponent mixtures. The model in conjunction with a phase-stability and flash algorithm has been used to study the phase behavior and bulk thermodynamic properties of mixtures of associating molecules commonly encountered in petroleum reservoir fluids. We have done extensive testing of the phase behavior of non-associating and associating binary mixtures using the SAFT model and compared its predictions with a popular engineering equation of state. We also propose to extend this model to predict interfacial properties, such as surface tension, interfacial tension and interfacial compositions of pure and multicomponent mixtures of alcohols, ketones and other polar compounds which is a very important challenge in understanding the wettability characteristics of crude oil-water-mineral systems.

BACKGROUND

Classical Equations of State

Equations of state that have been proposed in the literature generally have limitations with regard to the range of temperatures and pressures in which they are applicable and the substances that they can represent. Some equations are better for PVT, others for phase equilibria, and still others for enthalpy or entropy deviations. Cubic equations of state that are explicit in pressure and third degree in volume are among the most successful of the simpler forms. van der Waals [1], Redlich-Kwong [2] and Peng-Robinson equations of state [3] are some of the successful equations in this class. The advantages of these equations are that they are easy to implement in computer programs for repeated evaluations of properties. The van der Waals and Redlich-Kwong equations are not applicable to liquid phases and the Peng-Robinson equation does not do well for

low temperatures and for polar compounds. The Benedict-Webb-Rubin [4,5] EOS is one of the equations that successfully predicts behavior under cryogenic conditions. The Lee-Kesler [6] equation has been shown to predict enthalpy deviations very well.

For liquids, activity coefficient models have been shown to be quite successful. The group contribution method has been developed for calculation of activity coefficients. In this method the activity coefficient is considered to be the sum of the contributions of each individual group and the interaction between two groups as determined by matching the experimental phase equilibrium data. These methods have been shown to do well for polar compounds as well, but only for low pressure systems [7]. The UNIFAC model is the most popular group contribution method [8].

SAFT Equation of State

The other main class of equations is those based on intermolecular potentials. These are based on the viewpoint that the bulk properties of substances are a result of properties of individual molecules and interactions between them. Molecularly based equations allow for separating and quantifying the effects of molecular structure and interactions on bulk properties and phase behavior. Examples of such effects are the molecular size and shape(e.g., chain length), association(e.g., hydrogen bonding) energy, and mean field (e.g., dispersion and induction) energy.

Liquid Theories Based on Hard Sphere Model The relation between inter-molecular interactions and bulk properties of the system is provided by statistical mechanics. In statistical mechanics the structure of a liquid is expressed in terms of a molecular radial distribution function. These distribution functions give the time averaged spatial configuration of the molecules in the liquid. The radial distribution function is obtained from the knowledge of the intermolecular pair potential using, for example, the integral equation theories. The simplest pair potential model is to assume that the fluid is made up of hard spheres. By studying the exact molecular dynamics results for hard-sphere fluids Carnahan and Starling [9] were able to propose an accurate equation for the radial distribution function. From the knowledge of the radial

distribution function other thermodynamic properties can be evaluated. The basic idea is that once the spatial distribution of molecules as well as the interaction energies among them is known, the total energy is obtained as the summation of the energies between the molecules.

Perturbation Theory for Dispersion Forces In the previous section a simple model of hard-spheres was mentioned. In reality the interaction potentials are more complicated. For example, most real gases are polar or multi-polar: carbon dioxide is quadrupolar, and hydrogen chloride is both dipolar and quadrupolar. In addition, polyatomic molecules are nonspherical: the breadth-to-length ratio of bromine is 0.547, and that of carbon disulfide is about 0.9. All these factors influence the physical properties of the substance. A simple spherically symmetric potential function cannot adequately describe these effects. However, simpler models could serve as reference potentials, and the additional effects, such as quadrupolar forces, could be treated as perturbations on the reference systems. In principle, when the reference system chosen is close to the final system, one would also expect the properties produced by adding the perturbations to be close to the final system. This is the basis of the perturbation approach. The general theory of perturbation methods was first clearly described by Zwanzig[10]. The dispersion term used in this study is a power series initially fitted by Alder et al. [11]. This equation also provided the basis for the Perturbed Hard Chain Theory of Beret and Prausnitz [12] and by Chen and Kreglewski [13] in their equation of state, and was extended to mixtures by Simnick et al. [14].

Models for Association Effects

Early Models As mentioned in the previous section, perturbation theories give accurate results when the reference system chosen is close to the real pair potential. In case of molecules with specific directional associating sites such as alkanols, water and acids the simple hard sphere reference fluid proposed earlier is inadequate. There have been many attempts in the past to model association effects in fluid phase equilibria. Perhaps the best known concept is the chemical theory of Dolezalek [15], which postulates the existence of distinct molecular species in solution, which are a result of

chemical reactions assumed to be in a state of chemical equilibrium. This concept has been adopted in many approaches that usually utilize the chemical equilibrium constants involving the chemical entropy and enthalpy terms (in effect binary parameters) to allow for temperature dependence. These concepts are reviewed in Prausnitz et al. [16].

An alternative approach is that of lattice theories based on modeling the fluid structure as having essentially a solid-like lattice structure. Guggenheim [17] used the quasichemical approximation to treat non-random mixtures. Barker and Fock [18] used this theory for model mixtures. Several lattice models have been proposed to determine the properties of mixtures of strongly interacting molecules. There are several equations of state based on lattice theories that are popular in chemical engineering. The activity coefficient models applicable to nonrandom associating solution, for example, the models of Wilson [19], Abrams and Prausnitz [20], and Renon and Prausnitz [21], are based on these ideas.

Statistical Mechanical Models A more promising route leading to an understanding of associating fluids involves theories based on statistical mechanics. One approach has been to introduce molecular association into commonly used integral equation theories. Cummins and Stell [22], solved the integral equation in the Percus-Yevick approximation for the chemical association A+B=AB by using a spherically symmetric bonding potential. The model can be solved analytically in the limit of an infinitesimally wide and infinitely deep potential well; no effect of bonding orientation is included in the theory. Later Cummins and Blum [23] examined the directional character of the interaction in a study of the model for water. The system was solved in the PY approximation for the limit of surface adhesion.

Wertheim's Association Model Andersen was one of the first to introduce the geometry of the interaction at an early stage of the theory [24, 25]. He proposed a cluster (virial) expansion in terms of the total singlet number density (ρ) similar to the conventional approaches in simple fluids for obtaining the grand canonical ensemble partition function. The virial coefficients in the density expansion are dependent on the

intermolecular forces. The virial coefficients in the expansion are also referred to as graphs in the literature because of the use of pictorial graphs to represent the complex integration over volumes involved in these coefficients. The key concept in Andersen's model is that since the interaction is short-ranged and highly directional, the repulsive cores will restrict the system to single bonds at each attractive site. As a result many of the graphs in the expansion will be negligible. Although the incorporation of graph cancellation is cumbersome, Andersen's ideas have influenced later theories on associating fluids. Hoye and Olaussen [26] extended Andersen's approach by using a cluster expansion in terms of the monomer density rather than in terms of the overall density. They find that such an approach leads to much faster convergence.

The next most important advancement in the modeling of associating fluids is by Wertheim [27-30]. Wertheim did the resummed cluster expansion in terms of two densities, the total number density and the monomer density. This results in the applicability of the theory over a wide range of densities. Similar to Andersen, Wertheim was also able to simplify the complex graphical expansions by assuming that the repulsive core of each molecule restricts the orientationaly-dependent attractive forces to only single bonds at each attractive site. Some of the steric incompatibilities that result in graph cancellations are shown schematically in Figure 1. The first type involves three molecules: when the sites A and B on molecules 1 and 2 respectively get sufficiently close to form a bond, then the repulsive cores of molecules 1, 2 and 3 prevent molecule 3 from coming close enough to bond to either site A or B (Figure 1a). Another type of steric incompatibility prevents a site A on molecule 1 from bonding to two or more sites on molecules 2 (Figure 1b). One can also restrict the bonding between molecules to single bonding (Figure 1c).

Based on the graph cancellations discussed above, Wertheim was able to develop a key relationship between the residual Helmholtz energy due to association and the monomer density. This monomer density is related to a function Δ characterizing the association strength. Initially Wertheim had developed this theory for systems with a

single attractive site but later extended it to systems with multiple bonding sites. Wertheim's theory has been extended to mixtures of spheres [31].

Chains of Hard Spheres In this section, the Helmholtz's free energy contribution due to formation of chains is presented. Each chain can be visualized as m hard spheres at contact formed by imposing strong, covalent-like bonds on the hard spheres. In contrast to Wertheim's model where each hard-sphere can have multiple associating sites, for chain-formation each hard sphere needs to have two covalent bond forming sites on each of the hard-spheres in the interior of the chain and one covalent-bonding site on the end segments of the chain. With this simplification Wertheim's theory can be applied to chain formation taking into account the strength of the covalent bond. Chapman et al., [32] have derived a simplified expression for chain formation on the basis of the above formalism.

SAFT EQUATION OF STATE FOR MULTI-COMPONENT MIXTURES

Ideally, a single equation of state should incorporate all the effects described above in the previous section. Chapman et al. [33,34] proposed such an equation of state. The essence of their approach, referred to as the Statistical Associating Fluid Theory (SAFT) is to use a reference fluid that incorporates both chain formation and association bonding, in place of the much simpler hard sphere reference fluid used in most existing engineering equations of state.

The theoretical results underlying the equation of state are given in this section in terms of the residual Helmholtz energy a^{res} per mole, defined as $a^{res}(T,V,N)=a^{total}(T,V,N) - a^{ideal}(T,V,N)$, at the same temperature and density. All other thermodynamic quantities can be derived following a standard procedure as described, for example, by Topliss [35].

The residual Helmholtz energy is a sum of reference and dispersion parts:

$$a^{res} = a^{ref} + a^{disp} \qquad (5.1.a)$$

$$a^{ref}(T,V,N)=a^{hs}(T,V,N)+a^{chain}(T,V,N)+a^{assoc}(T,V,N) \quad (5.1.b)$$

Mixtures of Hard Spheres

The hard sphere term used is based on a theoretical result obtained by Mansoori et al. [36]. The Helmholtz energy is given by,

$$\frac{a^{hs}}{RT}=\frac{6}{\pi\rho}\left[\frac{(\zeta_2)^3+3\zeta_1\zeta_2\zeta_3-3\zeta_1\zeta_2(\zeta_3)^2}{\zeta_3(1-\zeta_3)^2}-\left\{\zeta_0-\frac{(\zeta_2)^3}{(\zeta_3)^2}\right\}\ln(1-\zeta_3)\right] \quad (5.2)$$

ζ_κ (k = 0 to 3) are functions of the molar density ρ. Since the reference fluid considered here contains hard spheres, which can be bonded to form chains, we use the ζ functions proposed by Chapman et al. [34], which are applicable to bonded spheres:

$$\zeta_k=(\pi/6)\,\rho\sum x_i\,m_i\,(d_i)^k \quad (5.3)$$

where x is the mole fraction, m_i is the number of segments(hard-spheres) per molecule, and d_i is the effective, temperature-dependent segment diameter.

The temperature dependence of the segment diameter d_i in the above equation is given based on the Barker-Henderson approach [37]. The equation used for d_i is given below based on the work of Chen and Kreglewski [13], who obtained d_i by solving the Barker-Henderson integral equation

$$d_i=\int_\sigma^\infty[1-\exp(-u(r)/kT)]dr \quad (5.4)$$

using a square-well potential. The final expression for d is

$$d_i=\sigma\left[1-C\exp\left[\frac{-3u^\circ}{kT}\right]\right] \quad (5.5)$$

u° / k in the above equation is the well depth, a temperature-independent LJ energy parameter, characteristic of nonspecific segment-segment interactions which will be referred to as the segment energy, in kelvin . Following Chen and Kreglewski, [13], the integration constant C is set to 0.12 .

We note that for pure components, Eq (5.3) reduces to

$$\frac{a^{hs}}{RT} = m\frac{a_0^{hs}}{RT} \tag{5.6}$$

where the hard-sphere term for pure segments a_0, is that proposed by Carnahan and Starling [9]:

$$\frac{a_0^{hs}}{RT} = \frac{4\zeta_3 - 3\zeta_3^{\,2}}{(1-\zeta_3)^2} \tag{5.7}$$

where ζ_3 is a segment packing fraction (reduced density):

$$\zeta_k = (\pi / 6)\,\rho\, m\, d^3 \quad \text{(pure components)} \tag{5.8}$$

Another useful expression derived by Mansoori et al. [35], which shall be invoked later, is the pair correlation function for a mixture of hard spheres (which approximate hard segments):

$$g_{ij}(d_i,d_j)^{seg} = g_{ij}(d_i,d_j)^{hs} = \frac{1}{1-\zeta_3} + \frac{3d_i d_j}{d_i + d_j}\frac{\zeta_2}{(1-\zeta_3)^2} + 2\left[\frac{d_i d_j}{d_i + d_j}\right]^2 \frac{\zeta_2^{\,2}}{(1-\zeta_3)^3} \tag{5.9}$$

$$g_{ii}(d_i)^{seg} = g_{ii}(d_i)^{hs} = \frac{1}{1-\zeta_3} + \frac{3d_i}{2}\frac{\zeta_2}{(1-\zeta_3)^2} + 2\left[\frac{d_i}{2}\right]^2 \frac{\zeta_2^{\,2}}{(1-\zeta_3)^3} \tag{5.10}$$

The hard-segment distribution function in the above equations depends on the effective sphere diameter d_i and on ζ_k (Equation 5.3).

The corresponding expression for the chemical potential due to the hard–sphere term for mixtures is given by [38].

$$\frac{\mu_i^{hs}}{kT} = -\ln(1-\zeta_3) + \frac{\Pi P_{CS}^{hs} d_i^3}{6kT} + \frac{3\zeta_2 d_i}{1-\zeta_3} + \frac{3\zeta_1 d_i^2}{1-\zeta_3} + \frac{9\zeta_2^2 d_i^2}{2(1-\zeta_3)^2}$$
$$+ 3\left(\frac{\zeta_2 d_i}{\zeta_3}\right)^2\left[\ln(1-\zeta_3) + \frac{\zeta_3}{1-\zeta_3} + \frac{\zeta_3^2}{2(1-\zeta_3)^2}\right] - \left(\frac{\zeta_2 d_i}{\zeta_3}\right)^3\left[2\ln(1-\zeta_3) + \frac{\zeta_3(2-\zeta_3)}{1-\zeta_3}\right] \tag{5.11}$$

where P_{CS}^{hs} is the contribution to the pressure from the hard-sphere terms. For mixtures the Carnahan-Starling radial distribution function gives the hard-sphere contribution to pressure as [38],

$$P_{CS}^{hs} = \frac{6kT}{\Pi}\left[\frac{\zeta_0}{1-\zeta_3} + \frac{3\zeta_1\zeta_2}{(1-\zeta_3)^2} + \frac{3\zeta_2^3}{(1-\zeta_3)^3} - \frac{\zeta_3\zeta_2^3}{(1-\zeta_3)^3}\right] \tag{5.12}$$

Note that the above expression for pressure includes the ideal-gas part as well. Hence the compressibility contribution from only the hard-spheres (z^{hs}) is,

$$z^{hs} = m\,(z_0^{hs} - 1) \tag{5.13}$$

and z_0^{hs} is given as,

$$z_0^{hs} = \frac{P_{CS}^{hs}}{m\rho\,kT} \tag{5.14}$$

For pure components, the corresponding expressions for the hard sphere part are

$$\mu^{hs} = m(RT)\left[\frac{4\zeta_3 - 3\zeta_3^2}{(1-\zeta_3)^2} + \frac{4\zeta_3 - 2\zeta_3^2}{(1-\zeta_3)^3}\right] \tag{5.15}$$

and

$$z^{hs} = m\frac{4\zeta_3 - 2\zeta_3^2}{(1-\zeta_3)^3} \tag{5.16}$$

Mixture of Chains

The pair correlation function given by Equation 5.9 is used to determine the Helmholtz energy contribution due to chain formation:

$$\frac{a^{chain}}{RT} = \sum x_i(1-m_i)\ln(g_{ii}(d_i)^{hs}) \tag{5.17}$$

where g_{ii} is evaluated for the interaction of two spheres i in a mixture of spheres, evaluated at the hard-sphere contact. Equation 5.17 has been derived on the basis of the associating fluid theory, where the association bonds are replaced by covalent, chain-forming bonds, as given by Chapman et al. [32,33,34].

The corresponding expression for chemcial potential is given by,

$$\frac{\mu_i^{chain}}{RT} = (1-m_i)\ln(g_{ii}(d_i)^{hs}) + \sum_j x_j\rho(1-m_j)\left[\frac{\partial \ln g_{jj}(d_j)^{hs}}{\partial\rho_i}\right]_{T,\rho_{j\neq i}} \tag{5.18}$$

where the partial derivative of the pair correlation function is given by

$$\left[\frac{\partial \ln g_{jj}(d_j)^{hs}}{\partial \rho_i}\right]_{T,\rho_{j\neq i}} = \frac{\Pi}{6}\frac{m_i}{g_{jj}(d_j)^{hs}}\left[\frac{d_i^3}{(1-\zeta_3)^2}+\frac{3}{2}\frac{d_j d_i^2}{(1-\zeta_3)^2}+\frac{3d_j d_i^3\zeta_2}{(1-\zeta_3)^3}+\frac{d_j^2 d_i^2\zeta_2}{(1-\zeta_3)^3}+\frac{3}{2}\frac{d_j^2 d_i^3\zeta_2^2}{(1-\zeta_3)^4}\right] \tag{5.19}$$

Similarly the contribution to the compressibility factor is given as

$$Z^{chain} = \sum_i x_i(1-m_i)\rho\left[\frac{\partial \ln g_{ii}(d_i)^{hs}}{\partial \rho}\right]_{T,x_j} \tag{5.20}$$

where

$$\rho\left[\frac{\partial \ln g_{jj}(d_j)^{hs}}{\partial \rho}\right]_{T,x_j} = \frac{1}{g_{ii}(d_j)^{hs}}\left[\frac{\zeta_3}{(1-\zeta_3)^2}+\frac{3}{2}\frac{d_i\zeta_2}{(1-\zeta_3)^2}+\frac{3d_i\zeta_2\zeta_3}{(1-\zeta_3)^3}+\frac{d_i^2\zeta_2^2}{(1-\zeta_3)^3}+\frac{3}{2}\frac{d_i^2\zeta_2^2\zeta_3}{(1-\zeta_3)^4}\right] \tag{5.21}$$

Mixture of Associating Spheres

The Helmholtz energy due to association, for pure components is given by Huang and Radosz [39], and is given for mixtures by Chapman et al. [34] and Huang and Radosz [39].

$$\frac{a^{assoc}}{RT} = \sum_i x_i\left[\sum_{A_i}\left[\ln Y^{A_i} - \frac{Y^{A_i}}{2}\right]+\frac{1}{2}M_i\right] \tag{5.22}$$

where $Y^{A}{}_{i}$, the mole fraction of molecules i not bonded at site A, in mixture with other compononents, is given by,

$$Y^{A_i} = \left[1 + \sum_i \sum_{B_i} \rho_j Y^{B_j} \Delta^{A_i B_j} \right]^{-1} \tag{5.23}$$

where $\sum_{Bj}$ is the summation over all sites on molecule j: A_j, B_j, C_j etc., and $\sum_i$ means summation over all components.

It is seen that $Y^{A}{}_i$ depends on the molar density ρ_j:

$$\rho_j = x_j \rho_{mix} \tag{5.24}$$

and on the association strength $\Delta^{A}{}_i{}^{B}{}_j$:

$$\Delta^{A_i B_j} = g_{ij}(d_j, d_j)^{seg} \left[\exp(\varepsilon^{A_i B_j} / kT) - 1 \right] (\sigma_{ij})^3 \kappa^{A_i B_j} \tag{5.25}$$

where $\sigma_{ij} = (\sigma_{ii} + \sigma_{jj}) / 2$. The segment radial distribution function in the above equation is approximated from Equation. 5.9.

The association contribution to the chemical potential μ_i^{assoc}

$$\frac{\mu_i^{assoc}}{RT} = \sum_{A_i} \left[\ln Y^{A_i} - \frac{Y^{A_i}}{2} \right] + \frac{1}{2} M_i + \sum_j \rho_j \left[\sum_{A_j} \left(\frac{\partial Y^{A_j}}{\partial \rho_i} \right)_{T, \rho_{l \neq i}} \left[\frac{1}{Y^{A_j}} - \frac{1}{2} \right] \right] \tag{5.26}$$

$$\left[\frac{\partial Y^{A_j}}{\partial \rho_i} \right]_{T, \rho_{l \neq i}} = -(Y^{A_j})^2 \left[\sum_{B_i} Y^{B_i} \Delta^{A_j B_i} + \sum_k \sum_{B_k} \rho_k \left[\Delta^{A_j B_k} \left(\frac{\partial Y^{B_k}}{\partial \rho_i} \right)_{T, \rho_{l \neq i}} + Y^{B_k} \left(\frac{\partial \Delta^{A_j B_k}}{\partial \rho_i} \right)_{T, \rho_{l \neq i}} \right] \right] \tag{5.27}$$

and

$$\left[\frac{\partial \Delta^{A_j B_k}}{\partial \rho_i}\right]_{T,\rho_{1\neq i}} = \left(\frac{d_j + d_k}{2}\right)^3 \left[\frac{\partial g_{jk}(d_j, d_k)}{\partial \rho_i}\right]_{T,\rho_{1\neq i}} [\exp(\varepsilon^{A_j B_k} / kT) - 1]\kappa^{A_j B_k} \tag{5.28}$$

$$\left[\frac{\partial g_{jk}(d_j, d_k)^{hs}}{\partial \rho_i}\right]_{T,\rho_{1\neq i}} = \frac{\pi}{6} m_i \left[\frac{d_i^3}{(1-\zeta_3)^2} + 3\left(\frac{d_j d_k}{d_j + d_k}\right)\left[\frac{d_i^2}{(1-\zeta_3)^2} + \frac{2d_i^3\zeta_2}{(1-\zeta_3)^3}\right] + 2\left(\frac{d_j d_k}{d_j + d_k}\right)^2\left[\frac{2d_i^2\zeta_2}{(1-\zeta_3)^3} + \frac{3d_i^3\zeta_2^2}{(1-\zeta_3)^4}\right]\right] \tag{5.29}$$

The corresponding expression for the compressibility factor due to association is

$$Z^{assoc} = \sum_i x_i \frac{\mu_i^{assoc}}{RT} - \frac{a^{assoc}}{RT} \tag{5.30}$$

Dispersion Term:

A general expression for the dispersion term is

$$\frac{a^{disp}}{RT} = m\frac{a_0^{disp}}{RT} \tag{5.31}$$

where m is the segment number and a_0^{disp} is the dispersion Helmholtz energy, per mole of segments. The a_0^{disp} term is a function of the segment energy u / kT [39].

$$\frac{a_0^{disp}}{RT} = \sum_j \sum_k D_{jk}\left[\frac{u}{kT}\right]^j \left[\frac{\zeta_3}{\tau}\right]^k \tag{5.32}$$

where D_{jk} are universal constants. In this work D_{jk} that have been refitted to accurate PVT, internal energy and second virial coefficient data for argon, by Chen and

Kreglewski [13] have been used. τ=0.74048 is the segment volume fraction in a close-packed arrangement. Hence, there are two parameters in the dispersion term, u/kT and m that have to be generalized for mixtures.

The mixing rule of the conformal solution [40], van der Waals one-fluid theory (vdW1) is used. It defines the molecular energy and size (volume) of a hypothetical pure fluid having the same residual properties as the mixture of interest. The vdW1 averaging equations are:

$$\frac{u}{kT} = \frac{\sum_i \sum_j x_i x_j m_i m_j \left[\frac{u_{ij}}{kT}\right] (v^\circ)_{ij}}{\sum_i \sum_j x_i x_j m_i m_j (v^\circ)_{ij}} \tag{5.33}$$

$$(v^\circ)_{ij} = \left[\frac{1}{2}[(v^\circ)_i^{1/3} + (v^\circ)_j^{1/3}]\right]^3 \tag{5.34}$$

$$u_{ij} = (1-k_{ij})(u_{ii}\, u_{jj})^{1/2} \tag{5.35}$$

where k_{ij} is an empirical binary parameter, fitted to experimental data.

The temperature dependence of u as given by Chen and Kreglewski, [13] is used

$$u = u^\circ \left[1 + \frac{e}{kT}\right] \tag{5.36}$$

and

$$v_i^\circ = \frac{\Pi}{6\tau} d_i^3 \tag{5.37}$$

where e/k is a constant that was related to Pitzer's acentric factor and the critical temperature [13, 41] for various molecules. Since the energy parameter in this model is

for segments rather than for molecules, e/k is set equal to 10 for all molecules. The only exceptions are a few small molecules where the e/k values close to those derived by Kreglewski have been used(e/k =0 for argon; 1 for methane, ammonia, and water; 3 for nitrogen; 4.2 for CO; 18 for chlorine; 38 for CS_2; 40 for CO_2; and 88 for SO_2); larger values of e/k for some of the molecules treated here as non-associating may be caused by their weak self-association.

Since the segment volume parameters V^{oo} and v^{o} are defined on a per-segment basis and hence do not vary much from molecule to molecule, especially for large molecules, we will use the segment number m as a measure of the molecular size. Therfore, our mixing rule for m (the average segment number for mixtures) is,

$$m = \sum_i \sum_j x_i x_j m_{ij} \tag{5.38}$$

where

$$m_{ij} = \tfrac{1}{2} (m_i + m_j) \tag{5.39}$$

The corresponding equation for the chemical potential is

$$\begin{aligned} \mu_i^{disp} &= m_i \sum_j \sum_k D_{jk} \left[\frac{u}{kT}\right]^j \left[\frac{\zeta_3}{\tau}\right]^k + m \sum_j \sum_k jD_{jk} \left[\frac{u}{kT}\right]^{j-1} \frac{\partial}{\partial n_i}\left(\frac{u}{kT}\right)\left[\frac{\zeta_3}{\tau}\right]^k \\ &+ m \sum_j \sum_k kD_{jk} \left[\frac{u}{kT}\right]^j \left[\frac{\zeta_3}{\tau}\right]^{k-1} \frac{1}{\tau}\frac{\Pi}{6} m_i \rho d_i^3 \end{aligned} \tag{5.40}$$

The corresponding compressibility factor is

$$z^{disp} = m \sum_j \sum_k kD_{jk} \left[\frac{u}{kT}\right]^j \left[\frac{\zeta_3}{\tau}\right]^k \tag{5.41}$$

The equation of state can be presented as the compressibility factor terms Z.

$$Z=1+Z^{hs}+Z^{chain}+Z^{assoc}+Z^{disp} \tag{5.42}$$

and the pressure of the system is given as

$$P = Z\,\rho\,K\,T \tag{5.43}$$

The chemical potential of the system can be calculated as

$$\mu_i = \mu_i^{ideal} + \mu_i^{hs} + \mu_i^{chain} + \mu_i^{assoc} + \mu_i^{disp} \tag{5.44}$$

The chemical potential contribution due to the ideal part μ_i^{ideal} is given by Reed and Gubbins [38].

$$\mu_i^{ideal} = RT\ln(\rho x_i) \tag{5.45}$$

The above expressions have been used to correlate vapor-liquid equilibria for many real fluid mixtures.

MULTIPHASE EQUILIBRIUM ALGORITHM

Much of the difficulty in multiphase equilibrium calculations lies in determining how many equilibrium phases should be considered. The algorithm described here for the phase equilibrium calculation is a sequential process. Initially, the overall composition of the mixture is tested for stability. If the mixture is found unstable, a phase is added, now making a two-phase mixture, and a calculation is initiated to find the compositions of the two, assumed, equilibrium phases. Had the stability analysis indicated that the mixture of overall composition was stable, no further calculations would be done, i.e., we would conclude that a single-phase equilibrium mixture exists.

After the compositions of the two phases have been calculated, the stability of one of these phases is tested. If the stability analysis indicates that the phase is stable, it is concluded that the proper equilibrium state requires only two phases. If, however, the indication is that the phase is unstable, a third phase is added and a calculation is begun to find the equilibrium compositions of this, now, three-phase mixture. A phase is added one at a time and only as necessary.

In summary then, the algorithm implemented here uses a sequential procedure outlined by the following steps:

1) Test the overall composition, z, for phase stability.

2) If unstable, add a second phase and compute the compositions assuming two-phase equilibrium.

3) Test the stability of the composition of one of the phases calculated in step (2).

4) If the phase composition is unstable, add a third phase and compute phase compositions assuming three-phase equilibrium.

If phase stability calculations show a phase composition to be stable, either in step(1) or step(3) no further calculations are required. The following sections explain Step(1) (phase stability analysis) and the step(2) the (flash algorithm).

Phase Stability Analysis

A stability analysis calculation on a mixture of overall hydrocarbon composition z is a search for a trial phase, taken from the overall mixture that, when combined with the reminder of the mixture, gives a value of Gibbs free energy that is lower than a single phase mixture of overall hydrocarbon composition, z. Mathematically, this condition is written as

$$\Delta G = \sum_{i=1}^{n_c} n_i \left[\mu_i(\vec{y}) - \mu_i(\vec{z}) \right] \tag{5.46}$$

Where μ_i is the chemical potential of component i and $\vec{y}$ is the mole fraction corresponding to the mole numbers $\vec{n}$. Substituting fugacity coefficients in terms of μ_i results in a more usable expression of the change in free energy

$$\Delta G = \sum_{i=1}^{n_c} n_i \left[\ln y_i + \ln \phi_i(\vec{y}) - \ln z_i + \ln \phi_i(\vec{z}) \right] \tag{5.47}$$

where $\vec{y}$ and $\vec{z}$ are the mole fraction compositions corresponding to the mole numbers $\vec{n}$ and the test compositions.

If for any set of mole fractions the value of ΔG at constant temperature and pressure is greater than zero, then the phase will be stable. If a set of mole fractions can be found such that $\Delta G < 0$, the phase will be unstable. The following is an algorithm for minimization of the free energy.

Method of Stationary Point Locations

Michelsen [42] reasoned that not all values of the phase space are important. In particular, only those sets of $\vec{n}$ at the stationary points of ΔG needed to be examined for stability to be established.

The variables n_i in Equation (5.47) could be replaced by the product εy_i, where ε is the sum of all n_i. Making this substitution and dividing by ε, the function ΔG may be modified to

$$\Delta G = \sum_{i=1}^{n_c} y_i \left[\ln y_i + \ln \varphi_i(\vec{y}) - h_i \right] \tag{5.48}$$

where

$$h_i = \ln z_i + \ln \varphi_i (z) \text{ for } i = 1, \ldots, n_c \tag{5.49}$$

The stationary points of ΔG ($\bar{y}$) occur where the derivatives with respect to the $n_c - 1$ independent variables y_i are zero. Differentiating,

$$\left(\frac{\partial \Delta G}{\partial y_i}\right)_{y_s,(s\neq 1,\ldots,n_c)} = \ln y_i + \ln \varphi_i (\vec{y}) - h_i - k = 0 \quad \text{for } i = 1,2, \ldots, (n_c - 1) \tag{5.50}$$

where, taking y_{nc} as the dependent mole fraction

$$k = \ln y_{nc} + \ln \varphi_{nc} (z) - h_{nc} \quad \text{for } i = 1, \ldots, n_c \tag{5.51}$$

Note that k is a constant for all the derivative conditions. Substitution of k into Equation (5.48) illustrates that at a stationary point,

$$\Delta G = \sum_{i=1}^{n_c} y_i k = k \tag{5.52}$$

and for stability, $\Delta G > 0$ implies $k > 0$

Figure 5.2 shows a graphic interpretation of the theory using a Gibbs free energy of mixing curve. In this example, the stability of a mixture of 20 mole percent carbon dioxide and 80 mole percent ethane is examined. At the overall composition, a tangent to the Gibbs free energy of mixing curve can be drawn. A phase of this composition will be stable provided the tangent lies below the curve at all other points. Mathematically, the distance between the Gibbs free energy of mixing curve at a composition $\bar{y}$ and the tangent is given by the value of the function $\Delta G(\bar{y})$, Equation (5.48).

Also shown in Figure (5.2) is a stationary point. This is a point which is either a local maximum or minimum, or a saddle point, of the function $\Delta G(\bar{y})$. A tangent to the Gibbs free energy of mixing curve at the stationary point will be parallel to the tangent drawn at

the overall composition. The distance between the two tangents is given by Equation (5.52).

Hence, if this distance is greater than or equal to zero, the phase will be stable. In figure (5.2), the distance is negative for the mixture of 20-mole percent carbon dioxide, and therefore, the phase is unstable. The strategy of the method of Michelsen, then, is to locate the stationary points and infer phase stability at those points.

From the derivative conditions, there are n_c equations of the form

$$\ln y_i - k + \ln \varphi_i(\bar{y}) - h_i = 0 \quad \text{for } i = 1, 2, \ldots, n_c \tag{5.53}$$

A set of variables $\bar{Y}$ can be defined such that

$$\ln Y_i = \ln y_i - k \quad \text{for } i = 1,2, \ldots, n_c \tag{5.54}$$

Equation (5.54) becomes

$$\ln Y_i + \ln \varphi_i(\bar{y}) - h_i = 0 \quad \text{for } i = 1,2, \ldots, n_c \tag{5.55}$$

after substitution of $\ln Y_i$,

$$1 = \sum_{i=1}^{n_c} y_i = \sum_{i=1}^{n_c} Y_i e^k \tag{5.56}$$

Then with Equation (5.54)

$$y_i = \frac{y_i}{\sum_{r=1}^{n_c} y_r} = \frac{Y_i}{\sum_{r=1}^{n_c} Y_r} \tag{5.57}$$

which establishes the relationship between the mole fractions $\bar{y}$ and the variables $\bar{Y}$. Note from Equation (5.56) that for $K \geq 0$ which indicates a stable phase, the sum of the variables Y_i must be less than or equal to one. This then is the condition that indicates stability.

To locate the stationary points, a set of nonlinear equations is solved for the variables Y

$$\ln Y_I + \ln \varphi_i (\bar{y}) - h_i = 0 \text{ for } i = 1, \ldots, n_c \tag{5.58}$$

where the mole fraction $\bar{y}$ is related to these variables by

$$y_i = \frac{Y_i}{\sum_{s=1}^{n_c} Y_s} \quad \text{for } i = 1,\ldots, n_c \tag{5.59}$$

Once a solution to the above equation is found, stability of the phase is inferred by the sum of the variables $\bar{Y}$. If the sum is less than or equal to one, the phase is stable, otherwise it is unstable.

The numerical solution technique used to solve the above equation is of successive substitution iteration and a Newton-Raphson iteration. Initially a successive substitution technique is used and once the estimates reach sufficiently close to the true solution then we switch to a Newton-Raphson algorithm to achieve rapid convergence.

For the method of successive substitution, the updating equation is given by

$$Y_i^{K+1} = \exp [\, h_i - \ln \varphi_i(\bar{y}) \,] \text{ for } i = 1,\ldots,n_C \tag{5.60}$$

For the Newton-Raphson method the residual r_i can be defined as

$$r_i = \ln Y_i + \ln \varphi_i(\bar{y}) - h_i \quad \text{for } i = 1,\ldots, n_C \tag{5.61}$$

These nonlinear equations can be solved for the independent variables Y_i using the updating equation

$$Y_i^{K+1} = Y_i^K - (J)^{-1} r \tag{5.62}$$

Where J the Jacobian matrix is a n_C x n_C matrix whose elements are given by expressions of the form

$$j_{is} = \left(\frac{\partial r_i}{\partial Y_S} \right)_{Y_{m(m \neq s)}} = \frac{1}{\sum_{r=1}^{n_C} Y_r} + \frac{\partial}{\partial Y_S} [\ln (y_i \varphi_i (y))]_{Y_{m(m \neq s)}} \tag{5.63}$$

The calcualation steps can be summarized as follows

1. Compute variable h_i from equation 5.49.

2. Estimate values for variable Y_i.

3. Compute φ_i (y) where y_i is given by Equation 5.59.

4. Calculate the value of the variables r by Equation 5.61.

5. Check the convergence of the successive substitution iteration by satisfying the condition.

6. Max $| r_i | \leq \varepsilon_{con}$ for $i = 1,\ldots,n_C$.

7. If not converged, check for switching to Newton-Raphson iteration by satisfying the criterion.

8. Max $| r_i | \leq \varepsilon_{swi}$ for $i = 1,\ldots,n_C$.

9. If the switching criterion is not met, update variable Y_i using Equation (5.60) and goto step (3) to continue successive substitution iteration. If the switching condition is satisfied, go to step (8) to start Newton-Raphson iteration.

10. Calculate the partial derivatives required using Equation (5.63) to determine the elements of the Jacobian J.

11. Update variable Y_i using Equation (5.62).

12. Calculate the value of the residuals, Equation (5.61) and check for the convergence criterion.

13. If it is not converged, go to step (7).

After convergence is achieved, the solution needs to be checked for stability of the equilibrium phases. The non-triviality of the solution is checked by comparison with the feed composition. A phase composition is considered non-trivial if the following condition is satisfied

$$\left[\sum_{i=1}^{n_C}(y_i - z_i)^2\right]^{1/2} \geq \frac{\varepsilon_{triv}}{n_C} \tag{5.64}$$

If a solution does not satisfy this condition or if convergence is not achieved in a certain maximum number of iterations, the entire procedure is begun again with a new estimate for Y. A phase is assumed to be stable if all initial estimates lead to the trivial solution.

If Equation (5.64) above is satisfied by a converged composition y, a second condition is checked to determine stability. A phase is considered to be unstable if

$$\sum_{i=1}^{n_C} Y_i - 1 \geq \varepsilon_{stab} \tag{5.65}$$

otherwise it is assumed to be stable. If the non-triviality condition is met but the above stability condition is not met then the procedure is repeated with a different initial estimate of Y. In addition to checking for convergence to a nontrivial solution, Equation (5.65) is tested whenever a Y is found such that the condition $\Delta G < 0$ is satisfied. If Equation (5.65) is also satisfied then the phase is unstable.

For testing an overall composition for single-phase stability, two initial estimates may be used. The first estimate for Y is computed from

$$Y_i = z_i K_i \quad \text{for } i = 1,\ldots,n_c \tag{5.66}$$

and the second estimate is

$$Y_i = z_i / K_I \tag{5.67}$$

where K-values are computed using the correlation [43]

$$K_i = \frac{P_{Ci}}{P} \exp[\,5.37\,(1+\omega_i)\,(1-\frac{T_{Ci}}{T})] \qquad \text{for } i = 1,\ldots, n_C \tag{5.68}$$

When testing the stability of a two-phase mixture, the computational procedure is the same as that for a single-phase mixture except that now one of the two-phase composition is used in Equation (5.46) instead of the overall composition.

Four different sets of initial estimates are used

$$Y_i = (1/2)\,(x_{i2} + x_{i3}) \quad \text{for } i = 1,\ldots, n_C \tag{5.69}$$

$$Y_1 = 0.999 \text{ and } Y_i = 0.001/(n_C - 1) \quad \text{for } i = 2,\ldots,n_C \tag{5.70}$$

$$Y_{nC} = 0.999 \text{ and } Y_i = 0.001 / (n_C - 1) \text{ for } i = 1,\ldots,n_C - 1 \tag{5.71}$$

and

$$Y_i = \exp h_i \quad \text{for } I = 1,\ldots,n_C \tag{5.72}$$

Two trivial solutions, which are the composition of the two phases, may result. A test analogous to Equation (5.64) should be also done but this time for both phase compositions.

Flash Calculation

Once a mixure has been shown to split into more than one phase by the stbaility analysis calculation, the amounts and composition of each phase must be found. Two different algorithms are implemented in UTCOMP for flash calculation. One is a flash formulation using K-values with an accelerated successive substitution method (ACSS) [44]. The second method determines phase compositions by minimization of the Gibbs free energy using an implementation of the reduced gradient approach described by Trangenstein [45]. Perschke [46] presents details for both the methods.

Accelerated Successive Substitution Method

A flash calculation is made to find the composition and amounts of each phase of an n_p phase system. In terms of mole fractions, as is done in conventional vapor/liquid calculations, the unknowns are the phase mole frations, x_{ij} , and the amounts of each phase given as the ratio of moles in a phase to the total number of moles in the mixture. This ratio, for phase j, is donated L_j . Thus, there are $n_p + n_p\, n_c$ unknowns: L_i and x_{ij} .

Not all these variables, are independent. The mole fractions are constrained by

$$\sum_{i=1}^{n_C} x_{ij} = 1 \qquad \text{for } j = 1,2, \ldots n_P - 1 \tag{5.73}$$

and the phase distribution is constrained by

$$\sum_{j=1}^{n_P} L_j = 1 \tag{5.74}$$

The number of independent variables can be reduced even more by using the component molar balance constraints

$$z_i = \sum_{j=1}^{n} x_{ij} L_j \quad \text{for } i = 1,2, \ldots n_C \tag{5.75}$$

which reduces the number of independent variables by n_c .Note that there are only $n_P - 1$ independent expressions of the form of Equation (5.73) because given Equation (5.74) and Equation (5.75), the n_P th expression may be derived. With Equation (5.73), Equation 5.74 and Equation 5.75 the number of independent variables can be reduced to $n_c(n_p - 1)$.

As is done in vapor/liquid calcualations, K – values are defined as the ratio of the component mole fraction in a reference phase to that in another phase

$$K_{ij} = \frac{x_{i1}}{x_{ij}} \quad \text{for } i = 1,2, \ldots n_C, \text{ and } j = 2,3, \ldots, n_P \tag{5.76}$$

The choice of the reference phase 1 is entirely arbitrary. When the vapor phase is chosen as the reference the above equation reduced to the conventional vapor/liquid equilibrium constants.

By substituting for the fucacity in the thermodynamic conditions for equilibrium, the K-values can be related to the fugacity coefficients:

$$\ln K_{ij} = \ln \varphi_{ij} - \ln \varphi_{i1} \quad \text{for } i = 1, 2, \ldots, n_c \text{ and } j = 2, 3, \ldots, n_p \tag{5.77}$$

With expressions for the fugacity coefficients given by Equation (5.44), Equation (5.73) through Equation (5.77) form a set of $2\ n_p\ n_c + n_p - n_c$ equations in as many unknowns: K_{ij}, L_j and x_{ij}. In the formulation implemented here, the $n_c\ (n_p - 1)$ independent variables

are chosen to be K_{ij} for i = 1,2,..., n_c and j = 2,3,..., n_p, and the set of n_c (n_p – 1) equations given by Equation (5.77) are solved for these variables.

Since the phase distribution variables and phase mole fractions are now treated as dependent variables, Equation (5.73) through Equation (5.76) must be used in such a way that these dependent variables can be calculated from the K – values.

After solving Equation (5.74) for L_1 , for example, this expression can be substituted in Equation (5.75). With the K – value definitions of Equation (5.76) and the relations

$$\sum_{i=1}^{n_c} x_{ij} - \sum_{i=1}^{n_c} x_{i1} = 0 \qquad \text{for } j = 2,3, \ldots, n_p \tag{5.78}$$

expressions of the following form may be derived

$$g_j(L_2, L_3, \ldots, L_{n_p}) = \sum_{i=1}^{n_c} \frac{z_i \left(\frac{1}{K_{ij}} - 1\right)}{1 + \sum_{k=2}^{n_p} L_k \left(\frac{1}{K_{ij}} - 1\right)} = 0 \qquad \text{for } j = 2,3, \ldots, n_p \tag{5.79}$$

Equation (5.79) is also called the flash equation. For an n_p phase mixture, n_p – 1 equation of this form can be written. With a given set of K – values , these non-linear equations can be solved for the variables L_j, for j = 2,3,..., n_p. The remaining variable L_1 can be computed from Equation (5.74).

Phase mole fractions for the reference phase may be computed once the flash equation has been solved from

$$x_{i1} = \frac{z_i}{1 + \sum_{k=2}^{n_p} L_k \left(\frac{1}{K_{ik}} - 1\right)} \qquad \text{for } i = 1, 2, \ldots, n_c - 1 \tag{5.80}$$

The mole fractions for the remaining phases can be found from Equation (5.76) given K_{ij} and x_{i1}.

The numerical technique used for solution of Equation (5.77) is an acceleratted successive substitution algorithm. In this method, K-values are updated by

$$K_{ij}^{n+1} = K_{ij}^{n} \exp\left(-\lambda^{n+1} \frac{f_{il}}{f_{ij}}\right) \quad \text{for } i = 1, 2, \ldots, n_c \quad \text{and } j = 2, 3, \ldots, n_p \tag{5.81}$$

where λ^{n+1} is an acceleration factor computed by method three of Mehra, Hidemann, and Aziz .

The acceleration factor is computed in a recursive fashion. For $n = 0$, λ^1 is set to 1, which implies that a successive substitution step is taken. For $n > 1$, λ is found from

$$\lambda^{n+1} = \frac{\lambda^n \sum_{j=2}^{n_p} \sum_{i=1}^{n_c} [s_{ij}^n]^2}{\sum_{j=2}^{n_p} \sum_{i=1}^{n_c} [s_{ij}^n s_{ij}^{n+1}] - \sum_{j=2}^{n_p} \sum_{i=1}^{n_c} [s_{ij}^n]^2} \tag{5.82}$$

where

$$s_{ij} = \ln f_{ij} - \ln f_{il} \quad \text{for } i = 1,2,\ldots, n_c \quad \text{and } j = 2,3, .., n_p \tag{5.83}$$

The acceleration factor is kept within the range $1 \leq \lambda^{n+1} \leq 4$. If λ^{n+1} falls outside these limits then it is set to the limiting value.

It is essential that a solution of Equation (5.79) be found for each set of K – valued computed. In this algorithm, Newton's method is used. At each iteration L_j is updated by

$$L_j^{n+1} = L_j^n + \Delta L_j^n \quad \text{for } j = 2,3, \ldots, n_p \tag{5.84}$$

Where ΔL_j^n is calculated by the solution of

$$J^n \Delta L^n = - f^n \tag{5.85}$$

The elements of J, the Jacobian matrix, are given by

$$j_{jk} = - \sum_{i=1}^{n_c} \frac{z_i \left(\frac{1}{K_{ij}} - 1\right)\left(\frac{1}{K_{ik}} - 1\right)}{\left[1 + \sum_{h=2}^{n_p} L_h \left(\frac{1}{K_{ih}} - 1\right)\right]} \qquad \text{for } j,k = 2,3, \ldots, n_p \tag{5.86}$$

and f is a vector whose elements are the function values for g_j given in Equation (5.79). For a three-phase mixture, J is a symmetric 2 x 2 matrix

Iteration is assumed to have converged when either

$$\max | g_j (L_2 , L_3 , \ldots , L_{np}) | \leq \varepsilon_{tol} \quad \text{for } j = 2,3,\ldots , n_p \tag{5.87}$$

or

$$\max | \Delta L_j^n | \leq \varepsilon_{tol} \quad \text{for } j = 2,3,\ldots , n_p \tag{5.88}$$

where ε_{tol} has a small value of, for example, 1.0×10^{-10}

Because Newton's method is used, a good initial estimate must be available for convergence to be achieved. Special precautions are taken to locate, a small interval containing the solution for two-phase calculations. For a two-phase mixture, there is only one equation of the form of Equation (5.86) in one unknown, L_2. The derivative of this function with respect to L_2 is given by

$$\frac{d g_2}{d L_2} = - \sum_{i=1}^{n_c} \frac{z_i \left(\frac{1}{K_i} - 1\right)^2}{\left[1 + L_2 \left(\frac{1}{K_i} - 1\right)\right]^2} \tag{5.89}$$

hence the function g_2 (L_2) is monotonically decreasing. For a solution to exist in the physically meaningful interval of $0 \leq L_2 \leq 1$, then g_2 (0) > 0 and g_2 (1) < 0.

To locate an interval about the solution, a value for L_2 is chosen and g_2 (L_2) is computed. Depending on the sign of $g_2(L_2)$, L_2 is either increased, if g_2 (L_2) > 0, or decreased, if g_2 (L_2) < 0, until an interval has been located in which the value of g_2 (L_2) changes sign. The initial estimate of L_2 is taken as the halfway point between the interval boundaries.

In summary, one method implemented for calculation of phase amounts and ompositions is to solve the n_c (n_p – 1) equations given by Equation (5.77) for the n_c (n_p – 1) variables, K_{ij}. Equation (5.79), Equation (5.80), Equation (5.73) and Equation (5.74) are used to relate the phase distribution and phase mole fractions to the K-values. An accelerated substitiution algorithm is used to solve Equation (5.88). The procedure is given by the following steps:

1) Estimate K-values, either from phase stability analysis results or correlations.

2) Calculate the phase distribution, L_j, from Equation (5.79) using Newton's method

3) Calculate the reference phase composition from Equation (5.80) and the remaining phase mole fractions with Eauation (5.76) and the given Kvalues

4) Using the equation of state, compute fugacity coefficients for each phase

5) Calculate the acceleration factor Equation (5.82).

6) Update K-values from Equation (5.81)

7) Check for convergence

8) Go to step (2) with new K-values if not converged.

Convergence is assumed when

$$\max | s_{ij} | \leq \varepsilon_{con} \quad \text{for } i = 1,2, \ldots, n_c \quad \text{and } j = 2,3, \ldots, n_p \tag{5.90}$$

and

$$\max \left| \frac{K_{ij}^{n+1} - K_{ij}^{n}}{K_{ij}^{n}} \right| \leq \varepsilon_{con} \quad \text{for } i = 1,2, \ldots, n_c \quad \text{and} \quad j = 2,3, \ldots, n_p \tag{5.91}$$

where s_{ij} is given by Equation (5.79). The value of ε_{con} is, for example, 1.0×10^{-10} . Note that accelerated successive substitution steps are taken only if that step reduces the Gibbs free energy. Otherwise a successive substitution step is made.

Incorporation of SAFT in UTCOMP

UTCOMP is an isothermal, three-dimensional compositional reservoir simulator developed at the University of Texas at Austin, which implements the above described stability analysis and flash algorithms. The phase behavior aspect of the reservoir simulator is incorporated in the subroutine FLASH. The algorithm for the working of FLASH is given in Figure (2). UTCOMP has the Peng-Robinson equation of state and Redlich-Kwong equation of state incorporated in it. In this work I have incorporated SAFT equation of state into the existing formulation. The SAFT formulation as given in [40] computes the chemical potential of each of the components in each phase and also the compressibility factor. It is trivial to compute the fugacity coefficients from the chemical potential

$$\mu_i - \mu_i^{ideal} = - RT \ln \varphi_i \tag{5.92}$$

The subroutine PLFC computes the fugacity coefficients at each step of the phase equilibrium calculation. Due to incorporation of SAFT, now PLFC calls the appropriate subroutine SAFT_EOS to invoke the SAFT based fugacity coefficients. The input to SAFT is the pressure, P, temperature, T and the feed mole fractions, at each step of the algorithm. SAFT needs to compute the compressibility factor and the chemical potential and return these parameters to UTCOMP. The problem formulation for SAFT is

1) Solve $P = f(T, \rho, x_i \; i = 1,\ldots,n)$ for the phase density ρ, given the pressure P, temperature T and mole fractions x_i, $i = 1,\ldots,n$

2) Using the density computed in step 1 above calculate the compressibility factor, Z

from the equation

$$Z = P / (\rho RT) \tag{5.93}$$

and also the chemical potential from the equation

$$\mu = f(T, \rho, x_i \; i = 1,\ldots,n) \tag{5.94}$$

The solution to step (1) above usually has multiple roots for density. The problem is now to pick the correct root out of the different densities. Traditionally selecting the root that minimizes the overall free energy of the phase does this. So the local optimization problem within SAFT is

$$\text{minimize free energy } G = \Sigma \, x_i \, \mu_i \quad i = 1,\ldots,n$$

$$\text{w.r.t } \rho$$

$$\text{such that } P = f\,(T, \rho, x_{i,\, i=1,..,n})$$

The above optimization problem is solved by a sequential quadratic programming algorithm DNCONF from the IMSL standard Math library.

The input parameters needed by SAFT_EOS at each step to compute the fugacity coefficients are the temperature, pressure and the feed mole fractions. These are the input variables that UTCOMP needs to supply to SAFT. The subroutine SAFT_EOS gets access to the above mentioned input parameters from UTCOMP by the COMMON statement. These parameters are read into the corresponding SAFT parameters using the module 'declare.f90'. Similarly, the return parameters of the subroutine SAFT are the

compressibility factor and the fugacity coefficients and these are again exchanged by using the COMMON statement for UTCOMP and module 'declare.f90' for SAFT. So the subroutine SAFT_EOS is the bridge between the UTCOMP and SAFT.

SUMMARY

Results and Discussion

Figure 5.4 shows the vapor pressure curves for a few alkanes. Alkanes have been chosen initially to check the non-associating terms (hard-sphere, dispersion and chain terms) in SAFT. It is observed that the percentage average absolute deviation (% AAD) from experimental data, in the vapor pressure is 1.9 % for hexane. Similarly the % AAD for heptane and octane are 1.8 % and 1.6 % respectively which can be considered an excellent fit for engineering equations of state. In Figure 5.5 the liquid specific volume curves are presented for n-alkanes as calculated from the SAFT equation of state. The % AADs for liquid specific volumes are also very low: 3.5 % for hexane, 3.4 % for heptane and 3.4 % for octane. Table 5.1 lists the SAFT parameters used for non-polar compounds. Hence SAFT works well in both the liquid and the vapor regime.

Figure 5.6 shows vapor pressure curves for ammonia and ethanol each of which have association bonding sites on them. Ammonia has three proton donor sites and one proton acceptor site. It is assumed that all the different hydrogen bonds formed are equivalent in terms of the energy of interaction and the volume of the bond. This approximation is aimed at reducing the total number of fitting parameters in the equation of state. Only two additional parameters are introduced in the equation of state (the energy and entropy of bonding). The % AAD in the vapor pressure curve of ammonia is 1.6 %. Similarly ethanol has two proton donors and two electron donors and the interactions amongst them are all considered equivalent. The % AAD in the vapor pressure of ethanol is 0.86 % which is an excellent fit. Figure 5.7 shows the liquid saturated density curves for ammonia and ethanol and the respective % AADs are 3.2 % and 0.88 %. Table 5.2 lists the SAFT parameters used for the compounds mentioned

above. Thus SAFT works very well even for highly polar compounds. Figures 5.4 to 5.7 confirm the usefulness of SAFT for pure components.

We now test SAFT for binary mixtures. First, we test the system for small molecular weight hydrocarbon mixtures. For binary mixtures, we have also compared the SAFT results with phase equilibrium data obtained using a conventional three-parameter equation of state such as the Peng-Robinson equation of state. In Figure 5.8, the vapor-liquid equilibrium curve for butane-hexane at 293.15 K is presented. Both, SAFT and PR curves have been obtained without adjusting the binary interaction coefficient. We see that both SAFT and PR predict the liquid phase mole fractions fairly accurately. It should be noted that PR equation of state does remarkably well for hydrocarbon mixtures. This is because, PR equation of state parameters have been tuned particularly well for hydrocarbons. In Figure 5.9, the vapor-liquid equilibrium for a methane-hexadecane system is presented. This system has been selected to study the effect of the chain-term on the phase-behavior calculation. Hexadecane is a long chain molecule with the chain length as calculated from the pure component vapor pressure and liquid density fit to be 12.3. So the mixture is expected to show a significant effect of the chain term on the vapor-liquid equilibrium predictive capability of SAFT. Interestingly, we observe that although SAFT predicts the vapor phase mole fractions fairly accurately, the liquid phase methane mole fractions are over-predicted. On the other hand, PR equation of state predicts both the vapor-phase and the liquid phase mole fractions very accurately. It is seen in Figure 5.10 that when the binary interaction coefficient (k_{ij}) is adjusted to 0.882, then the SAFT predicts both the liquid and the vapor phase mole fractions accurately. Once k_{ij} has been established the same parameter can be used to predict the VLE curve for any other condition. This is shown by the second plot in Figure 5.10 which has been obtained at 623 K.

After this analysis of SAFT for non-associating binary mixtures, we test SAFT for associating binary mixture to evaluate the effect of the association term on the vapor-liquid phase equilibrium predictions. In Figure 5.11 the vapor-liquid equilibrium curve for a ethane-ethanol system at 313.4 K is presented. We have shown the PR equation of

state predictions as well to compare the effect of the association term. Both the curves have been obtained without adjusting the binary interaction coefficient. Clearly, it is seen that SAFT predict both the gas phase and the liquid phase mole fraction reasonably accurately. PR equation of state, on the other hand, does not do a very good job of predicting the liquid phase mole fractions. This is expected as PR equation of state has been designed for hydrocarbons and thus cannot handle polar components such as ethanol. Figure 5.12 shows the VLE curve for the same system at a higher temperature of 333.4 K. SAFT without any adjustment of the binary interaction parameter predicts the vapor-phase and the liquid-phase mole fractions fairly accurately. PR predicts the gas phase mole fraction, but over-predicts ethane liquid phase mole fractions. We tested another three-parameter equation of state: Redlich_Kwong equation of state, for this case. We observe that the predictions are even worse. We do not consider this equation of state in further comparisons. Figure 5.13 shows the VLE curve for methane-ethanol system at 313.4 K. In this case it is observed that although ethanol is an associating compound, the PR equation of state which does not explicitly account for association, does predict the liquid phase mole fractions very accurately. On the contrary, SAFT overpredicts the liquid-phase methane mole fractions. When the binary interaction coefficient is adjusted to 0.95, SAFT is able to predict the liquid-phase mole fractions. This could be because the methane pure component SAFT parameters reported in the literature are not the best parameter set when considering mixture behavior. This trend is again repeated at a different temperature of 333.4 K for the same system as shown in Figure 5.14.

Figure 5.15 shows the VLE curve for a CO_2-methanol system. Again we observe that for associating systems, SAFT has a better predictive capability than the PR equation of state. Figure 5.16 and Figure 5.17 show the VLE curve for a CO_2-ethanol system at two different temperatures. Although SAFT predictions are better than those of the PR equation of state are, the CO_2 liquid phase mole fractions are still over-predicted by SAFT. Figures 5.18 and 5.19 show the VLE curve for CO_2-propanol system. Here the improvement in liquid mole fraction prediction by SAFT is only marginal. This could be due to the poorer modeling of the non-associating part of the model, whose effects become significant for heavier molecules. When the binary interaction coefficient is

adjusted to 0.938 we get an excellent agreement of the vapor and the liquid phase mole fractions.

Figures 5.20 and 5.21 show the VLE curve for a ethane-propanol system. SAFT without any adjustment in the binary interaction coefficient predicts the liquid phase and the gas phase mole fractions accurately. The PR equation of state over-predicts the ethane liquid phase mole fractions.

Figure 5.22 shows SAFT predictions for an azeotrope forming mixture of methanol-hexane. A binary interaction coefficient of 0.956 captures the azeotrope and the liquid and the gas phase mole fractions very accurately. The PR equation of state is not able to capture the trend for azeotrope forming mixtures. Figure 5.23 shows the VLE curve for another azeotrope forming mixture of propanol and heptane where again SAFT with an adjustable binary interaction coefficient of 0.982 captures the azeotrope behavior. SAFT without any adjustment of the binary interaction coefficient does not do well around the azeotrope concentration, but predicts the phase behavior reasonably accurately at very low and very high concentrations of propanol.

We now proceed to test SAFT for the phase behavior of ternary mixtures. Figure 5.24 shows the VLE diagram of a ternary mixture of methane-ethane-propane system at –75 C and 100 psia. The SAFT predictions are not accurate in the liquid phase. PR equation of state, on the other hand, predicts the liquid and the gas phase mole fractions extremely accurately. Figure 5.25 shows the VLE curve of the same system at a higher pressure of 200 psia. The deviation in the SAFT predictions are even higher whereas the PR equation of state still accurately predicts the liquid and gas phase mole fractions. This suggests that the defects in the non-associating part of SAFT formulation become even more significant when handling ternary mixtures. The same trend is maintained at 400 psia, 600 psia and 800 psia as shown in Figures 5.26, 5.27 and 5.28. It is observed that the two-phase region shrinks as the pressure is increased. Figure 5.29 shows the liquid-liquid equilibrium curve for a mixture of methanol-cyclopentane-cyclohexane containing a polar compund. The system conditions facilitate formation of two liquid phases. It is seen that the methanol rich phase is very poorly predicted by PR with a range of adjustment

parameters and also by SAFT without any adjustment parameters. The hydrocarbon-rich phase is predicted reasonably well by PR equation of state with a binary interaction coefficient of 0.9. SAFT with a binary interaction coefficient of 0.95 has better predictions than PR equation of state in both the hydrocarbon-rich phase and the methanol-rich phase.

Conclusions and Proposed Future Work

We have developed a SAFT based model for phase behavior of multi-component mixtures of associating molecules. As shown in the previous section we have extensively tested the SAFT model for pure-components and binary mixtures. We have extensively studied binary mixtures of non-associating and associating mixtures. We conclude that SAFT clearly is more accurate when polar mixtures are modeled. We have also done some initial testing on ternary systems. We propose to do some extensive testing on liquid-liquid equilibrium and vapor-liquid equilibrium for various ternary systems. We have implemented the SAFT parameter evaluation for pseudo-components generally encountered in the modeling of reservoir fluids. We propose to test the pseudo-component phase behavior using SAFT rigorously for various petroleum reservoir fluids.

We have successfully merged SAFT into an existing compositional reservoir simulator (UTCOMP) which helps us in accurate predictions of thermodynamic properties in reservoir studies. Phase compositions are obtained by flash calculations. A rigorous Gibbs stability test is done before all flash calculations to determine the number of phases. UTCOMP has a three-phase calculation capability. The incorporation of an accurate thermodynamic model such as SAFT in a reservoir simulator such as UTCOMP as an alternative to the existing Peng-Robinson equation of state greatly enhances the prediction of thermodynamic properties of complicated hydrocarbon reservoir fluid mixtures.

REFERENCES

1. van der Waals, J.H., Physical society 1, **iii**, 333 (1890).
2. Redlich, O., and Kwong, J.N.S., *Chem. Review.*, **44**, 233 (1949).
3. Peng, D.Y., and Robinson, D.B., *Ind. Eng. Chem. Fundamen.*, **15**, 59 (19 76).
4. Benedict, M., Webb, G.B., and Rubin, L.C., *J. Chem. Physics.*, **8**, 334 (1940); **10**, 747 (1942).
5. Benedict, M., Webb, G.B., and Rubin, L.C., *Chem. Eng. Progress,* **47(8)**, 419 (1951); **47(9)**, 449 (1951).
6. Lee, B.I., and Kesler M.G., *AIChE Journal,* **21**, 510 (1975).
7. Chao, K.C., and Seader, J.D., *AIChE Journal,* **7**, 598 (1961).
8. Fredenslund, A.M ., Gmehling J., Michlsen, M.L., Ramussen P., and Prausnitz., *Ind. Eng. Chem. Process Des. Dev.*, **16**, 450 (1977).
9. Carnahan, N. F., and Starling, K. E., *J. Chem. Phys.*, **51**, 635 (1969).
10. Zwanzig R. W., *J. Chem. Phys.*, **22**, 1420 (1954).
11. Alder, B.J., Young, D.A., and Mark, M.A., *J. Chem. Phys.*, **56**,3013 (1972).
12. Beret, S., and Prausnitz, J.M., *AIChE J.* **21**,1123 (1975).
13. Chen, S.S., and Kreglewski, A., *Ber. Bunsen-Ges. Phys. Chem.*, **81**,1048 (1977).
14. Simnick, J.J., Lin, H.M., and Chao, K.C., *Adv. Chem. Ser.,* **182**, 209 (1979).
15. Dolezalek, F. Z., *Z. Phys. Chem.*, **64**, 727(1908).
16. Prausnitz, J.M., Lichtenthaler, R.N., De Azevedo, E.G., *Molecular Thermodynamics of Fluid Phase Equilibria*, Prentice-Hall:Englewood Cliffs, NJ,1986.
17. Guggenheim, E.A., *Applications of Statistical Mechanics*, Oxford University Press, Oxford, U.K., 1955.
18. Barker, J.A., and Fock, W., *Discuss. Faraday Soc.*, **15**, 188 (1953).
19. Wilson, G.M., *J. Am. Chem. Soc.*, **86**, 127 (1964).
20. Abrams, D., and Prausnitz, J.M., *AIChE J.*, **21**, 116 (1975).
21. Renon, H., and Prausnitz, J.M., *AIChE J.,* **14**, 135 (1968).
22. Cummins, P.T., and Stell, G. S., *Molec. Phys.*, **51**, 253 (1984).
23. Cummins, P.T., and Blum, L., *J. Chem. Phys.*, **84**, 1833 (1986).
24. Andersen, H.C., *J. Chem. Phys.*, **59**, 4714 (1973).
25. Andersen, H.C., *J. Chem. Phys.*, **61**, 4985 (1974).
26. Hoye, J.S., and Olaussen, K., *Physica A.*, **104**, 435 (1980).
27. Wertheim, M.S., *Journal of Statistical Physics*, **35,1**,19 (1984).
28. Wertheim, M.S., *Journal of Statistical Physics*, **35,1**,35 (1984).
29. Wertheim, M.S., *Journal of Statistical Physics*, **42, 3**, 459(1986).
30. Wertheim, M.S., *Journal of Statistical Physics*, **42,3**, 477(1986).
31. Jackson G., Chapman, W.G., and Gubbins K.E., *Molecular Physics*, **65, 1**,1 (1988).
32. Chapman, W.G., Jackson G., and Gubbins K.E., *Molecular Physics*, **65, 5**,1057 (1988).
33. Chapman, W.G., Gubbins, K.E., Jackson, G., and Radosz, M., *Fluid Phase Equilibrium.* **52**, 31(1989).
34. Chapman, W.G., Gubbins, K.E., Jackson, G., and Radosz, M., *Ind. Eng. Chem. Res.*, **29**, 1709 (1990).

35. Topliss, R. J., *Techniques to facilitate the use of equations of state for complex fluid-phase equilibria*. Ph.D. Dissertation, Univ. of California, Berkley, 1985.
36. Mansoori, G.A., Carnahan, N.F., Starling, K.E., and Leland,T.W., *J. Chem. Phys.* **54**,1523 (1971).
37. Barker, J.A., and Henderson, D., *J. Chem. Phys.*, **21**,1123 (1967).
38. Reed, T.J., and Gubbins, K.E., *Applied Statistical Thermodynamics*, Mc. Graw-Hill, 1973.
39. Huang, H.H., and Radosz, M., *Ind. Eng. Chem. Res.*, **29**, 2284 (1990).
40. Huang, H.H., and Radosz, M., *Ind. Eng. Chem. Res.*, **30**, 1994 (1991).
41. Kreglewski, A., *Equilibrium Properties of Fluids and Fluid Mixtures.*, The Texas Engineering Experiment Station (TEES) Monograph Series; Texas A&M University Press: College Station., 1984.
42. Michelsen,M.L., *Fluid Phase Equilibria*, **9**, 1,(1982).
43. Wilson, G.M., 65th National AIChE Meeting, Cleveland, OH, May 4-7, 1969.
44. Mehra, R.K., Heidemann, R.A., and Aziz, K., *Can. J. of Chem. Eng.*, **61**,590, (1983).
45. Trangenstein, J.A., *Chem. Eng. Sci.*, **42**, 2847, (1987).
46. Perschke, D.R., M.S. Thesis, University of Texas at Austin, 1984.
47. Chang, Y.B., Ph. D Dissertation, University of Texas at Austin, 1990.

	T range, K	v^{∞}, (mL/mol)	Chain length (m)	u^{o} / k (K)
Methane	92-180	21.576	1.000	190.29
n-Hexane	243-493	12.475	4.724	202.72
n-Heptane	273-523	12.282	5.391	204.61
n-Octane	303-543	12.234	6.045	206.03
n-Hexadecane	333-593	12.300	11.209	210.65
Benzene	300-540	11.421	3.749	250.19

Table 5.1: SAFT parameters for some non-polar compounds

	T range, K	v^{∞}, (mL/mol)	Chain length (m)	u^{o} / k (K)	ε / k (K)	$10^{2}\kappa$
Methanol	273-487	12.0	1.776	216.13	2714	4.856
Ethanol	302-483	12.0	2.457	213.48	2759	2.920
Ammonia	200-380	10.0	1.503	283.18	893.1	3.270

Table 5.2: SAFT parameters for some polar compounds

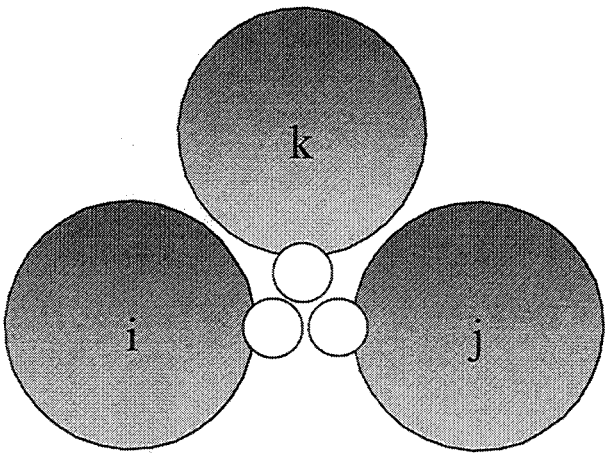

Figure 5.1 a : Only two molecules can form a bond at a single associating site

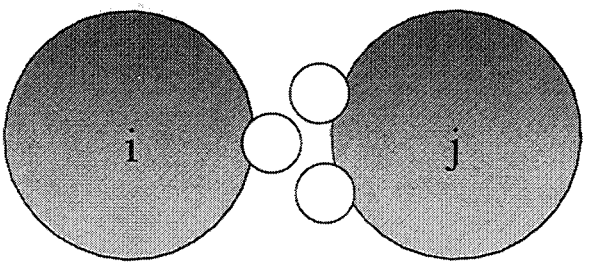

Figure 5.1 b : No site on one molecule can bond simultaneously to two sites on an another molecule

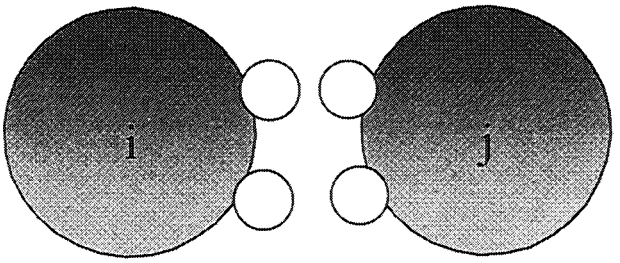

Figure 5.1 c Double bonding between molecules is not allowed

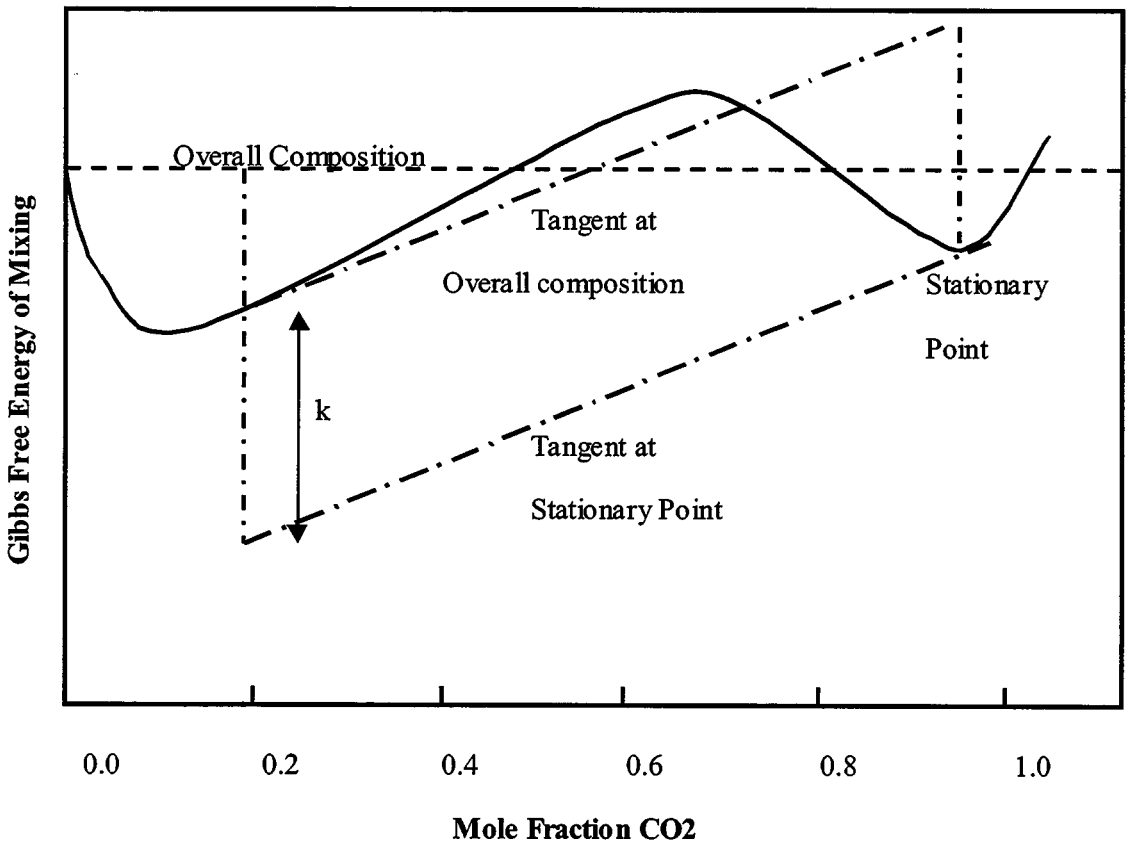

Figure 5.2 Graphical Interpretation of phase stability analysis and the method of Michelson

Figure 5.3: Algorithm for Phase Equilibrium Calculation

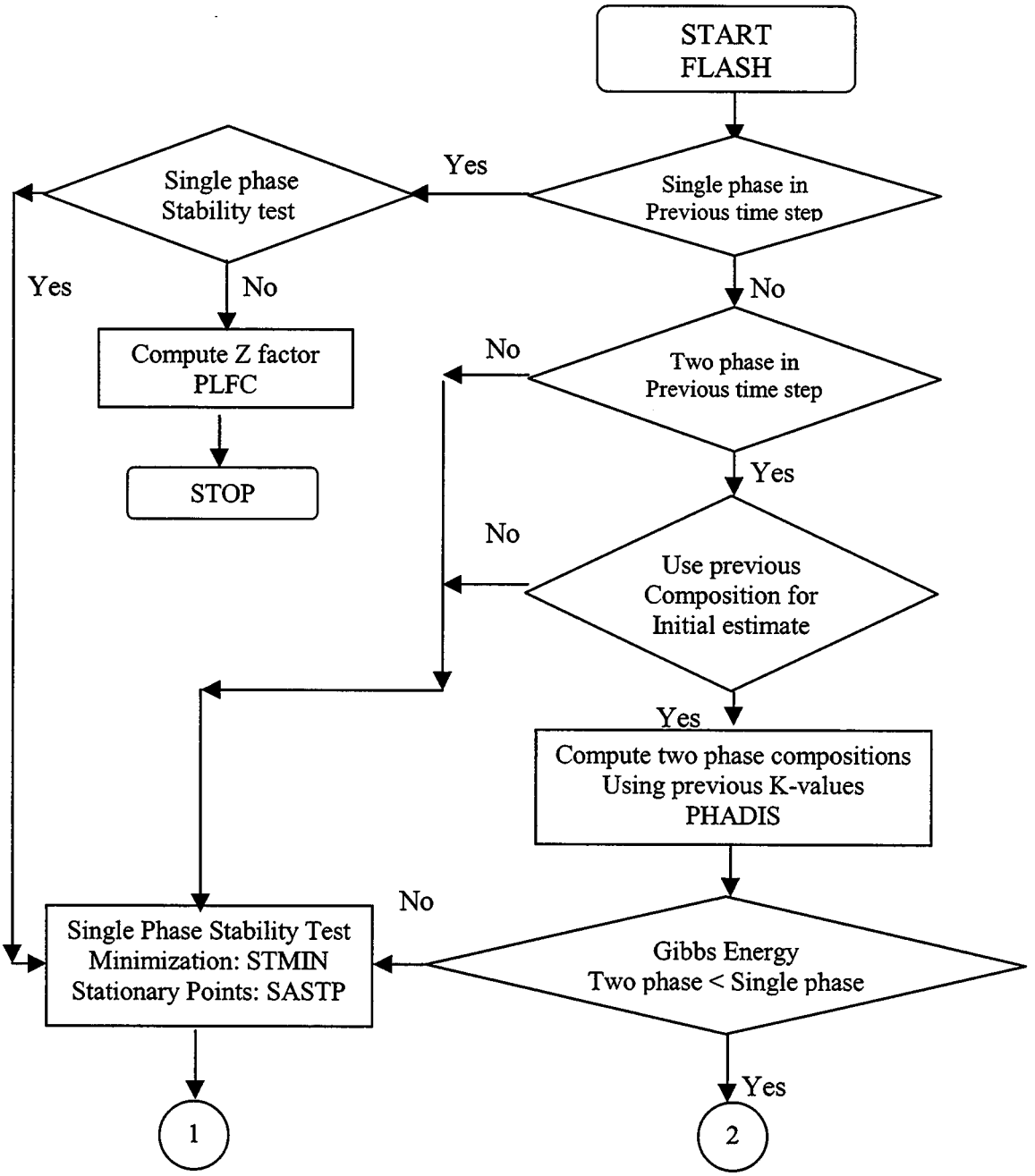

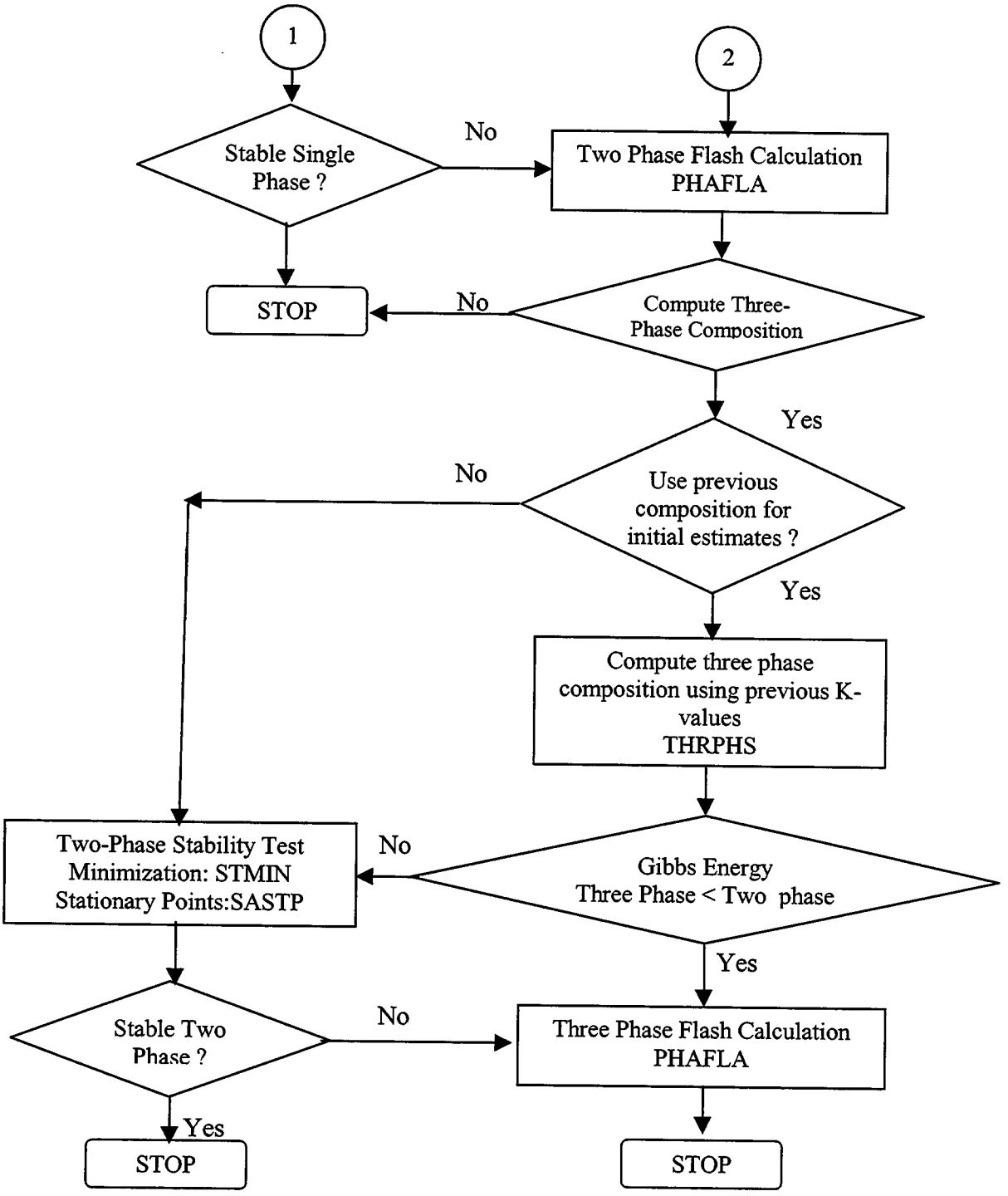
1
2
Stable Single Phase ?
No
Two Phase Flash Calculation PHAFLA
STOP
No
Compute Three-Phase Composition
Yes
No
Use previous composition for initial estimates ?
Yes
Compute three phase composition using previous K-values THRPHS
Two-Phase Stability Test Minimization: STMIN Stationary Points:SASTP
No
Gibbs Energy Three Phase < Two phase
Yes
Stable Two Phase ?
No
Three Phase Flash Calculation PHAFLA
Yes
STOP
STOP

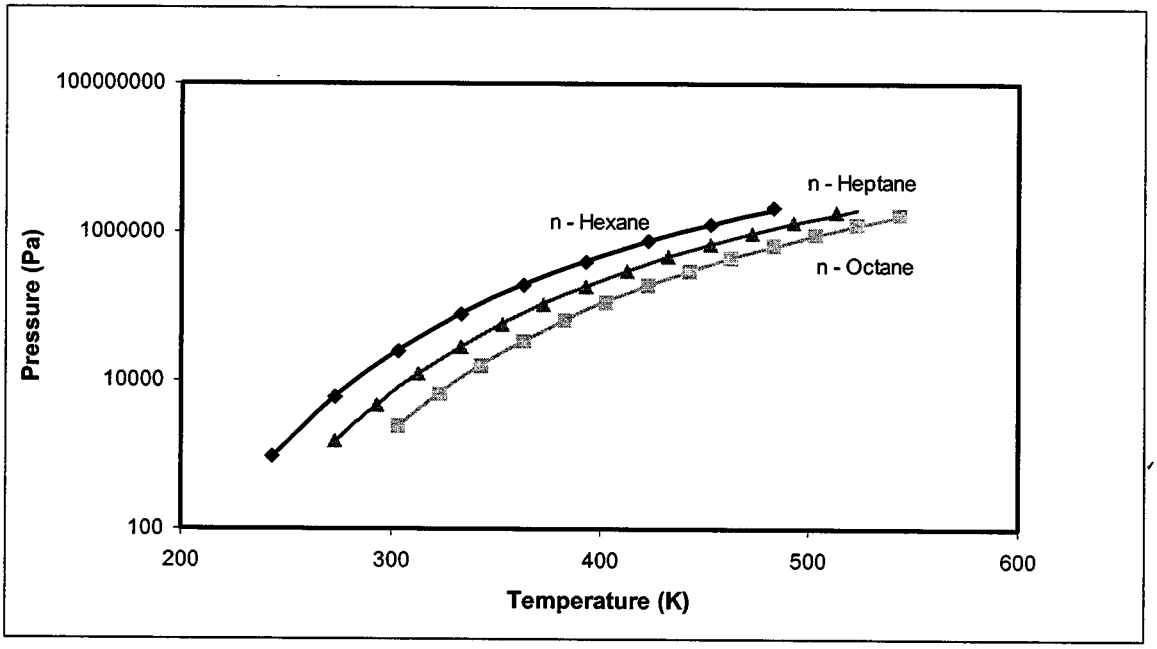

Figure 5.4: Vapor Pressure curves of n–alkanes

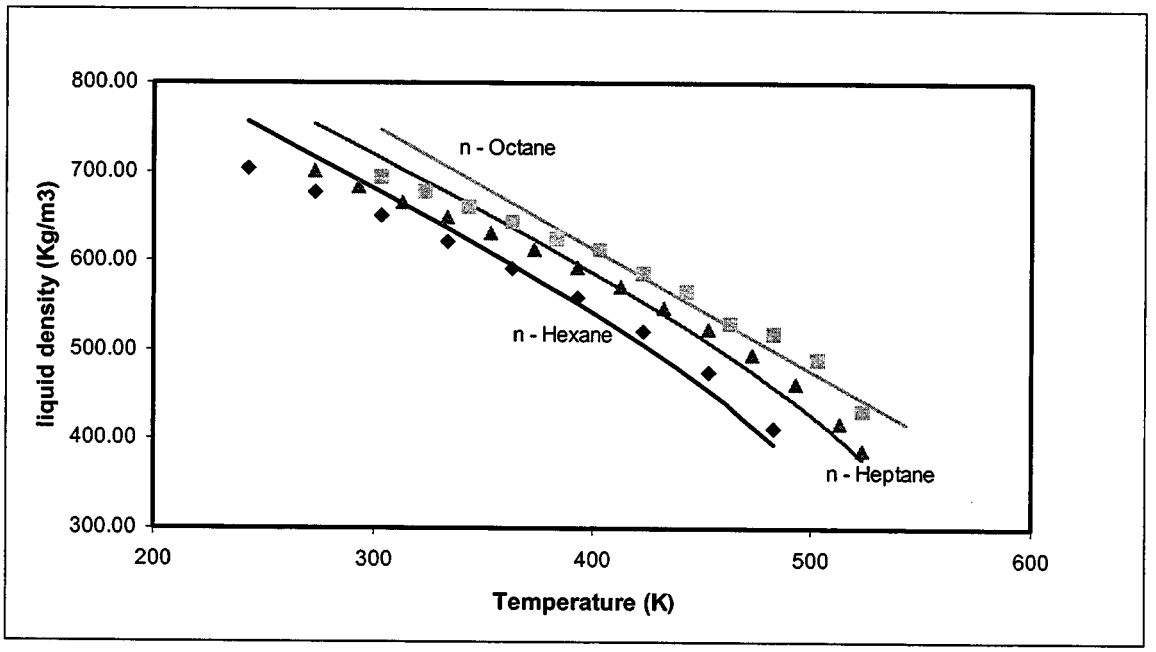

Figure 5.5: Liquid density curves of n–alkanes

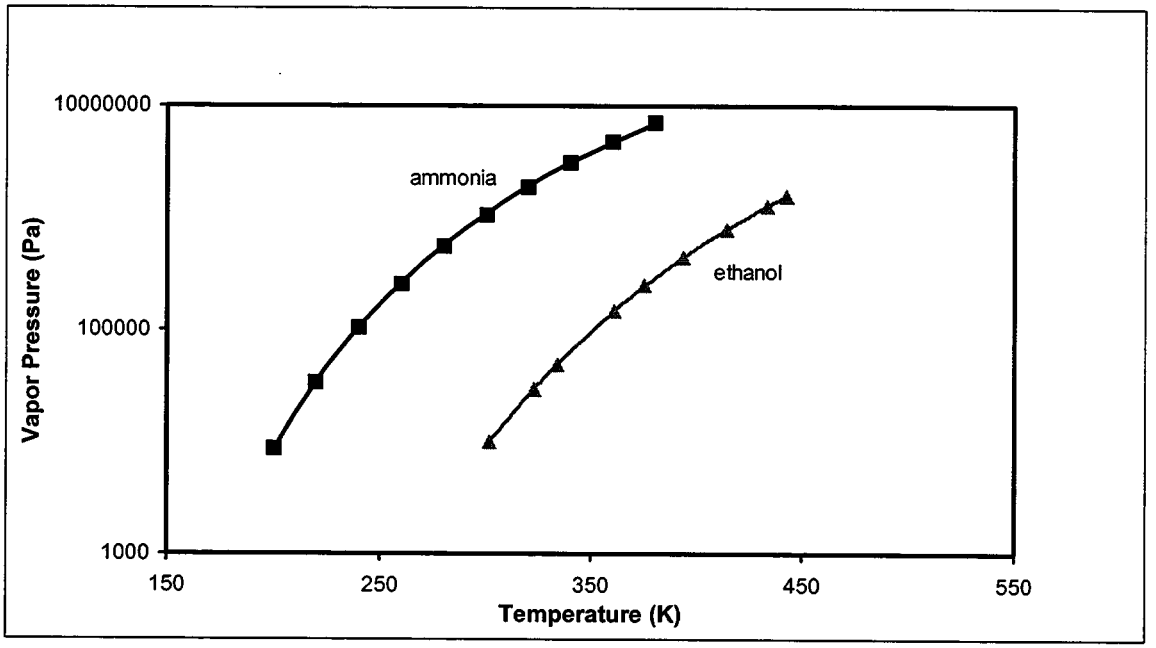

Figure 5.6: Vapor pressure curves for polar compounds

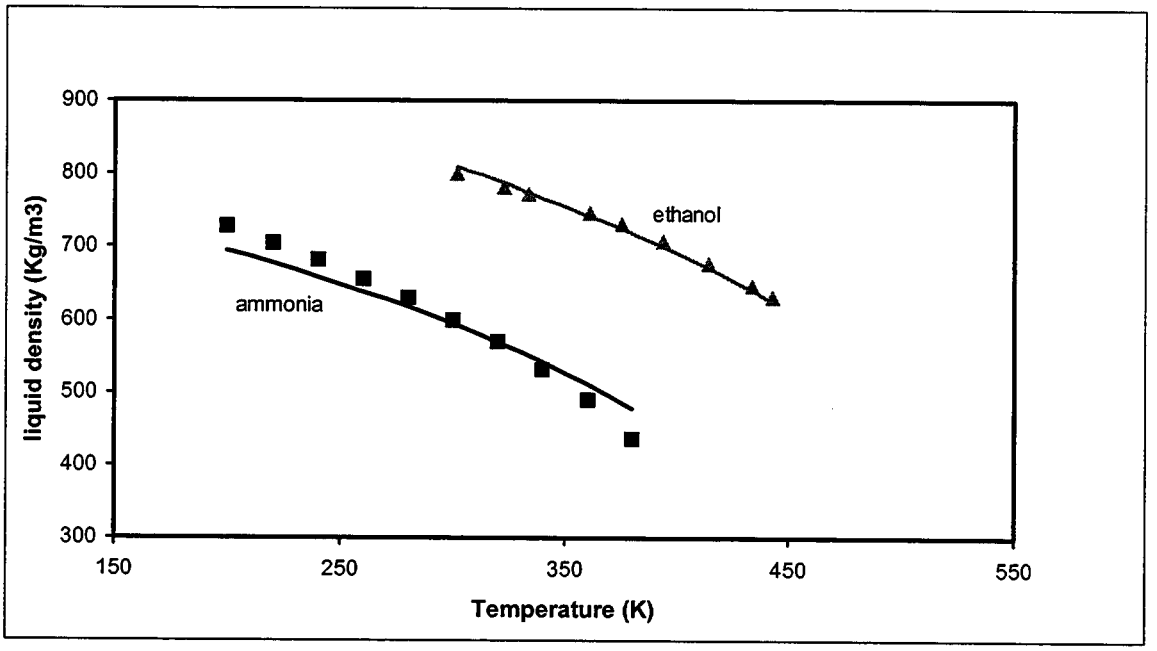

Figure 5.7: Liquid densities of polar compounds

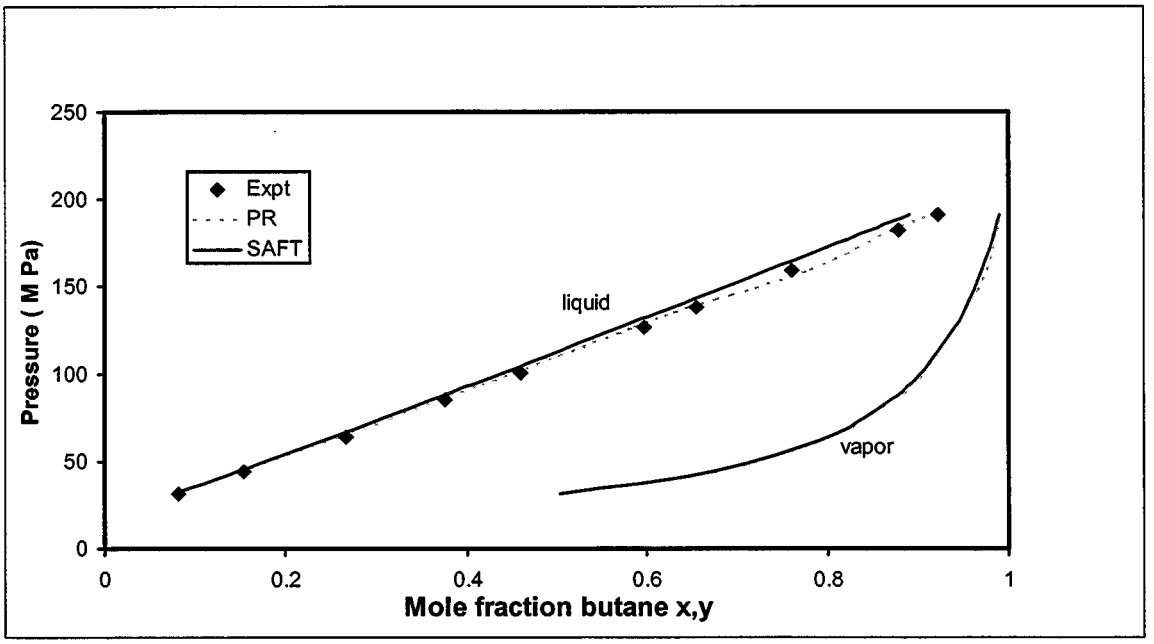

Figure 5.8: Vapor liquid equilibrium for butane-hexane system at 293.15 K

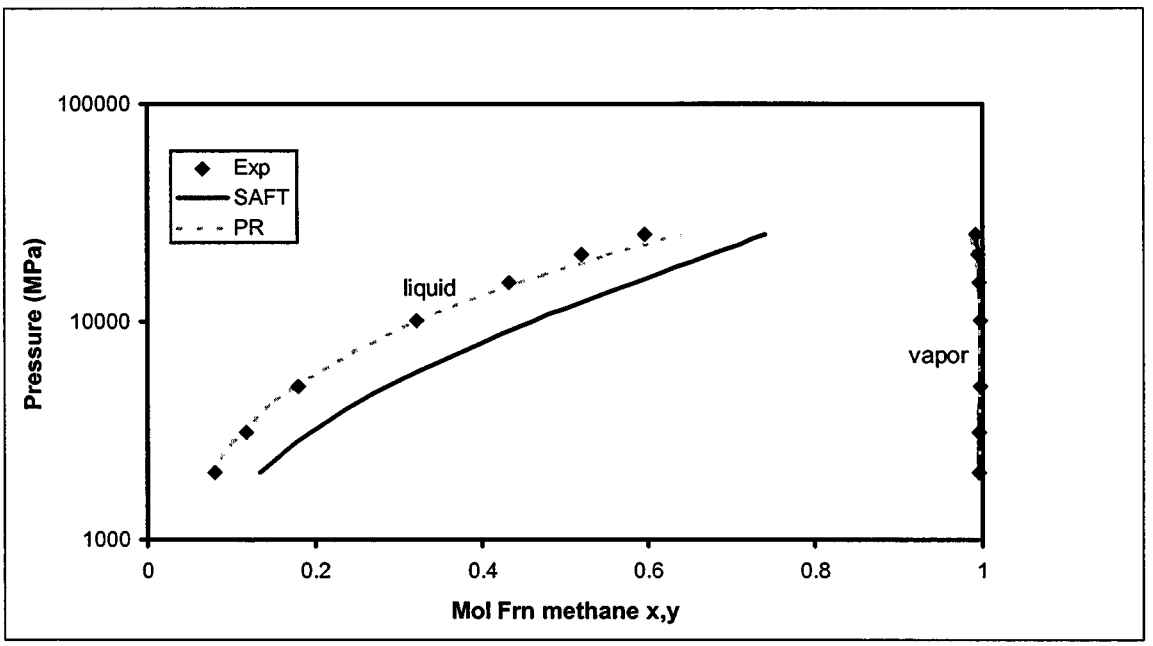

Figure 5.9: Vapor liquid equilibrium for Methane-Hexadecane at 462 K

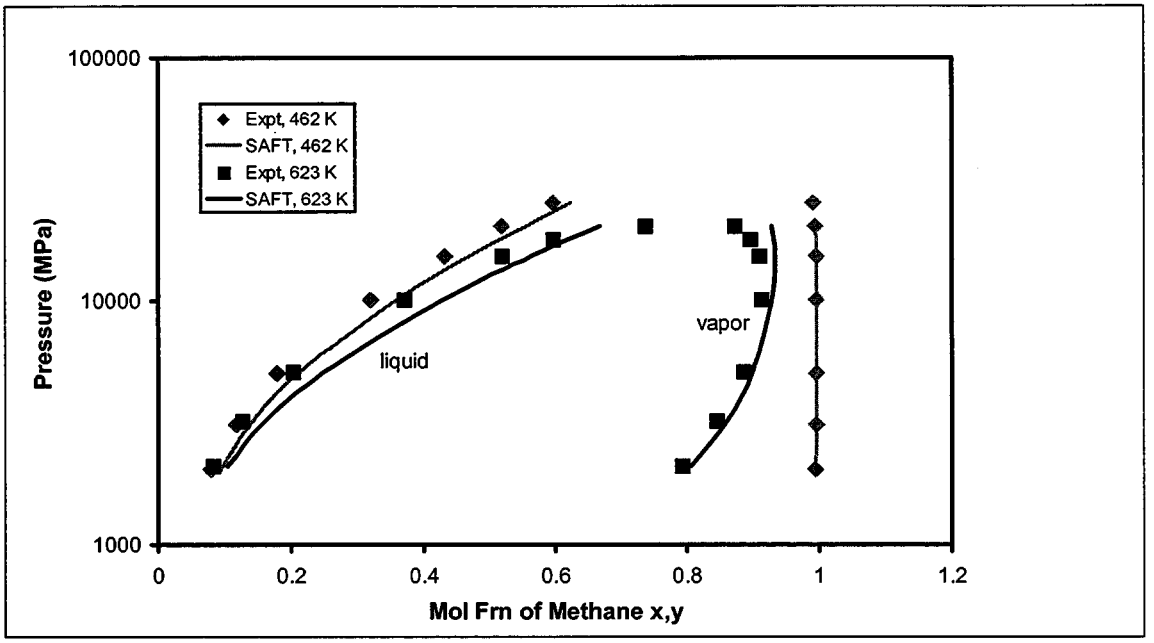

Figure 5.10: Vapor Liquid equilibrium curve for Methane-Hexadecane system at 462 K and 623 K

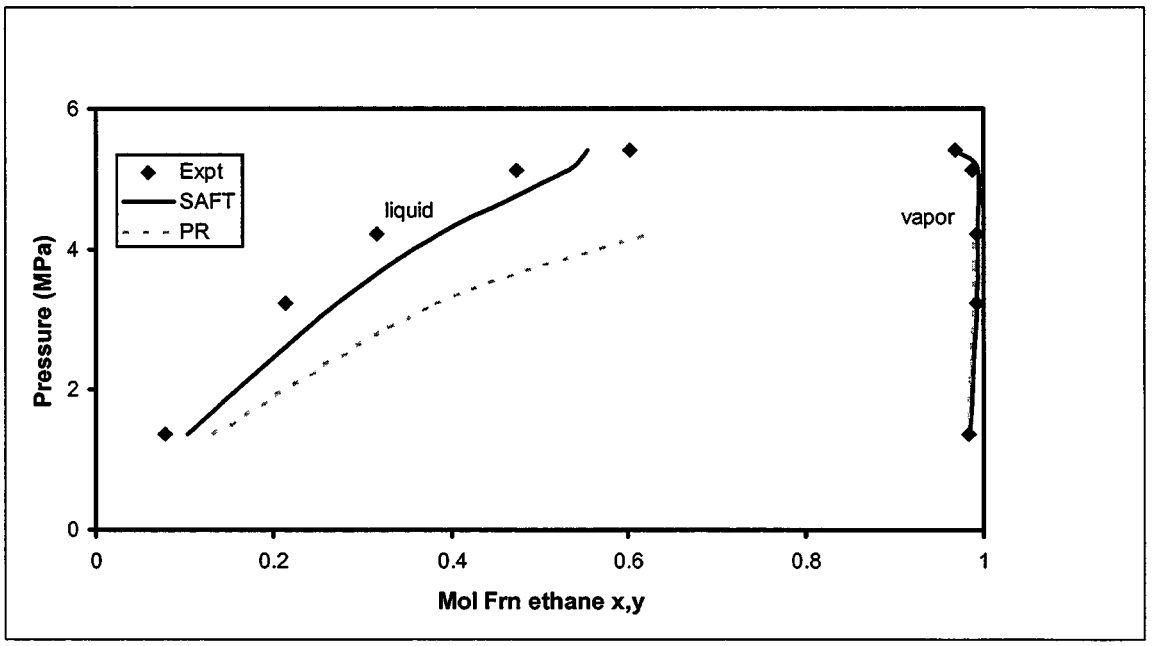

Figure 5.11: Vapor Liquid equilibrium curve for Ethane-Ethanol system at 313.4 K

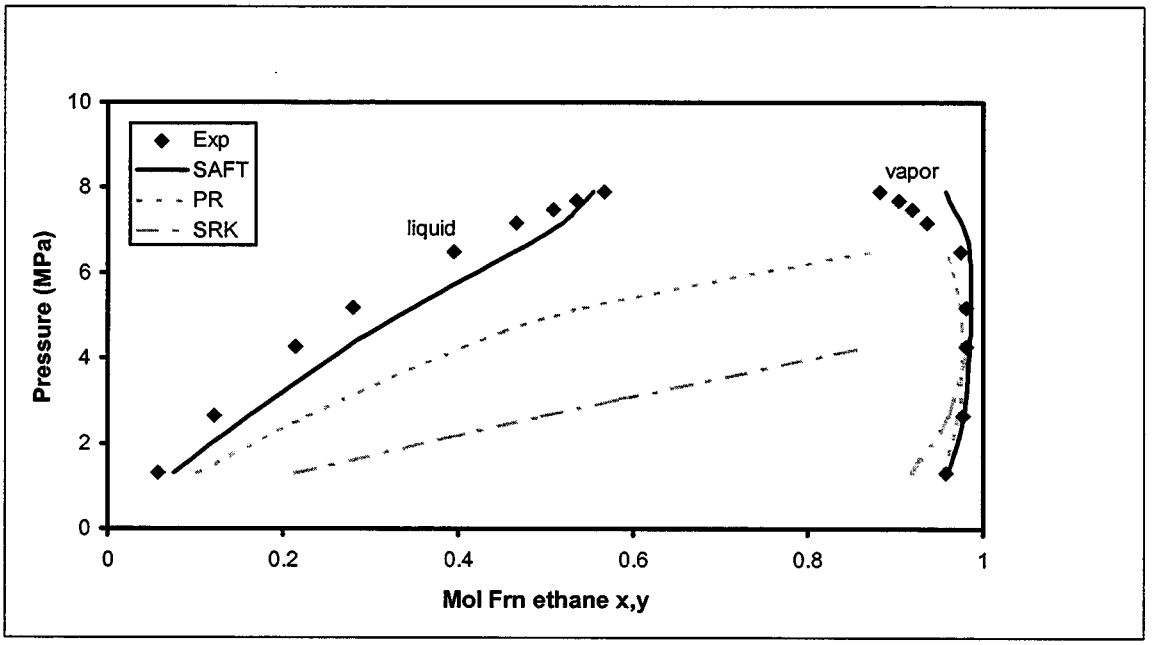

Figure 5.12: Vapor Liquid equilibrium curve for Ethane-Ethanol system at 333.4 K

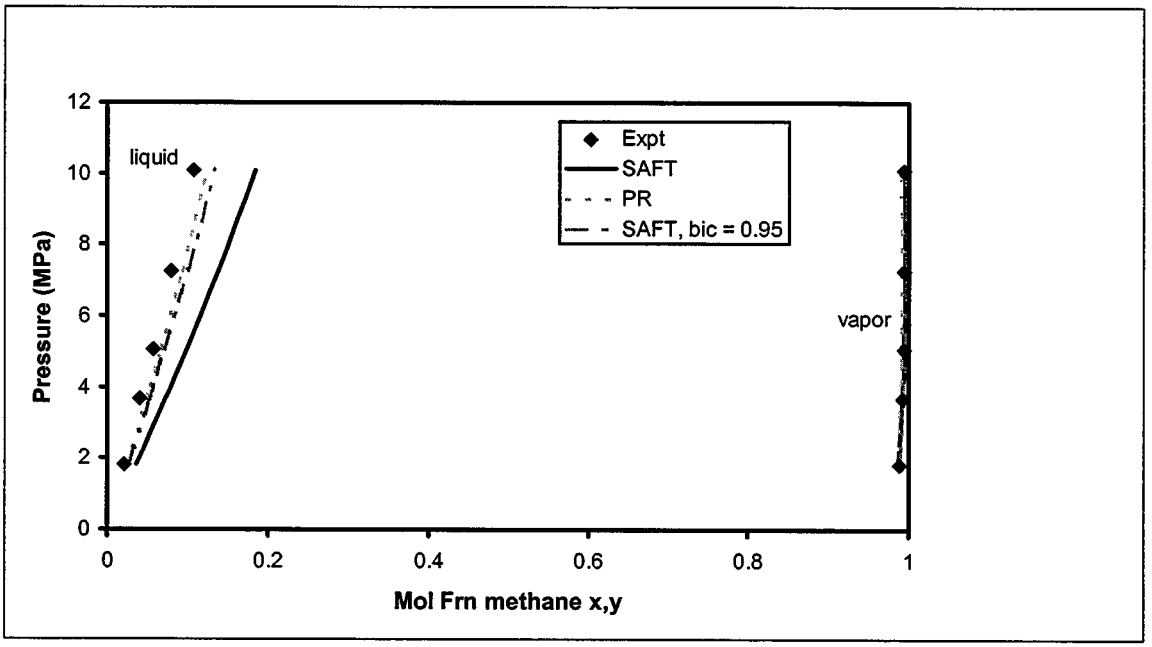

Figure 5.13: Vapor Liquid equilibrium curve for Methane-Ethanol system at 313.4 K

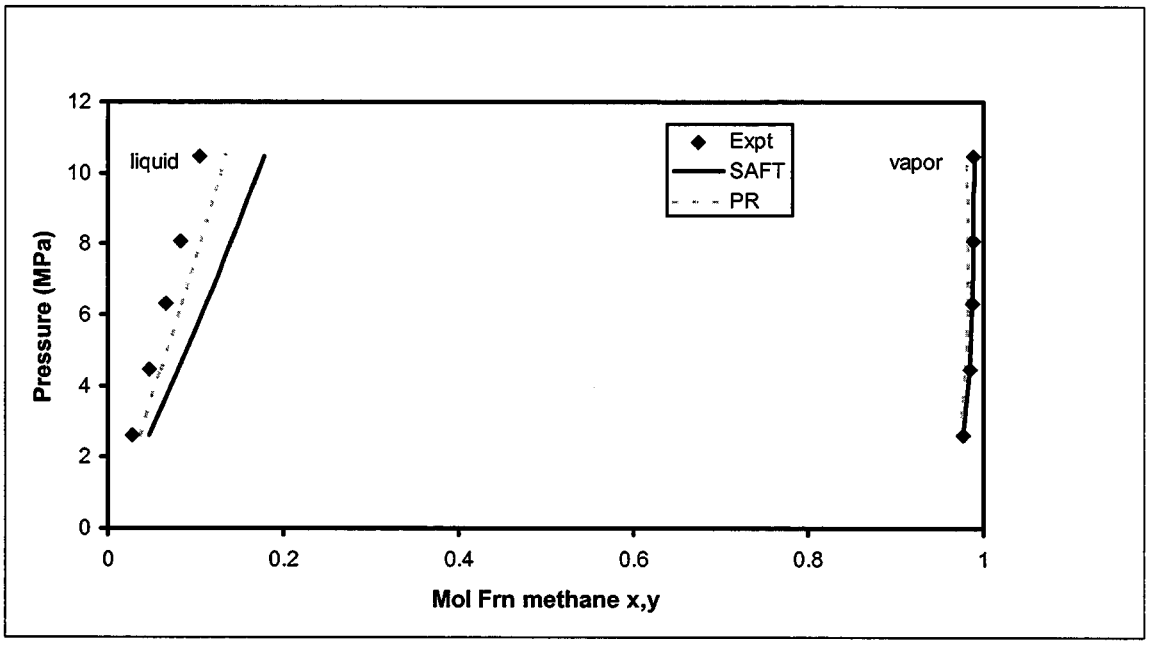

Figure 5.14: Vapor Liquid equilibrium curve for Methane-Ethanol system at 333.4 K

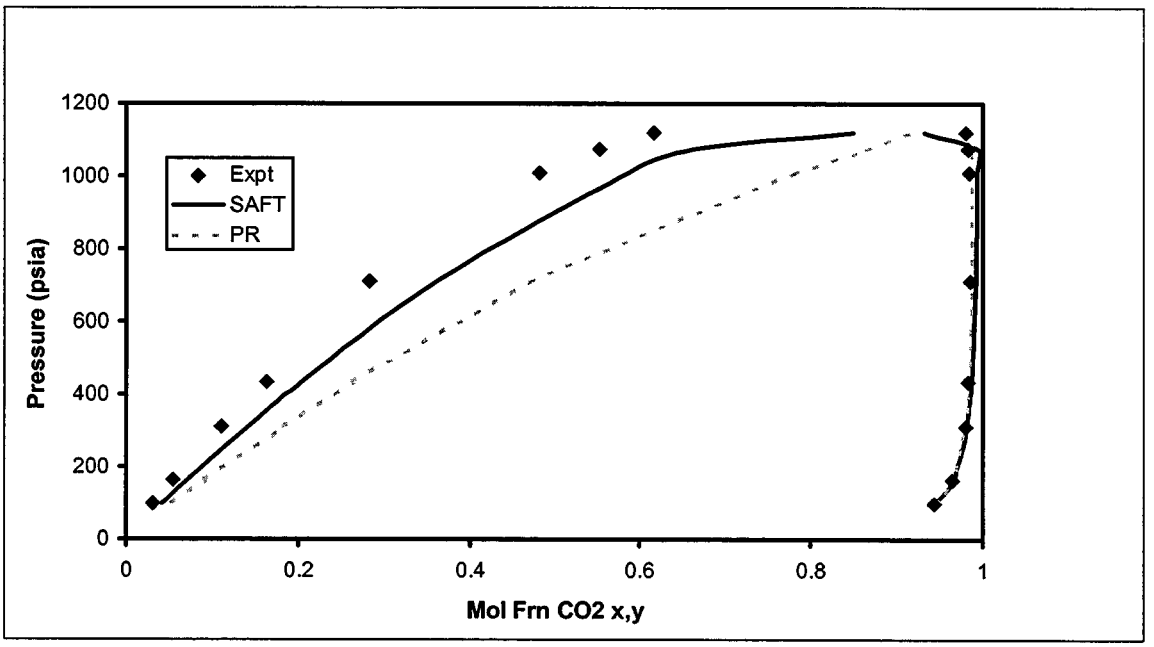

Figure 5.15: Vapor Liquid equilibrium curve for CO2-Methanol at 313.4 K

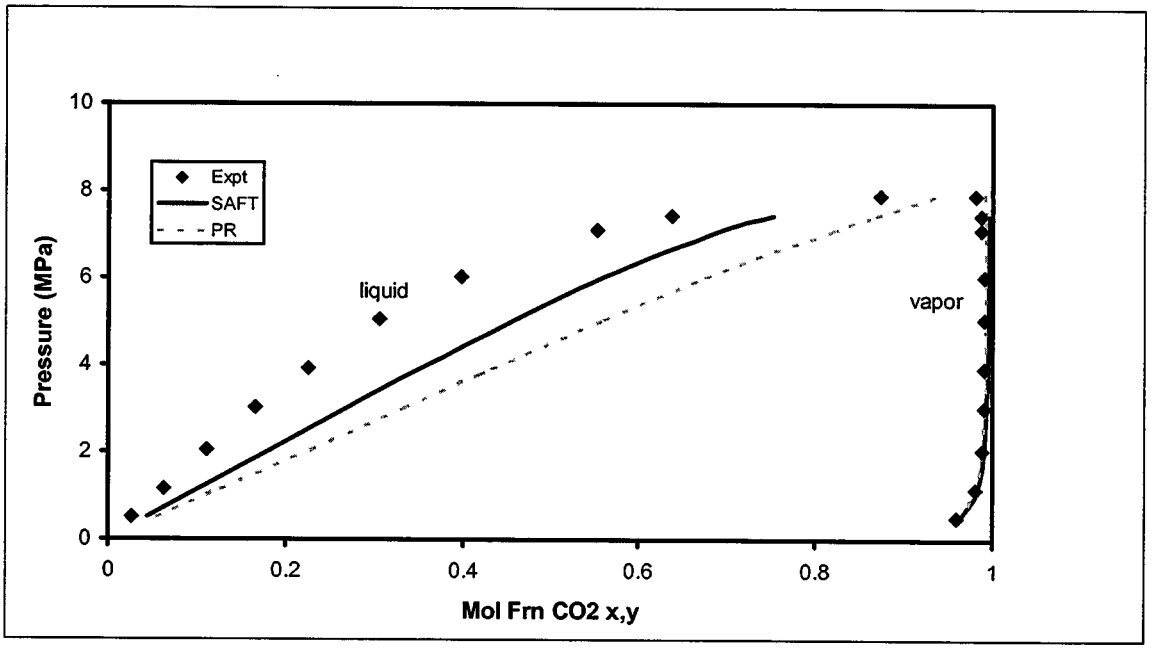

Figure 5.16: Vapor Liquid equilibrium curve for CO2-ethanol system at 313.4 K

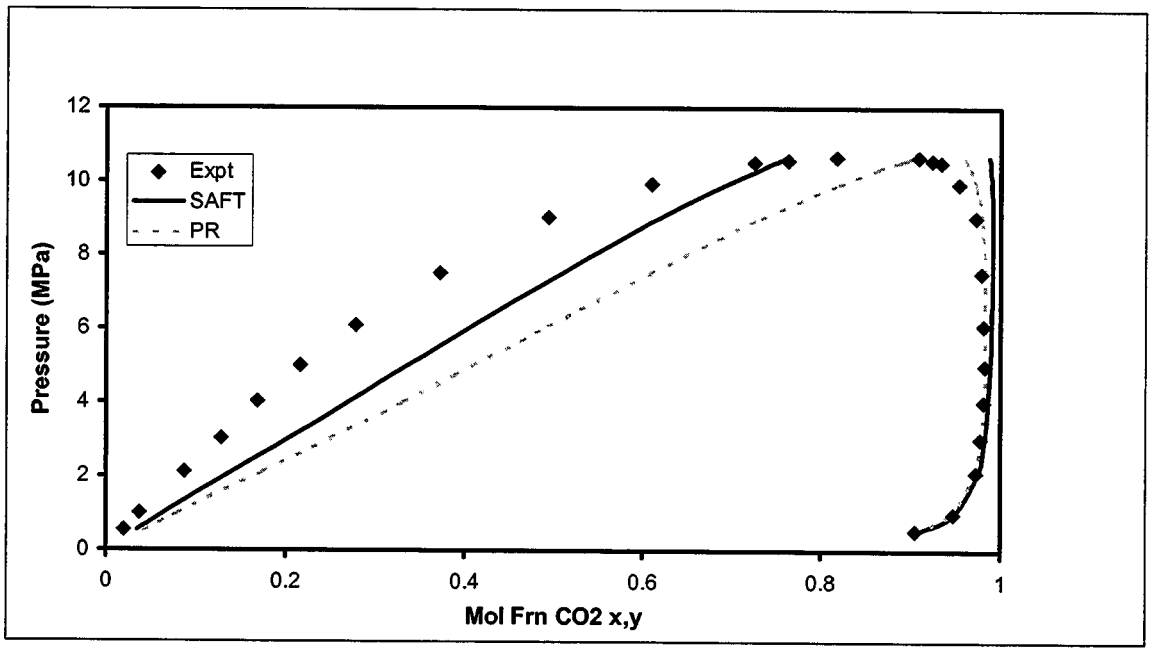

Figure 5.17: Vapor Liquid equilibrium curve for CO2-ethanol system at 333.4 K

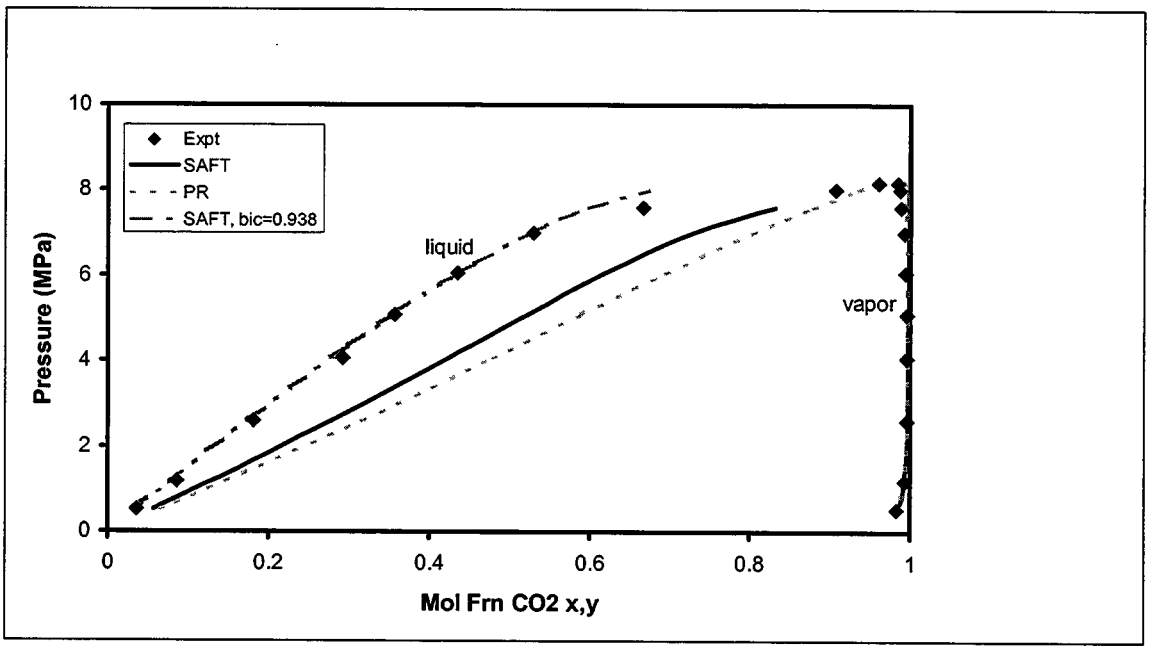

Figure 5.18: Vapor Liquid equilibrium curve for CO2-Propanol at 313.4 K

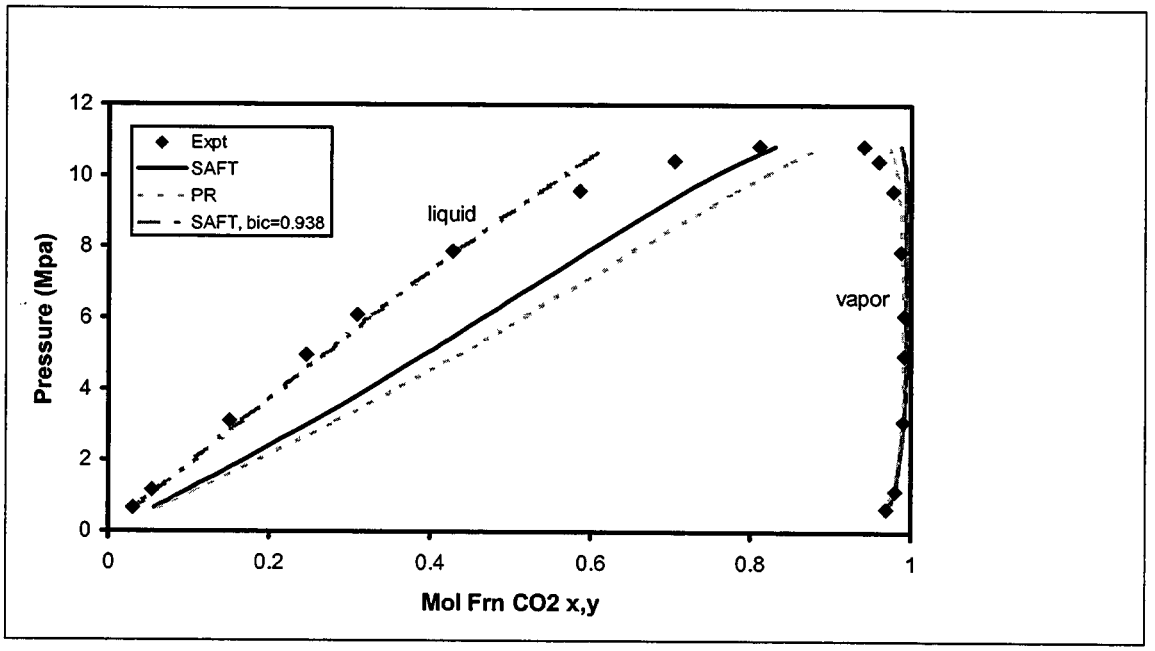

Figure 5.19: Vapor Liquid equilibrium curve for CO2-Propanol system at 333.4 K

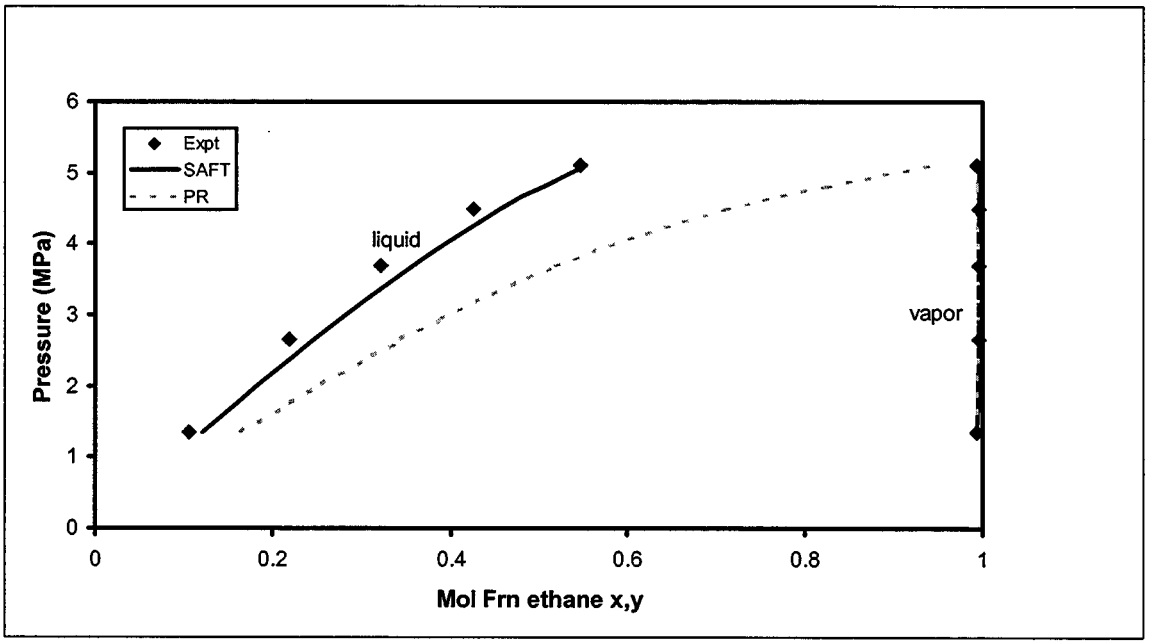

Figure 5.20: Vapor Liquid equilibrium curve for Ethane-Propanol system at 313.4 K

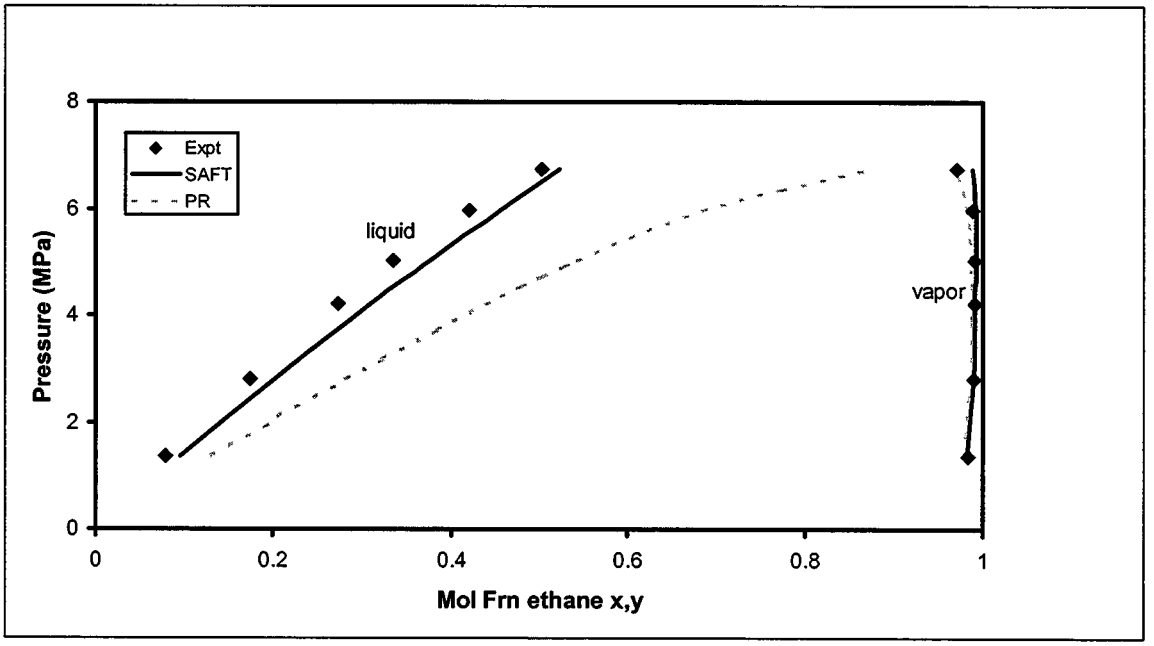

Figure 5.21: Vapor Liquid equilibrium curve for Ethane-Propanol system at 333.4 K

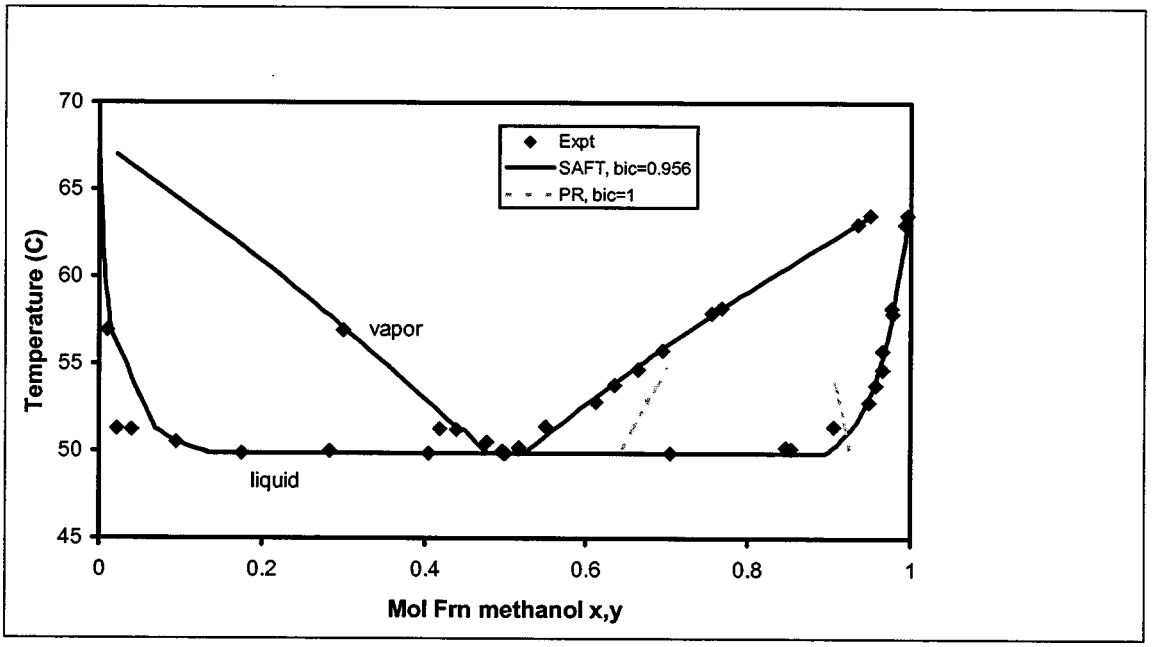

Figure 5.22: Vapor Liquid equilibrium curve for Methanol-Hexane system at 1 atm

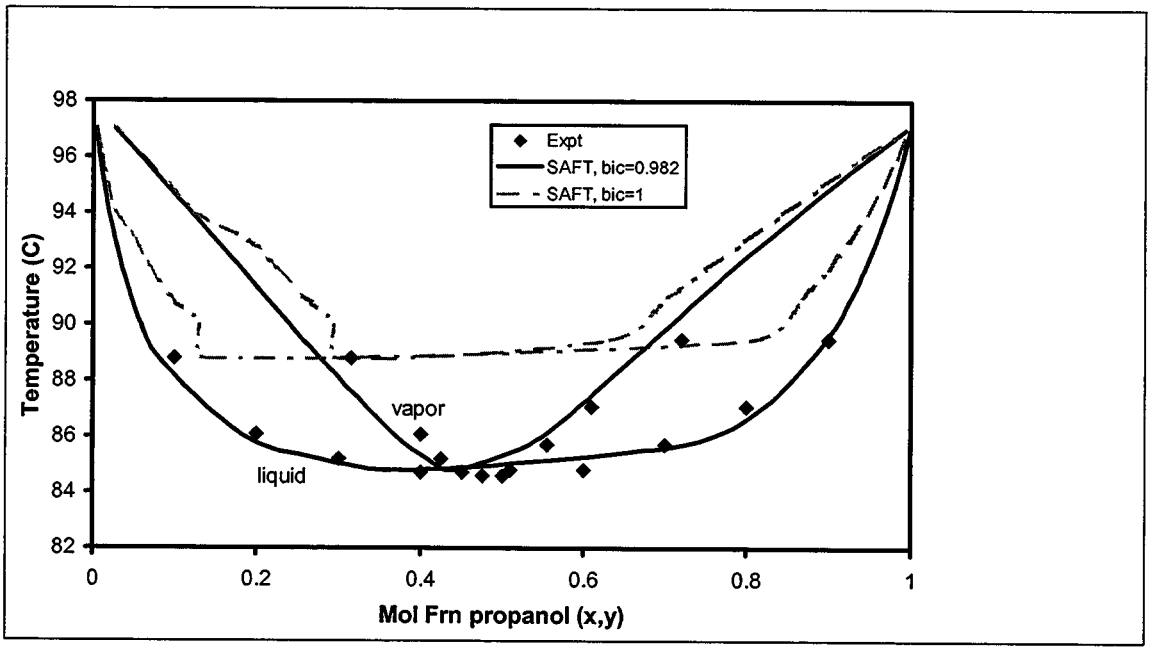

Figure 5.23: Vapor Liquid equilibrium curve for Propanol-Heptane at 1 atm

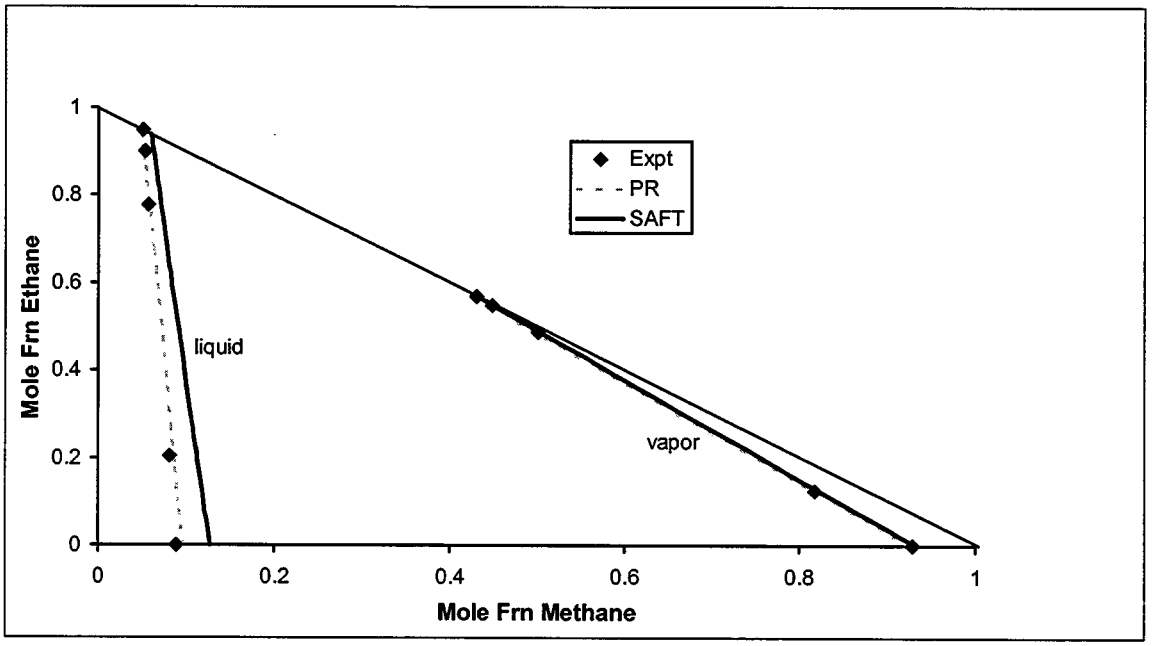

Figure 5.24: VLE curve for Methane-Ethane-Propane system at –75 C, 100 psia

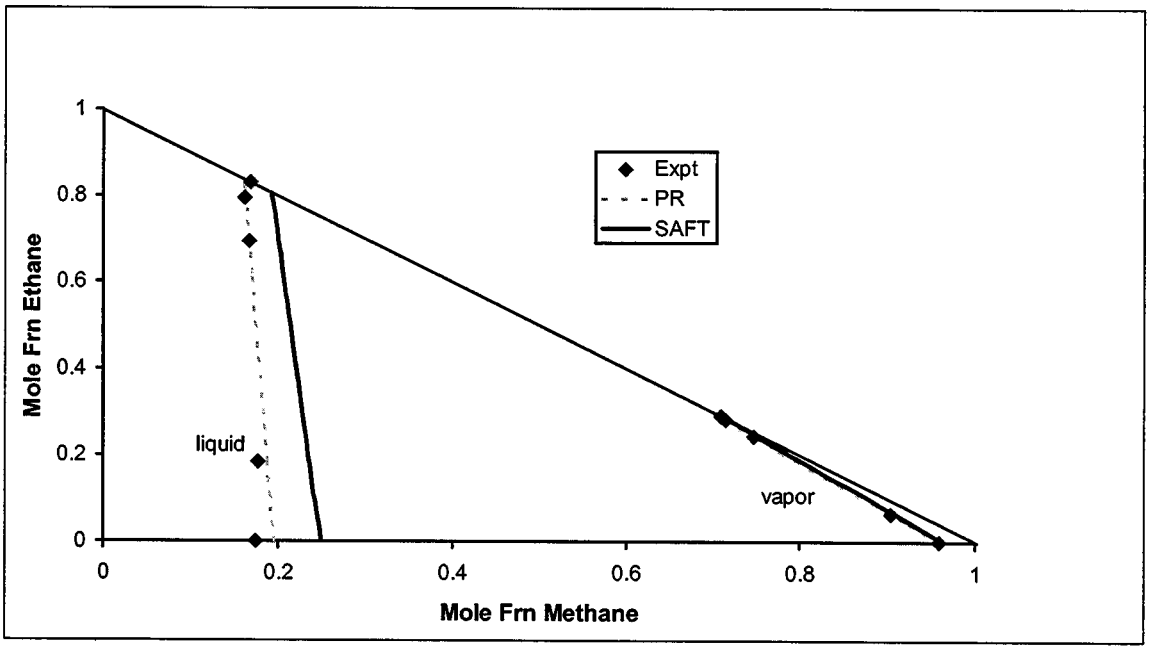

Figure 5.25: VLE curve for Methane-Ethane-Propane system at –75 C, 200 psia

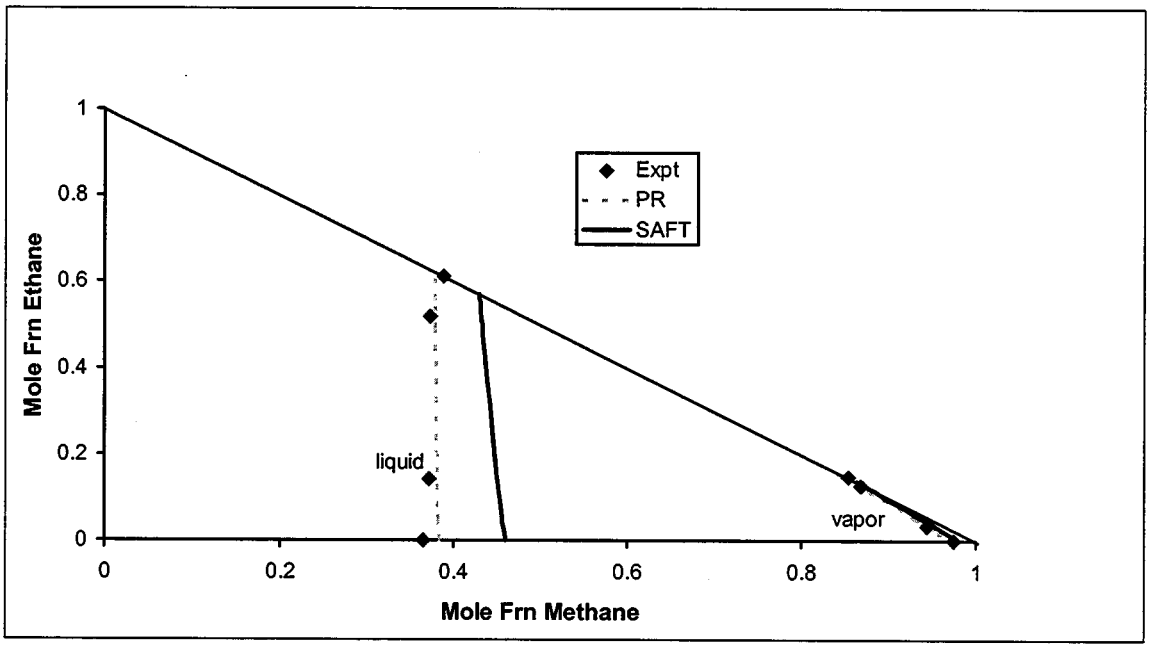

Figure 5.26: VLE curve for Methane-Ethane-Propane system at –75 C, 400 psia

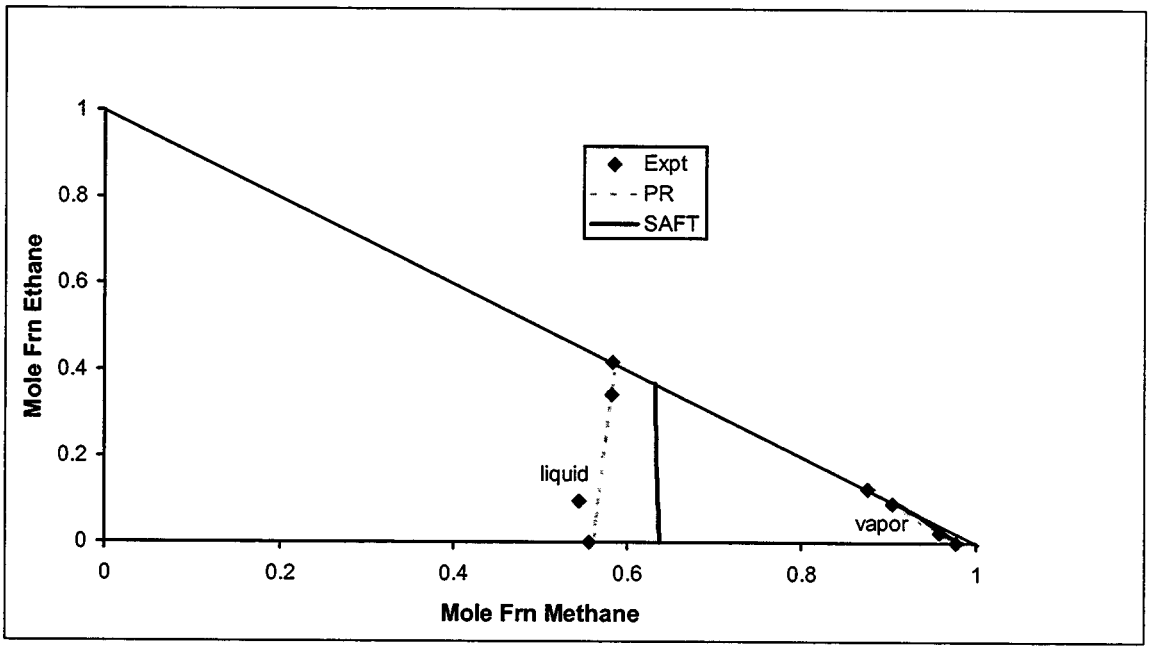

Figure 5.27: VLE curves for Methane-Ethane-Propane system at –75 C, 600 psia

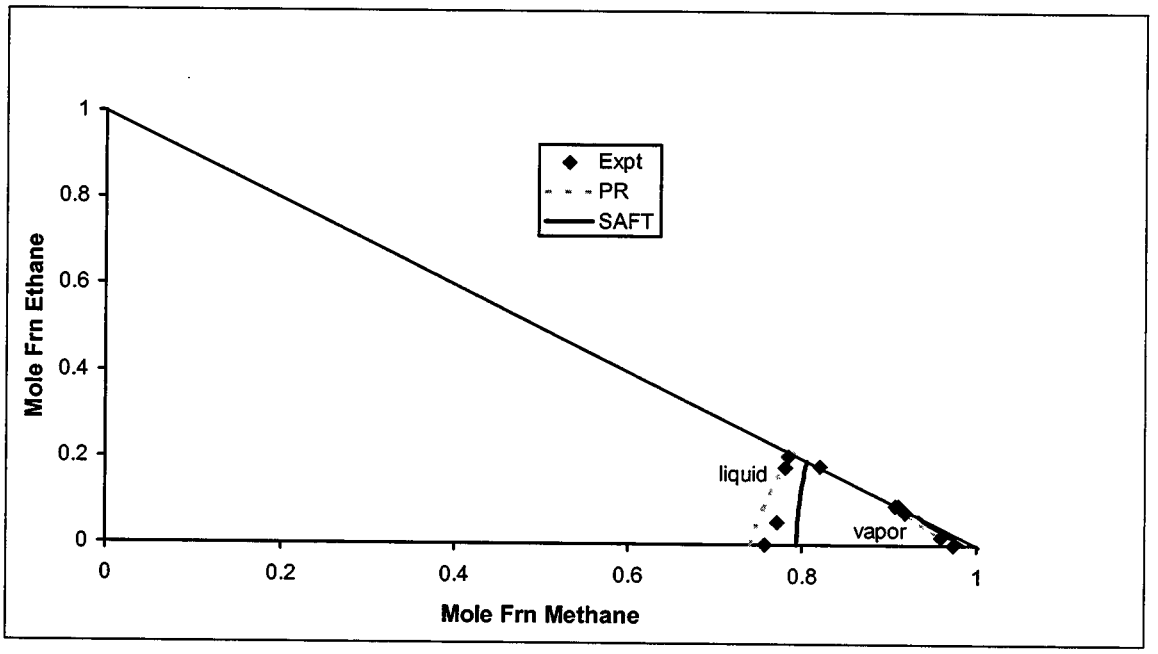

Figure 5.28: VLE curve for Methane-Ethane-Propane system at –75 C, 800 psia

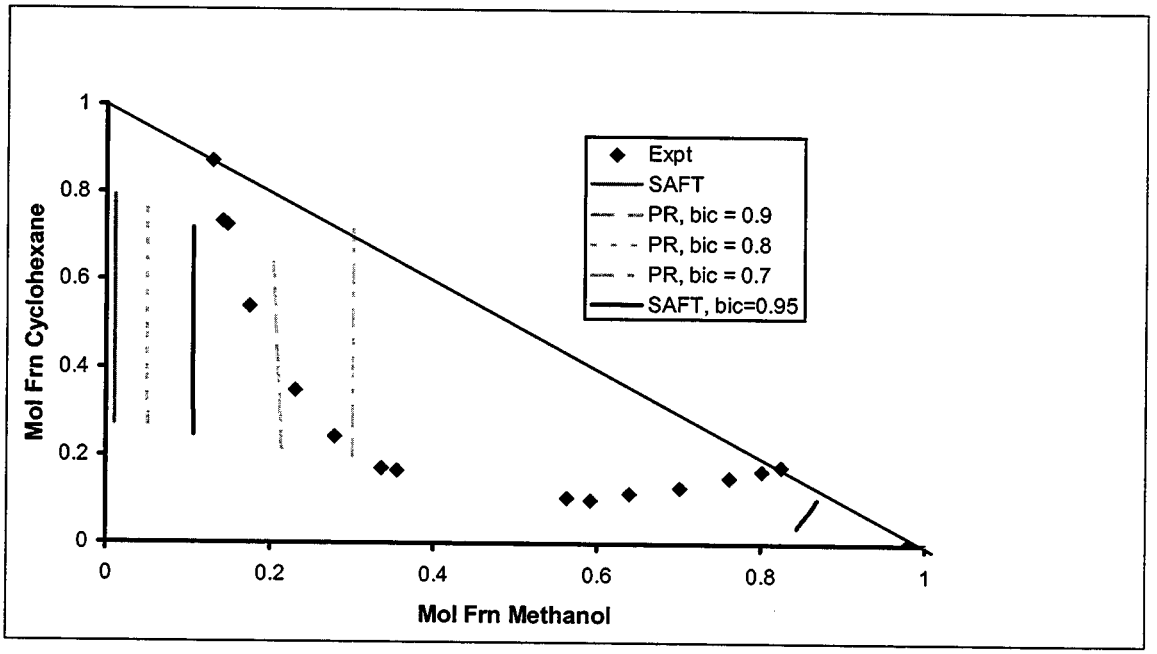

Figure 5.29: VLE curve for Methanol-Cyclopentane-Cyclohexane system at 25 C and 1atm

6. Effect Of Wettability on Displacement Efficiency And Imbibition Behavior

INTRODUCTION

Oil recovery in petroleum reservoirs is greatly affected by fluid-rock and fluid-fluid interactions. These surface chemical interactions directly control rock wettability, capillary pressure curves and relative permeabilities.

It has been generally accepted in the past that while relative permeability to the oil is higher in water-wet rocks the ultimate oil recovery may be higher in mixed-wet and oil-wet rocks. This lower residual oil saturation has been attributed to the presence of thin wetting films of oil on the surface of the rock grains (1, 2). Such continuous wetting oil films allow the oil to drain over a long period of time with very low trapped oil saturations left behind as disconnected oil ganglia. This mechanism has been used to explain high oil recoveries observed in reservoirs in which gravity drainage is the major recovery process. The ultimate oil recovery at the end of a waterflood has been shown to either increase or decrease with increasing oil-wetness (3). In three phase systems an alternative explanation for these high oil recoveries is the drainage of oil films spreading on water in the presence of gas in the pore space.

The importance of wettability in determining oil recovery and relative permeability curves is well established (2). The conditions under which mixed-wettability states are achieved is less well understood. The studies conducted by Basu and Sharma (4, 5) and Buckley et al. (6) point to the importance of crude oil composition in wettability alteration. In addition the wettability state has been shown to be a function of the height above the oil-water contact (7). This dependence on the capillary pressure can be explained on the basis of the critical disjoining pressure that has been measured for both mineral oil and crude oils (8). At capillary pressure above the critical disjoining pressure thin brine films that wet the mineral grains are ruptured and the crude oil wets the grain surface. Since the critical disjoining pressure is a function of the properties of the brine and crude oil and the curvature of the mineral grains there can be a wide range of pressure over which film rupture occurs. It is expected that convex surfaces will be dewet at the lowest capillary pressures in accordance with the augmented Young- Laplace equation. This selective dewetting of surface can give

rise to mixed-wetting conditions over a range of capillary pressures. With this conceptual framework the rock is expected to get progressively more oil-wet as the capillary pressure is increased i.e. the connate water saturation is decreased. This is consistent with the fact that reservoirs tend to be more oil-wet higher in the structure (7).

The centrifuge method is a fast and reliable method for obtaining the desired residual saturations as a function of the capillary pressure. Hirasaki et al. (9,10) presented a detailed analysis for estimating relative permeability and capillary pressure from centrifuge experiments. The modeling approach and assumptions are discussed in these papers.

Filoco et al. (11) have reported the effect of brine salinity and crude oil properties on relative permeability and residual saturations. They have observed that the connate brine salinity had a dramatic influence on the ultimate oil recovery. The effect of salinity on oil recovery depends on the crude oil/brine/rock interactions that are directly linked to the chemistry of all three components.

The objectives of this work are to perform centrifuge coreflow tests with a range of fluids under different conditions of wettability and to clearly identify the factors that influence: (i) the remaining water phase saturation at the end of the primary drainage, (ii) the residual non-wetting phase saturation at the end of the imbibition cycle, (iii) the change in wettability due to aging and (iv) the relative permeability to the non-wetting phase during imbibition. A sequence of drainage and imbibition cycles are conducted using the centrifuge for two and three-phase systems. In regions of low relative permeability (near end points) and in reservoirs where gravity drainage controls the recovery process the centrifuge method offers some clear advantages over other displacement methods.

EXPERIMENTAL METHODS

Fluids Used

The water/oil/gas fluid systems were chosen with the objective of studying the role of crude oil properties on relative permeability and residual saturations. All chemicals used were of analytical grade and were used as received from the manufacturer without any further purification. Brine solutions were prepared using deionized water (Milli-Q Plus, Millipore Corp., Bedford, WA). The solutions were prepared just before use in the experiments. 100 mL of crude oil was mixed with 500 mL brine and left in contact for at

least 24 hours to equilibrate. The equilibrated brine and crude oil were used in the centrifuge experiments. At equilibrium it is expected that components from the oil will also partition into the brine phase. The gas phase is air.

The oil phases used were decane, Produe Bay and Moutray crude oil. Produe Bay crude is very well studied oil with a lot of published data in the literature. Figure 6.1 shows the zeta potenial of Prudhoe Bay at different pH. Figure 6.2 shows the IFT values of this crude oil at different pH and ionic strength (12).

Core Preparation

A total of 40 core plugs (2.5 cm in diameter and 2.5 cm in length) were cut from a large optically homogeneous slab of Berea sandstone and Texas Cream Limestone using tap water as the cutting fluid. The core plugs were dried in an air-oven at 100 °C for at least 24 hours and then evacuated and saturated in a dessicator during a period of 12 hours prior to weighing. The core porosities varied from 19.7% to 21% for Berea and 17% to 20 % for the Texas Cream limestone and the absolute permeability varied from 180 mD to 220 mD for the Berea sandstone and 10 mD to 15 mD for the limestone.

Interfacial Tensions Measurements

The interfacial tension between brine and crude oil was measured by a DuNouy ring tensiometer. The instrument consists of a platinum-iridium ring supported by a stirrup attached to the beam of a torsion balance. The flamed ring was placed at the interface of two liquids or at the surface of a liquid with air. It was than pulled upward until it breaks free of the liquid and moves into the second liquid or into the air. The force that is just required to break the ring free of the liquid/liquid or liquid/air interface is proportional to the surface tension. The manufacturer has designed the instrument so that the dial reading is the apparent interfacial or surface tension. We can correct this apparent surface tension to obtain the true surface tension by multiplying by a correction factor (F) based on the geometry of the instrument. The correction factor is normally very close to one. The correction factor was obtained by measuring the IFT of a water-air interface.

Centrifuge Experiments

The apparatus consists of a Beckman high-speed ultra-centrifuge (maximum speed of 20,000 rpm), a stroboscope, an electrical timer, and a device for mounting the cores in the centrifuge for drainage and imbibition. The centrifuge has an observation window and is equipped with a heater and a cooler to accurately control the temperature during the measurements. The fluid production from the cores is observed through a transparent glass window with the help of a stroboscope. The core-mounting device is composed of six core holders with graduated plastic collection tubes. A simple and inexpensive video setup was prepared in order to obtain accurate data for very early times. A video camera was placed over the observation window of the centrifuge (see fig. 6.3). It is very important to record the first few minutes of each test. The fluid production was recorded manually by viewing the tape in slow motion. O'Meara and Lease (12) solved the same problem using an automated centrifuge apparatus that uses a linear photodiode array in conjunction with a microcomputer to image and identify liquids recovery from centrifuged core samples.

The centrifuge method consists of increasing the centrifuge speed in steps and measuring at each step the amount of fluid produced from a core as a function of time and at equilibrium when flow has ceased. At each speed, the equilibrium saturation and capillary pressure is used to obtain the capillary pressure curve, and the transient behavior is used to infer the relative permeability of the displaced phase.

The cores, previously dried and weighted, are saturated with the specified brine using a dessicator. A drainage centrifuge displacement is run, displacing the brine with crude oil until residual water saturation is achieved. The volume of wetting phase collected as a function of time is recorded at each centrifuge speed. The remaining water saturation at each rpm is also recorded to obtain the capillary desaturation curve for the wetting phase.

The imbibition curve was obtained by centrifuge displacement of oil by brine/air in the presence of connate water using imbibition centrifuge buckets. The oil-saturated core was placed in the bottom of the bucket and the polycarbonate receiving tube sits on the top of the rock core. The first few minutes are recorded with the video camera for more precise early readings and the test stops when the production of oil ceases. For our test conditions relatively little flow occurs after 30 min to 1 hour. To ensure equilibrium the core was spun at each rpm from 4 hours to 16 hours.

At any stage of the centrifuge experiment, the highest capillary pressure occurs at the inlet face of the core at r_1. At the inlet face, the capillary pressure is:

$$P_c = \frac{\Delta\rho\omega^2}{2}(r_2^2 - r_1^2) \qquad [6.1]$$

where Pc = capillary pressure at core inlet, dynes/cm^2, r_1 = radius of core inlet face measured from the center of rotation, cm, r_2 = radius of core outlet face measured from the center of rotation, cm, ω = angular velocity (= $2\pi N/60$, where N = centrifuge speed in revolutions per minute), radians/second and $\Delta\rho$ = (density of water – density of oil), gm/cm^3.

The average water saturation of a core for drainage is given by: Swav = (PV-V)/PV, where PV = pore volume of the core and V = the amount of water displaced by oil. The relative permeability curves for the displaced phase were calculated using the method presented by Hagoort (13) and O'Meara (12). This method provides an easy analytical way of analyzing the data.

The outlet saturation of phase i $\left(S_i^*\right)$ is given by,

$$S_i^* = S_i^o - N_i + \tau\frac{dN_i}{d\tau} \qquad [6.2]$$

Relative permeability of phase i (k_{ri}^*) is given by,

$$k_{ri}^* = \frac{\phi\mu_i(r_2 - r_1)}{\omega_\infty^2 Rk(\rho_i - \rho_n)}\frac{dN_i}{d\tau} \qquad [6.3]$$

where the effective time (τ) is,

$$\tau = \frac{1}{\omega_\infty^2}\int_0^t \omega^2(t')dt' \qquad [6.4]$$

RESULTS AND DISCUSSION

Table 6.1 gives the properties of the oil used and Table 6.2 gives the surface and interfacial tension of the different liquid systems used in this research. Figure 6.4 shows the capillary desaturation curve where the non-wetting phase was Prudhoe Bay crude oil (Fig. 6.4a), or decane (Fig. 6.4b) or air (Fig. 6.4c), and Berea was used as porous medium. Figure 6.5 shows capillary desaturation curve where the non-wetting phase was Prudhoe Bay crude oil (Fig. 6.5a) or air (Fig. 6.5b) and Texas Cream limestone (LS) was used as porous medium. Similar results are observed for the two porous mediums. The S_{wr} at high Pc was lower when the water was displaced by air (0.12) as compared to oil (0.42).

Important differences in the shape of the wetting phase capillary desaturation curves are observed (after primary and secondary drainage) when crude oil was used as non-wetting phase compared to the system where decane and air are used as non-wetting phase. Similar trends were observed in both cases of Berea and limestone. The S_{wr} after primary drainage was 0.22, whereas after secondary drainage the value was 0.40 for Berea/Prudhoe Bay system. But for decane/Berea and air/Berea system the difference between S_{wr} of primary and secondary drainage was only 0.02 and 0.05 respectively.

For LS/crude oil system the difference of S_{wr} after primary and secondary drainage was high (0.23) as compared to the difference of S_{wr} after primary and secondary drainage of LS/air system (0.01). The possible explanation of these observations was that the pore space progressively becomes more oil-wet due to film rupture as the capillary pressure was raised. This implies that the water flooding brine during imbibiton sees a different porous medium, which is now mixed wet or partially oil wet. As a consequence the brine during imbibition would tend to go into the largest of the oil-wet pores and of course continue to flow through the smallest pores which have not been contacted by oil during drainage and hence are still water-wet. This creates a very different fluid distribution (Figure 6.6) than it would have achieved if the core were oil-wet to begin with. Waterflood brine would, therefore, be excluded from the intermediate size pores that have remained oil-wet. The fraction of such pores depends on the capillary pressure imposed during drainage. The reassignment of pore occupancy caused by change in wettability during primary drainage was likely the reason for a large fraction of the water being trapped during secondary drainage and as a result the considerable difference in S_{wr} after primary and secondary drainage was observed.

The oil recovery achieved in these systems during imbibition process where air or brine displaces oil at connate water saturation are shown in Figure 6.7. The result for imbibition was dramatically different. It was evident that significantly higher oil recoveries are obtained when air displaces oil (~65%) compared to brine displaces oil (~13.8%) at same capillary pressure. Percentage of oil recovery was higher in sandstone as compared to limestone.

Table 6.3 gives the wettability indices of the systems studied in this research. Results show that residual oil saturation decreases with an increase in salinity. Both LS and SS cores become more susceptible to wettability alteration as the salinity was increased. Aging the samples with crude oil also impacts the wettability of the core. Aging the samples for 20-30 days with Moutray crude oil results in a change in wettability of the cores. The oil recovery increases by 10-15% to more than 95% in SS and LS cores (Figure 6.8). These results show that with time the crude oil changes the wettability of the core from strongly water wet to mixed wet, which leads to higher oil recovery. The measurement of water-amott index for Moutray-LS samples in table 6.3 shows that the index reduces with aging, indicating change in wettability of the core. This change was also evident from the differences observed in residual brine saturation observed during primary and secondary drainage.

CONCLUSIONS AND FUTURE PLANS

The centrifuge has the potential to measure capillary pressure curves, wettability index and residual oil saturation on multiple cores in a reasonable short period of time. From the capillary desaturation curves (primary and secondary drainage) it was observed that the wettability of the core changes from water-wet to mixed-wet. It can be concluded that it is no longer sufficient to know what the original wettability of the rock is but to be able to track changes in the wettability as the rock undergoes cycles of drainage and imbibition.

The effect of connate brine salinity, displacing brine salinity, crude oil composition and estimation of relative permeability will be studied. Models for estimating residual saturations of wetting and non-wetting phases in a centrifuge experiment and in displacement experiments will be tested against experimental data. Impact of aging on wettability and oil recovery with Prudhoe bay crude oil on SS and LS cores is being studied. This work is in the progress.

REFERENCES

1. Anderson, G. W.: " Wettability Literature Survey – Part 5: The Effects of Wettability on Relative permeability," *JPT* (November 1987) 1453.

2. Salathiel, R. A.: "Oil Recovery by Surface Film Drainage in Mixed-Wettability Rocks," *JPT* (October 1973) 1216.

3. Morrow, N. R.: "Wettability and its Effect on Oil recovery," *JPT* (December1990) 1446.

4. Basu, S. and Sharma, M. M.: "Characterization of Mixed Wettability States in Oil Reservoirs by Atomic Force Microscopy," SPE J, SPE 35572, December 1997.

5. Basu, S. and Sharma, M. M.: "Investigating the Role of Crude Oil components On Wettability Alteration Using Atomic Force Microscopy," proceedings of the SPE International Symposium on Oilfield Field Chemistry, SPE 37231, Houston, TX, February 18-21, 1997.

6. Buckley, J. S.; Liu, Y. and Monsterleet, S.: "Mechanisms of Wetting Alteration by Crude Oils," SPE 37230, Presented at the SPE International Symposium on Oilfield Chemistry, Houston, TX, February, 1997.

7. Jerauld, G. R. and Rathmell, J. J.: " Wettability and Relative Permeability of Prudhoe Bay: A Case Study of Mixed-Wet Reservoirs," SPE Reservoir Engineering, February 1997, 58.

8. Basu, S. and Sharma, M. M.: "Measurement of Critical Disjoining Pressure for Dewetting of Solid Surfaces," The Journal of Colloid and Interface Science, 181, 443-455, August 1996.

9. Hirasaki,G. J.; Rohan, J. A. and Dudley II, J. W.: "Interpretation of Oil/Water Relative Permeabilities from Centrifuge Displacement," SPE 24879, Paper presented at the 67th Annual Technical Conference and Exhibition of the SPE,

Washington, DC, October 4-7, 1992.

10. Hirasaki,G. J.: "Dependence of Waterflood Remaining Oil Saturation on Relative Permeability, Capillary Pressure and Reservoir Parameters in Mixed-wet, Turbidite Sands," SPE 30763, Paper presented at the SPE Annual Technical Conference and Exhibition, Dallas, TX, October 22-25, 1995.

11. Filoco, P. R. and Sharma, M. M.: "Effect of Brine Salinity and Crude Oil Properties on Relative Permeabilities and Residual Saturations," SPE 49320, Paper presented at the SPE Annual Meeting, New Orleans, LA, September 1998.

12. O'Meara Jr, D. J. and Lease, W. O.: "Multiphase Relative Permeability Measurements Using an Automated Centrifuge," SPE 12128, Paper presented at the SPE Annual Meeting, San Francisco, October 1983.

13. Hagoort, J.: "Oil Recovery by Gravity Drainage," *SPEJ* (June 1980), 139.

Table 6.1: Properties of the crude oils used

Crude oil	Acid number/Base number	Density (gm/cc)	Viscosity (cp)
Prudhoe Bay	0.15 / 2.28	0.91	22
Moutray	0.26/	0.845	5.25

Table 6.2 : Wettability indices measured for different fluid pairs

Porous media	Systems	Water-Amott	Oil-Amott
Texas cream limestone	0.3% (NaCl) Brine-AK 93	0.556	0
	3.0% (NaCl) Brine-AK 93	0.50	0
	20% (NaCl) Brine-AK 93	0.467	0.136
	4% (NaCl) +0.5% ($CaCl_2$)-Moutray	0.242	0
	4% (NaCl) +2.0% ($CaCl_2$)-Moutray	0.276	0
Aged sample	4% (NaCl) +0.5% ($CaCl_2$)-Moutray	0	0
	4% (NaCl) +2.0% ($CaCl_2$)-Moutray	0.016	0
Berea Sandstone	4% (NaCl) +0.5% ($CaCl_2$)-Moutray	0.181	0
	4% (NaCl) +2.0% ($CaCl_2$)-Moutray	0.361	0
	3% brine-decane	0.462	0

Table 6.3: Surface and interfacial tension of the fluid systems used

Fluid System	σ_{wg} / σ_{og} / σ_{ow} (Dynes/cm)
0.3 % brine equilibrated with AK93	69
AK93 equilibrated with 0.3 % brine	29.6
Air	19
3 % brine equilibrated with AK93	70
AK93 equilibrated with 3 % brine	31
Air	12
20 % brine equilibrated with AK93	71
AK93 equilibrated with 20 % brine	29.5
Air	16
4 % +0.5% $CaCl_2$ brine equilibrated with Moutray	62.4
Moutray equilibrated with brine	27.1
Air	8.3
4 % +2% $CaCl_2$ brine equilibrated with Moutray	64.7
Moutray equilibrated with brine	28
Air	9
3 % brine	68.5
Decane	25.4
Air	40.2

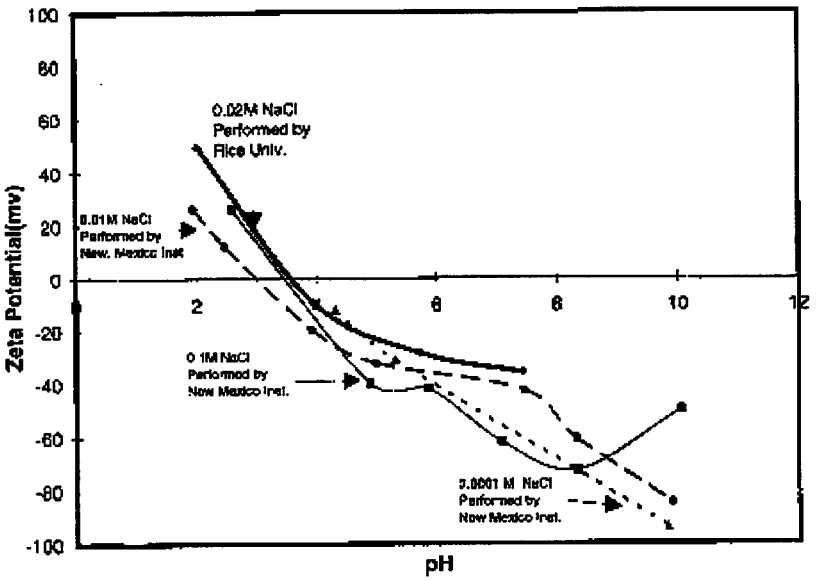

Fig. 6.1: Zeta potential of Prudhoe Bay at different pH.

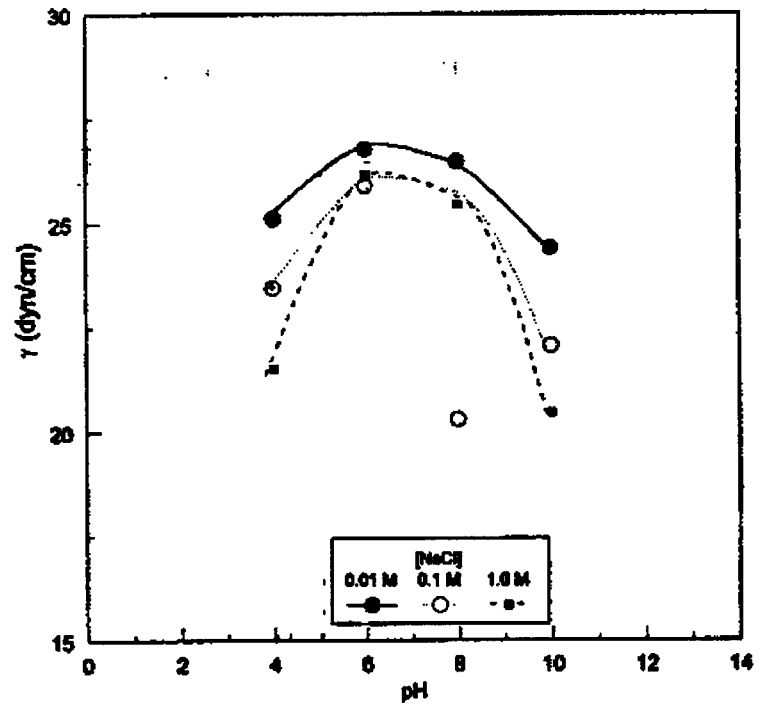

Fig. 6.2: IFT between Prudhoe Bay crude oil and brines of varying pH and ionic strength.

Fig 6.3: Beckman ultra-centrifuge with a video setup to allow early time readings

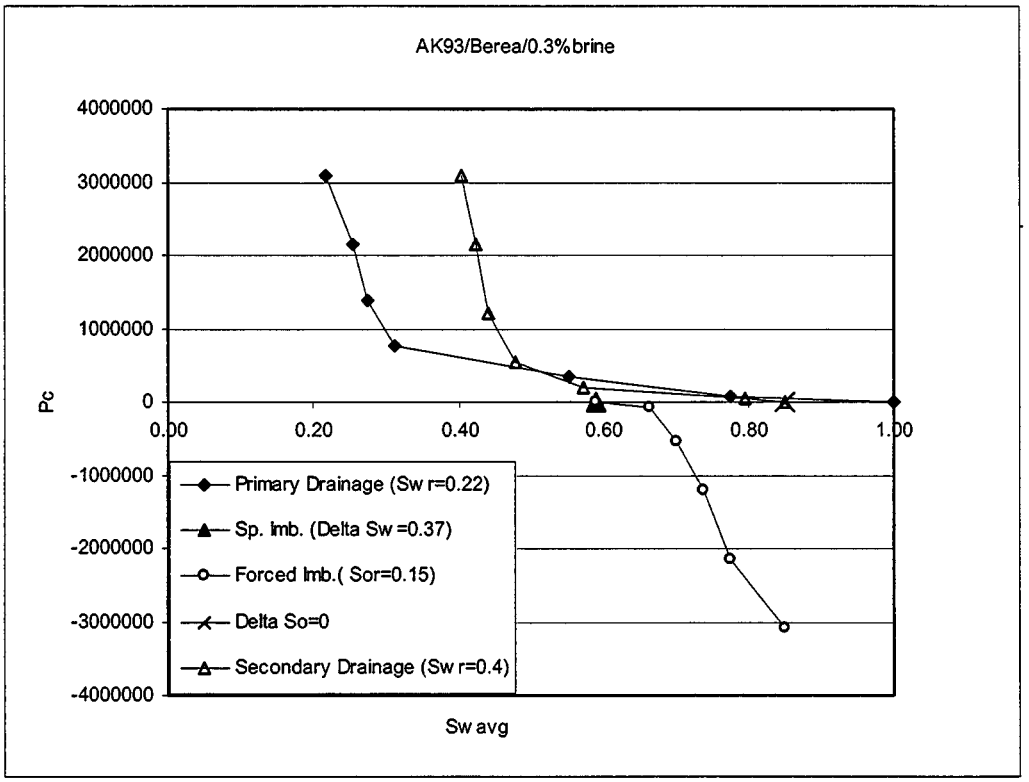

Fig. 6.4a: Capillary desaturation curves for 0.3% brine-AK93 –Berea system

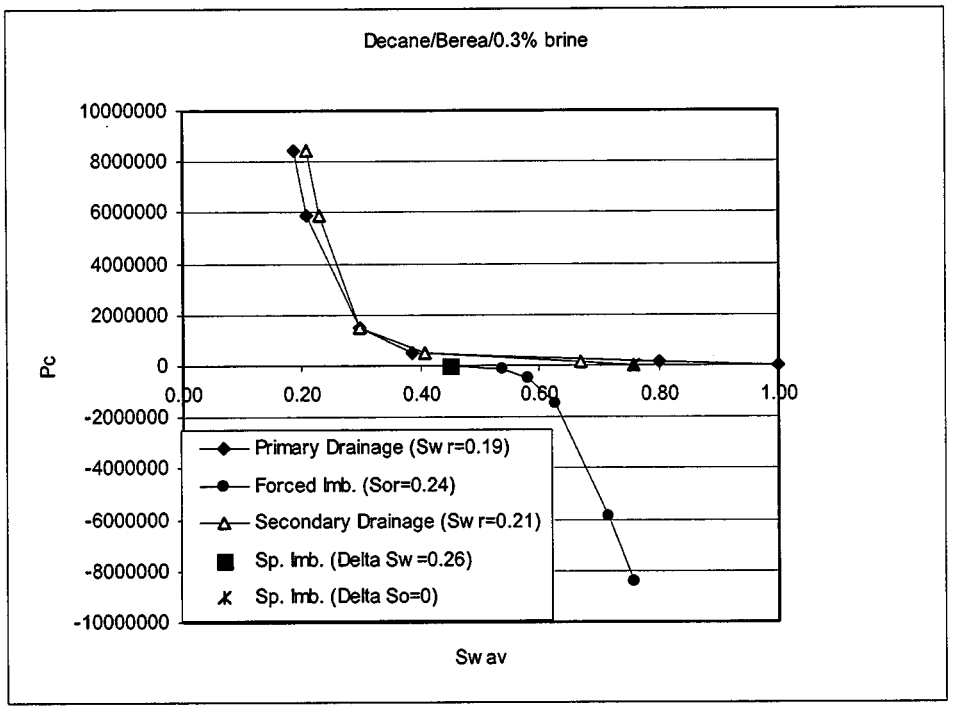

Fig. 6.4b: Capillary desaturation curves for 0.3% brine-decane –Berea system

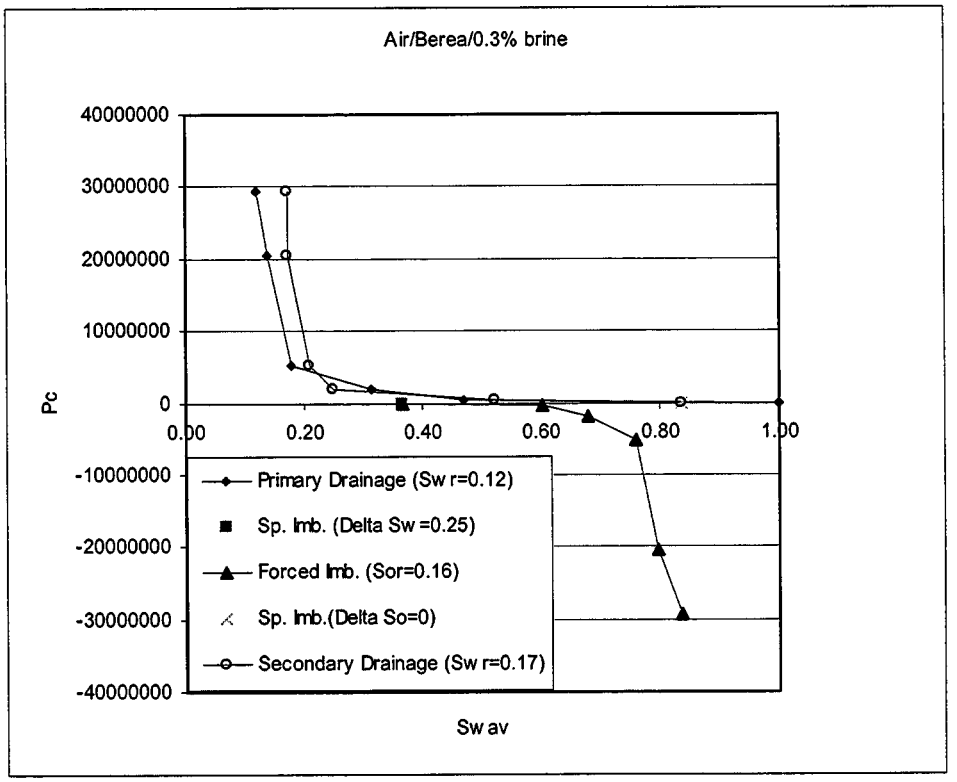

Fig. 6.4c: Capillary desaturation curves for 0.3% brine-air –Berea system

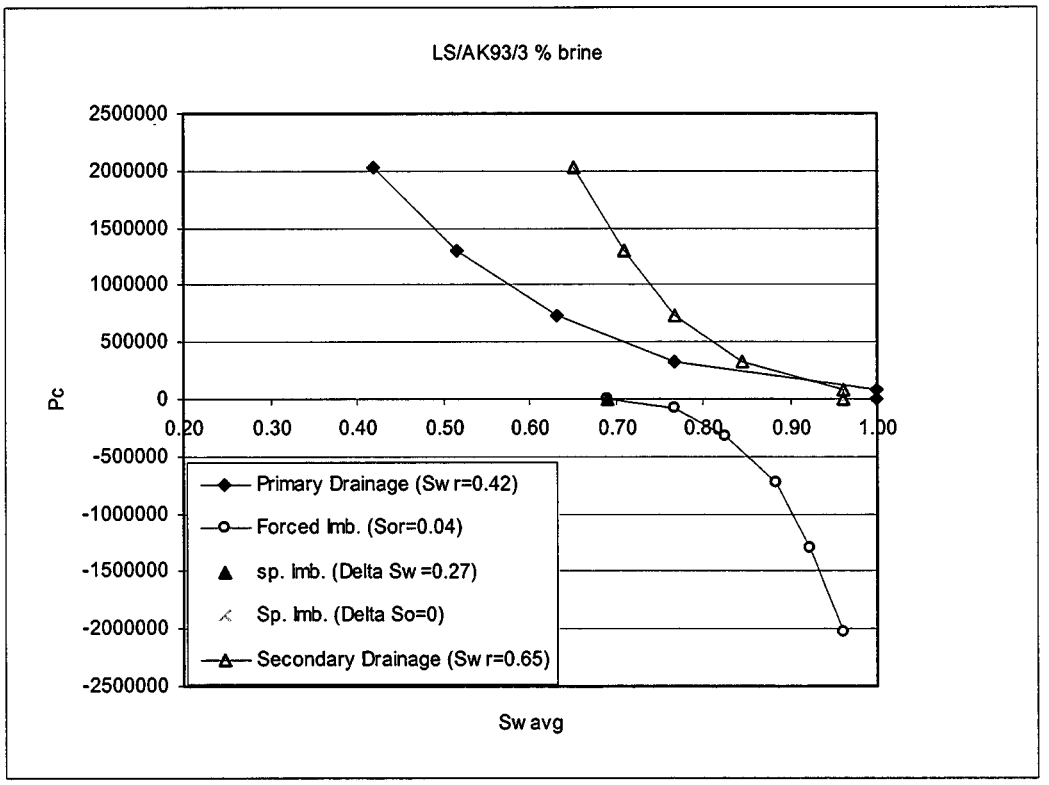

Fig. 6.5a: Capillary desaturation curves for 3% brine-AK 93 –limestone system

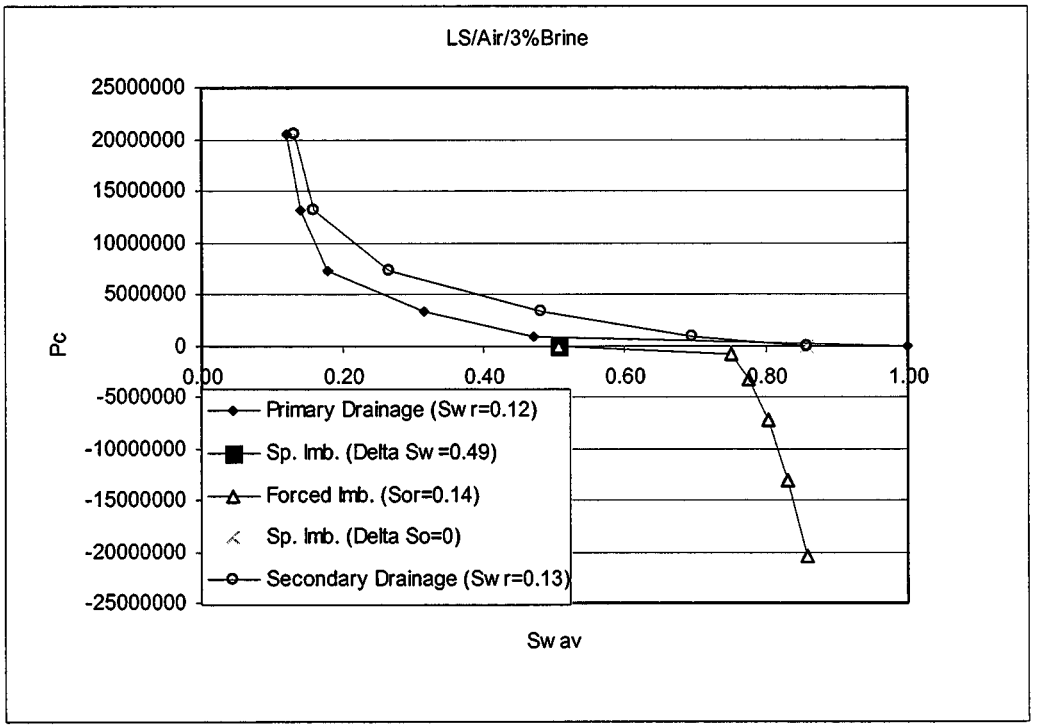

Fig. 6.5b: Capillary desaturation curves for 3% brine-air –limestone system.

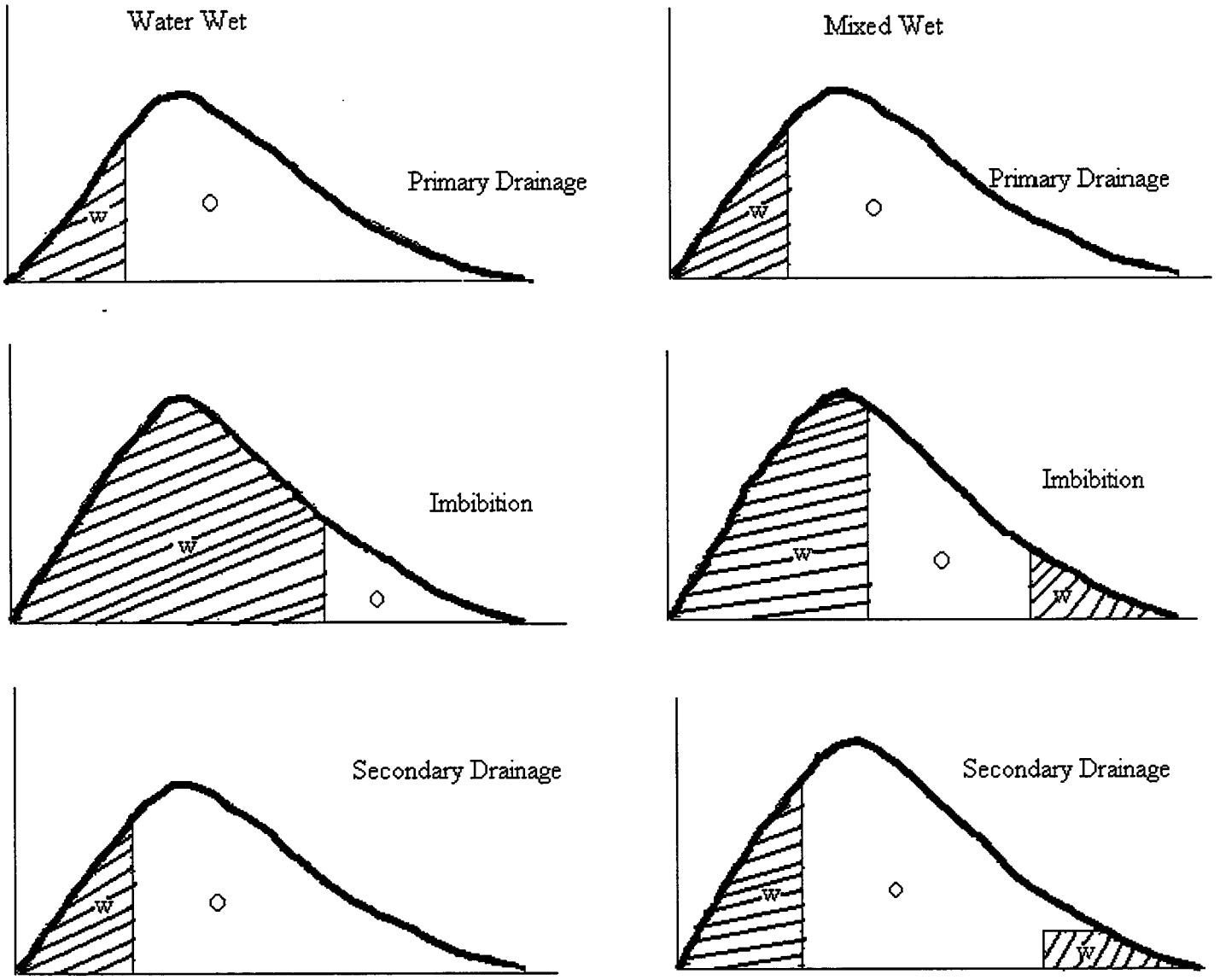

Fig. 6.6: Proposed mechanism of the change of wettability of the core from water-wet to mixed-wet during drainage and imbibition process.

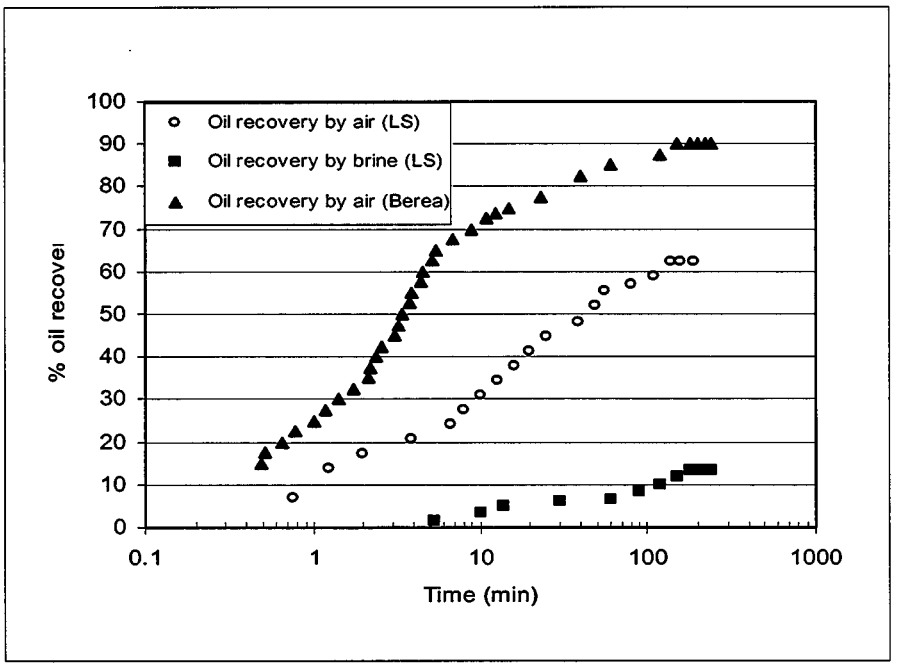

Fig. 6.7: Percentage of oil recovery (Prudhoe bay) during imbibiton by brine and air in SS and LS.

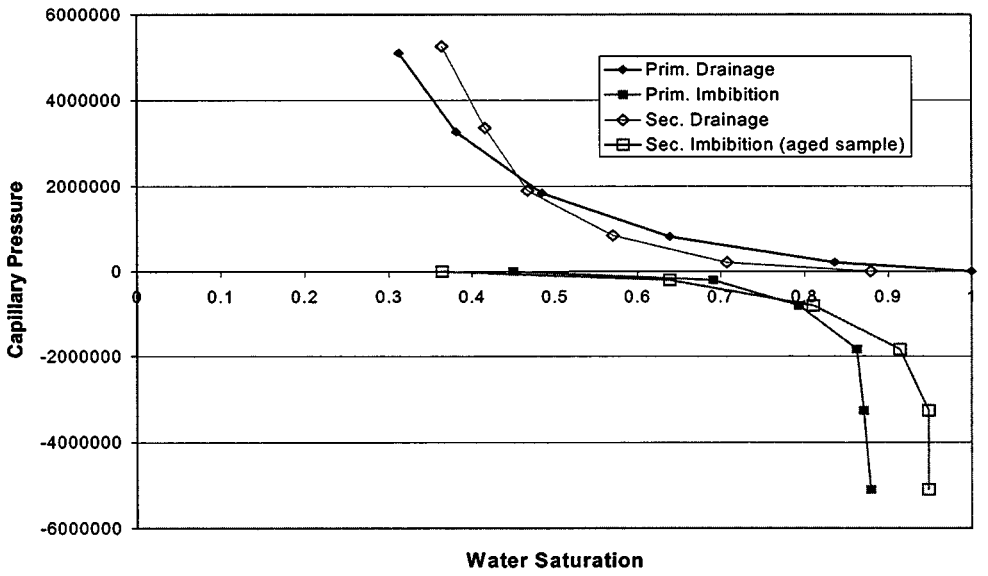

Fig 6.8: Capillary desaturation curves for an aged core in 4% NaCl + 0.5% CaCl2 brine-Moutray oil-LS system.

7. Determination of Liquid-Liquid Interfacial Area and Relative Permeability as a Function of Wetting Phase Saturation and Wettability

INTRODUCTION

The knowledge of the interfacial area is important to better understand and quantify many flow and transport processes in unsaturated/saturated porous media. Mass transfer processes such as adsorption, dissolution, and volatilization are all proportional to interfacial areas. Interfacial areas are also important for modeling colloidal and microbial transport. Air-water interfacial area is important for characterizing remediation process like soil-vapor extraction in vadose zone. Air-water interfaces serve as sorption sites for colloids and bacteria, subsequently retarding their transport process in the unsaturated media. Similarly knowledge of liquid-liquid interfacial area is important to estimate the contaminant flux between nonaqueous phase liquids (NAPL) and water for various remediation processes such as surfactant enhanced aquifer remediation (SEAR) and adsorption of bacteria. Hence knowledge of the interfacial areas would facilitate the quantification and numerical simulation of a variety of flow and transport processes; including remediation strategies for organic contamination.

The objective of this research was to develop a tracer technique to characterize the wettability of porous mediums over a wide range, by measuring specific liquid-liquid interfacial area. Interfacial tracers can be used to measure the specific oil-water interfacial area in a porous media. A standard assumption in modeling is that the flowing aqueous phase is in local chemical equilibrium with the oil/NAPL phase. Depending on the flow rate, the NAPL saturation and the ratio of surface area to volume of the NAPL phase, this assumption may not be valid. Moreover, the area of the liquid-liquid interface is likely to vary with NAPL saturation, and this effect is not accounted for in standard kinetics models. Because so little data is available for interfacial area, this paper presents a series of experiments with interfacial tracers (compounds that adsorb to the oil/water interface) in order to better define the possible range of interfacial areas over different saturations for varying type (water wet and oil wet) of porous medium.

BACKGROUND

Most of the fluid transport in porous media models employ a "lumped" mass transport parameter, which includes an interfacial area and mass transfer coefficient, as it is difficult to measure the interfacial area over which the adsorption, dissolution etc is occurring. This would not be a problem if the interfacial area were constant. However, applications of the novel experimental method of interfacial tracers show clearly that interfacial area varies with non-wetting phase saturation.

There are quite a few theoretical studies which have modeled air-water or liquid-liquid interfacial area in porous media as a function of pressure and saturation using specific pore geometry (Gvirtzman and Roberts, 1991; Reeves and Celia, 1996, Cary, 1994; Bradford and Leij, 1997). Some experimental measurements of air-water interfacial area in unsaturated porous media as a function of saturation have been carried out. Karkare and Fort (1996) used a hydrophobic surfactant (1-tetradecanol) to study its impact on water movement and then calculated air-water interfacial area as the number of molecules of surfactant required to initiate water movement multiplied by area of each surfactant molecule. Kim et al. (1997) developed a miscible displacement technique using interfacial tracers to measure the interfacial areas. The interfacial tracers technique can be used as a simple, nondestructive measurement method for obtaining the specific oil-water interfacial area in both laboratory and field settings (Saripalli et al., 1997 and Annable et al., 1997). Anionic surfactants are used as interfacial tracers at concentrations below the critical micelle concentration (CMC), to minimize solubilization and mobilization of the oil phase. These interfacial tracers accumulate at the oil-water or air-water interface by adsorption, however they do not partition into the oil or air phase.

Schaeffer et al. (2000) measured air-water interfacial area as a function of capillary pressure and water saturation. They measured interfacial areas greater than that observed by Kim and Rao (1997) and attributed this to inclusion of thin films in their measurements. Faisal Anwar et al. (2000) have developed a new method to measure air-water interfacial area using the surfactant adsorption concept. The experimental studies along with modeling results show air-water interfacial area increases with decreasing water saturation during drainage cycle. The imbibition cycle area differs from the corresponding drainage data.

Schaeffer et al. (2000) observed no relation between interfacial area and increasing water saturation (imbibition cycle).

However, there are no studies present which measure the specific liquid-liquid interfacial area in a porous media as a function of water saturation. Most of the work by Sarapalli et al. (1997) involved measuring the liquid-liquid interfacial area at residual non-wetting phase concentration for water wet and oil wet sands. The objective of this study is to measure liquid-liquid interfacial area as a function of saturation over a range of wettability states (water wet and oil wet porous medium).

Initial experimental evidence strongly indicates that the specific oil-water interfacial area exhibits changes as a function of the wetting state of the porous medium. Saripalli et al. (1997) conducted sand packed column experiments with pentaflurobenzioc acid as a conservative tracer and sodium dodecyl benzenesulfonate (SDBS) and sodium dioctyl sulfosuccinate (Aerosol OT-100) as interfacial tracers. Results from their column experiments using interfacial tracers demonstrate that the specific oil-water interfacial area (per unit pore volume) varied from 86 cm^2/cm^3 to 272 cm^2/cm^3 depending upon which phase was initially present in the column. When water was initially present in the column and was displaced by decane, which was subsequently reduced to a residual saturation, the specific interfacial area between the water and decane at a residual decane saturation was 86 cm^2/cm^3. The specific interfacial area was much larger when decane was initially present in the column and then reduced to a residual saturation by water. In the first case, decane in the water-saturated column can not coat the water-wet solid surfaces and is thus trapped primarily within the larger pores, producing a small specific interfacial area.

All the studies discussed above, assume that there was no impact of sorption onto the porous medium. The background sorption of interfacial tracers onto the solid matrix can be measured by conducting tracer experiments in the water-saturated sand packed column. Previous studies have revealed that the SDBS interfacial tracer does not sorb significantly onto the porous medium (Saripalli et al., 1997). However, column and field studies conducted and reported by Field and Istok (1998) show that there is chromatographic separation of the tracer SDBS along the column due to preferential sorption of the linear alkyl benzenesulphonate (LAS) components. The results of the study conducted by Kruger et al. (1998) shows that the retardation factor increased with increasing alkyl chain length

and external substitution. Moreover, their results show that the ten and eleven carbon chain length LAS homologues were the least hydrophobic and they weakly adsorbed onto the porous medium. These studies show that use of SDBS as an interfacial tracer can impact the retardation factor and overestimate the interfacial area. Thus, the choice of a surfactant as an interfacial tracer is very important.

THEORY

Aqueous transport of a tracer through a homogeneous porous medium can be modeled by using the one-dimensional advective-dispersion equation:

$$R\frac{\partial C_w}{\partial t} = -v_x\frac{\partial C_w}{\partial x} + D_w\frac{\partial^2 C_w}{\partial x^2} \qquad [7.1]$$

Where R is the retardation factor; C_w: aqueous phase concentration, mol/cm^3; v_x: pore water velocity; cm/min; x: distance, cm, t: time, min; D_w: hydrodynamic dispersion coefficient, cm^2/min.

The retention factor, R, contains all the terms that account for retention of a tracer in the porous medium, which includes sorption onto the porous medium and adsorption at the wetting-non-wetting interface:

$$R = 1 + \frac{\rho K_d}{S_w} + \frac{K_o}{S_w} \qquad [7.2]$$

ρ: bulk density of solid, g/cm^3; K_d: sorption coefficient onto the solid matrix, cm^3/g; S_w: wetting phase or water saturation; K_o: adsorption coefficient at the wetting-nonwetting interface.

The phase distribution coefficients can be estimated from independent experiments. If the sorbed concentration of the tracer (C^s_{ads}, mol/g) onto the solid porous medium is a simple linear function of the equilibrium aqueous concentration, C_w, then,

$$C^s_{ads} = K_d C_w \qquad [7.3]$$

The sorption coefficient can be estimated be measuring the sorbed concentration of the surfactant onto the porous medium in a series of batch experiments. This can also be estimated from a tracer experiment conducted in a water-saturated column in absence of non-wetting phase. The retardation of the interfacial tracer with respect to the conservative tracer

gives the sorbed concentration of the interfacial tracer onto the solid medium. However, if the interfacial tracer does not sorb onto the porous medium, then the retardation factor is given as,

$$R = 1 + \frac{K_o}{S_w} \qquad [7.4]$$

Similarly, Gibbs adsorption equation can be used to interpret the adsorption of the tracer at the oil-water interface. The adsorbed concentration of the tracer (C^i_{ads}) at the oil-water interface is given as,

$$C^i_{ads} = \Gamma a_i = K_o C_w \qquad [7.5]$$

where a_i is the oil-water interfacial area, cm^2/cm^3 and Γ, surface excess of the tracer is given as,

$$\Gamma = -\frac{1}{2RT}\left(\frac{\partial \gamma}{\partial C_w}\right)_T C_w \qquad [7.6]$$

Γ: surface excess of the tracer, mol/cm^2; R: ideal gas constant, erg mol^{-1} K^{-1}; T: absolute temperature, K; γ: interfacial tension, dyne/cm.

Surface excess of the tracer can be determined using interfacial tension data. Since γ is a nonlinear function of C_w, the interfacial adsorption isotherm is nonlinear too. However, it can be used to estimate K_o using equations 7.5 and 7.6:

$$K_o = \frac{\Gamma a_i}{C_w} = -\frac{a_i}{2RT}\left(\frac{d\gamma}{dC_w}\right) = -\frac{a_i \beta}{2RTC_w} \qquad [7.7]$$

where β is obtained by fitting the following equation: $\gamma = [\alpha - \beta \ln(C_w)]$.

For a step-input tracer experiment the retardation factor is calculated by measuring the area above the breakthrough curve and can be calculated using equation 8:

$$R_{ift} = \frac{\mu_{ift}}{\mu_{con}} \qquad [7.8]$$

where μ is given as

$$\mu = \int_0^\infty (1 - C^*)dt \qquad [7.9]$$

here, $C^x(t) = C(t)/C_w$, is the normalized concentration of the tracer monitored at the column outlet; C_w is the influent tracer concentration.

The retardation factor obtained from the analysis of the effluent profile of the tracers can be used to obtain the oil-water interfacial area using equations 7.2 and 7.8.

MATERIALS AND METHODS

Experiments were conducted to study the spatial distribution of fluid saturations and specific interfacial areas of two immiscible fluids under static and steady flow conditions. Inert and interfacial tracers were used to measure a_i, area of the interface between the phases.

Materials

Flow experiments were conducted in glass columns packed with cleaned glass beads (Potter Industries, Brownwood, TX). The glass beads were cleaned using 0.1 M HCL and 15% H_2O_2 in order to remove surface impurities like metal ions and to oxidize the organic matter. The glass beads were then thoroughly washed with water to remove the residual acid and peroxide, and then oven-dried before storing them in a clean beaker for use in column experiments. The glass beads were made oil wet using silane.

Water was used as the wetting/aqueous phase and decane was the organic nonwetting phase. Experiments were conducted with decane loaded in different ways (e.g. water loaded first vs decane loaded first) in columns packed with water wet or oil wet glass beads. Potassium iodide, KI, and pure 3-phenyl decyl benzene sulfonate (C_{10} 3-ϕ LAS), an anionic surfactant were used as conservative and interfacial tracers, respectively. C_{10} 3-ϕ LAS is a 10 carbon, linear alkyl benzenesulphonate, with the benzene ring at the third carbon position. All the chemicals used in this research were obtained from Aldrich chemical company, Milwaukee, WI, except the interfacial tracer. The surfactant was purified in the chemistry department at the University of Texas at Austin. T-stilbene was the conservative organic soluble tracer. Based on the results of Saripalli et al. (1997) and Kruger et al. (1998), C_{10} 3-ϕ LAS used in this study should have very weak sorption on to the porous medium and also no chromatographic separation.

Methods

Aqueous solutions were prepared at different surfactant concentrations and interfacial tension was measured between the aqueous surfactant solutions and decane using a ring tensiometer.

Figure 7.1 shows the setup for column experiments. The column was a chromatography (Kontes, Vineland, NJ) glass column (diameter: 2.5 cm and length: 30 cm), fitted with PTFE shielded O-rings, metal screens, and a variable length teflon fitting at one end, which can be used to control the packed length of the column. The other end fitting was modified to facilitate simultaneous flow of oil and water. A 100 mesh metal screen was present on each end of the column to prevent migration of fines and to distribute fluids evenly in the column.

The glass column was dry packed on a vibrating table. The column was packed in increments, so that the glass beads packed densely. A consistent porosity was achieved by this method. The column was then evacuated for 1 hour. It was then flooded with CO_2 gas and again evacuated for ½ hour and then saturated with deairated and de-ionized water. The column was then flushed with 2-3 pore volumes of deairated water before the tracer experiments were conducted. The gross weight of the column without sand and the column with sand was measured. The dry weight of the sand packed in the column was obtained from the difference in weight, which was used to obtain the overall porosity and pore volume of the column.

The permeability of the column to water was measured using pressure transducers (Cole Parmer, Vernon Hills, IL) connected to the inlet and outlet lines of the column. The electrical signal from the pressure transducer was converted into pressure and recorded on a chart recorder. Measurements were done at different speeds (1-4ml/min) and the average permeability was computed.

The measurements of interfacial area are extracted from the retardation of a step-change in interfacial tracer concentration relative to a step-change in inert/conservative tracer concentration. The retardation was determined from effluent concentration histories (concentration of tracer exiting the column vs. time). The effluent concentrations are measured directly in a flow-through sample cell plumbed into the experimental apparatus. This provides the requisite resolution for determining retardation of the concentration front

and eliminates many of the concerns that would arise if discrete samples were collected and then analyzed in batch mode. To eliminate the possibility of overlapping absorption peaks, the tracers are injected in separate slugs.

The column was flushed with a step input of KI at a C_w value of 25 mg/L, which was followed by water when KI was observed in the effluent. Once, there was no more KI observed in the effluent, the column was flushed with another 2-3 pore volumes of water and the process was repeated with a step input of C_{10} 3-ϕ LAS at a C_w value of 50 mg/L. The injected concentration is far below the CMC of the surfactant (600 ppm). Because of the low injection concentration of the tracer, we do not anticipate any mobilization or solubilization of the oil, which would have changed the interfacial area as the tracer was injected in the column. Effluent profile was analyzed using an online UV detector (Ocean Optics, Model: CHEM2000-UV-VIS) for a continuous detection of KI (wavelength: 221 nm) and LAS (wavelength: 217 nm). Each data point (concentration in effluent line at a given time) was the average of 25 scans of the contents of the in-line sample cuvette (Hellma Scientific, 18 µl volume), taken over a 0.04 minute interval. The scanning and averaging are carried out automatically by the spectrophotometer system that includes a proprietary data acquisition card and software. Data are logged directly to a PC.

A calibration curve was prepared for each tracer that relates measured absorbance to known tracer concentration. The response was almost perfectly linear. Measurements in the range of interest, i.e. greater than 1% of the injected concentration, show high accuracy. The calibration curve was used to obtain the effluent concentration profile.

The initial tracer tests were done to calculate the background sorption of interfacial tracer onto the glass beads. After that, decane being lighter than water was introduced into the column from the top. A connate water saturation of about 30% was obtained. Subsequently, the column was flushed with 4-5 pore volumes of water from the bottom at increasing flow rates (1ml/min-4ml/min) to reduce the column to a residual decane saturation. After establishing residual decane saturation in the column, the tracer experiments are conducted following the procedure described above. The retardation was obtained from the effluent concentration profile. The flow-rate through the column was maintained at 1 ml/min.

The decane saturation in the column was increased by flowing decane through the column, while reducing the water flow rate, keeping the total flow rate through the column constant at 1ml/min. At each fractional flowrate, water and decane were simultaneously injected into the column for 35-40 pore volumes to achieve steady state saturations in the column. The permeability to liquid phases was measured at each stage, followed by the tracer experiments. Water saturation at each fractional flowrate was obtained from the conservative tracer profile, while the retardation of the interfacial tracer in comparison to the conservative tracer was used to obtain the interfacial area. The residual water saturation was obtained by using T-stilbene as the conservative tracer in oil, as at this point water is present as discontinuous phase in the column. The fractional flow rate was changed in the following sequence: 1 ml/min water; 0.75 ml/min water to 0.25 ml/min decane; 0.50 ml/min water to 0.50 ml/min decane; 0.25 ml/min water to 0.75 ml/min decane; 1 ml/min decane.

RESULTS AND DISCUSSION

Interfacial tension measurements

Interfacial tension was measured for different concentrations of C_{10} 3-ϕ LAS surfactant with decane. Figure 7.2 shows the reduction in interfacial tension with increase in surfactant concentration. The slope (β) is required to calculate K_o as shown in equation 7.7. It was obtained by fitting the interfacial tension data (Figure 7.3). K_o has a value of $8.16X10^{-4}$ cm for a C_w of 50mg/L (the injection concentration of the C_{10} 3-ϕ LAS tracer in the column experiments).

Interfacial area measurements

A typical effluent profile as a function of pore volume injected is shown in Figure 7.4. As the figure shows that there was a small retardation of C_{10} 3-ϕ LAS tracer as compared to the conservative KI tracer. Hence sorption of LAS onto the porous media can not be neglected in calculating retardation factor and interfacial area.

Repeat injections of tracers (KI and C_{10} 3-ϕ LAS) were done in water saturated column to establish the accuracy and repeatability of the effluent profile. Injected concentrations of the tracers are 25 to 50 mg/l. Standard deviation of replicate analysis was

of the order 10^{-3} mg/l, so that the MDL was of the order 10^{-4} mg/l. The precision of concentration measurements obtained from the UV spectrophotometer was better than 1%. Two sets of replicate analyses on each of the two tracers (KI and LAS) were conducted of the injection concentration in batch mode. For each set 80 to 100 measurements were carried out, each measurement being the average of 25 scans conducted in a 0.04 minute interval (these are the acquisition conditions during the experiments). The relative standard deviations obtained are summarized below.

Tracer	RSD, first set	RSD, second set
KI	0.53%	0.27%
LAS	0.33%	0.44%

The results of the replicate effluent profiles and batch studies show great reproducibility of the data and the accuracy of the detecting equipment.

Repeat injections of C_{10} 3-ϕ LAS tracer were done in column at residual decane saturation to observe the impact of flow stoppage and flowrate. The results indicate that the changes in flowrate (reduction from 1ml/min to 0.25 ml/min) and flow stoppage (15 hrs) had no impact on the effluent profile. Thus, mass transfer limitations are not governing the sorption of surfactant.

Figure 7.5 shows the effluent profiles of LAS and KI for two different conditions highlighting the impact of residual decane on the retardation of LAS in a glass column. As the figure shows, the presence of residual decane saturation results in the KI tracer breakthrough before 1 pore volume (earlier than in a water saturated column). The C_{10} 3-ϕ LAS profile was delayed from the KI profile, due to the sorption of surfactant onto the porous medium and also at the water-decane interface. Equation 7.2, which includes sorption of tracer onto the porous media, was used to calculate the interfacial area between water and decane.

Table 7.1 gives the experimental conditions of the four experiments whose results are presented in this paper. Experiments ww1 and ww2 were conducted using water wet glass beads, while in experiments ow3 and ow4, oil wet beads were used. The glass beads were made oil wet using the silination method. In the ww1 experiment the interfacial area was measured during the primary drainage, where decane displaced water from the column. In the ww2, experiment the column was reduced to residual decane saturation and specific

interfacial area measured during the secondary drainage, whereby water flowrate was decreased and decane flowrate increased, till residual water saturation was achieved. The experiments ow3 and ow4 are similar to the ww1 and ww2 experiments, however oil wet beads were used to pack the glass column. In experiment ow3, area was measured during primary drainage, where water displaced decane. Experiment ow4 is similar to ww2, however water was first loaded into the column, and the interfacial area was measured during the secondary imbibition.

Figure 7.6 shows the changes in interfacial area as a function of water saturation in a glass column packed with 400 μm diameter water wet glass beads. The figure shows the change in interfacial area for two cases: primary drainage (exp.: ww1) and secondary drainage (exp.: ww2). Changing the water/decane fractional flow rate through the column changed the water saturation in the column. As the figure shows, decrease in water saturation leads to increase in interfacial area. This result is consistent with changes in air-water interfacial area observed in other studies (Kim et. al. 1997, Schaefer et. al. 2000, and Faisal et. al. 2000).

The figure shows that decreasing the water saturation from 82% to 61% increases the interfacial area from 50 cm^2/cm^3 to 190 cm^2/cm^3. At residual saturation, decane is present as a discontinuous phase in larger pores and hence it presents a smaller water-decane interfacial area. However, as the decane saturation increases in the column, it starts occupying smaller pores, which leads to a larger water-decane interfacial area over a specific pore volume. If the glass beads are assumed to be perfect spherical, then the surface area of the particles is 98.7 cm^2/cm^3 total volume (obtained by dividing the surface area of a glass bead by its volume, and then multiplying by 1-porosity). As the water saturation decreases, the film area increases dramatically in comparison to the interfacial area. The total interfacial area calculated and measured here includes the contribution of the water films present over the glass beads.

The changes in interfacial area as a function of water saturation in a glass column packed with oil wet glass beads for primary and secondary drainage are shown in Figure 7.7. The interfacial area curve measured during primary drainage (exp.: ow3) was different from that measured during secondary drainage (exp.: ow4). The area increased from 50 cm^2/cm^3 to 95 cm^2/cm^3 with increase in decane (wetting phase) saturation from10% to 25%.

However, it reaches a maximum and reduces at the residual water saturation (70%). This results shows that decane film are not sustained over the glass beads as the decane saturation decreases, as that would have lead to an increase in total interfacial area, instead of a decrease in area, as observed. This result is different from the results obtained for water wet glass beads. In the water wet case the area increases with the decrease in water saturation, due to the presence of wetting film on the glass beads. The change in total interfacial area measured in experiment ow4 during secondary drainage showed trends similar to experiments ww1 and ww2. The area increased 50 cm^2/cm^3 to 190 cm^2/cm^3 for reduction in water saturation from 72% to 21%. The results indicate that it was easier to establish and sustain water films over glass beads as compared to oil films. There was breakdown in oil films, which reduced the film area in experiment ow3 as compared to presence of water films in the other three experiments.

Figure 7.8 compares changes in interfacial area and residual decane saturation as a function of grain size. It shows that at residual decane saturation, increasing the grain size of glass beads leads to a decrease in the specific interfacial area. The water-decane interfacial area for 3-mm glass beads is 22 cm^2/cm^3 as compared to 50 cm^2/cm^3 for 0.4-mm glass beads. This is very much expected as the specific solid surface area increases with decrease in grain size, which also leads to an increase in the specific liquid-liquid interfacial area. Film area is at a minimum at residual decane saturation. Faisal et al. (2000) observed similar results in their experiments with glass beads ranging from 0.25mm to 0.75mm diameter, while measuring air-water interfacial area. The residual decane saturation also decreases with increase in grain size.

The relative permeability of water and decane as a function of water saturation in columns packed with water-wet and oil-wet glass beads are shown in Figures 7.9 and 7.10, respectively. Decreasing water saturation decreases permeability of the column to water, while it increases the decane permeability. The relative permeability curves shift left for oil wet glass beads as compared to water wet beads, which was expected due to the change in wettability of the porous medium. The presence of films and changes in interfacial area impacts the relative permeability. The interfacial area measurements will be used to validate the models for prediction of relative permeabilities (Alpak and lake, 1999) and compared to the experimental values.

CONCLUSION

A new method has been developed for the measurement of liquid-liquid interfacial area as a function of saturation. The results show that interfacial area increases with decrease in water saturation and at residual water saturation, the areas are close to 180 cm^2/cm^3. This high interfacial area was due to the presence of water films on the glass beads. However, the results of the interfacial area measured during primary drainage of decane in oil wet beads are different. The area increases with a decrease in decane saturation and reaches a maximum and decreases again at the residual decane saturation. These results indicate that oil films are either not sustainable at high water saturation or if they are present the tracer does not account for them.

A principal objective achieved was the evaluation of the possible range of interfacial areas that could be expected in typical field situations. In this respect the experiments provide a considerable benefit even if they merely indicated the order of magnitude of the areas, since so little was known about their variation in the field. The application of these data will serve as a baseline for future work on more heterogeneous porous media, notably soils/rocks with a wider distribution of grain sizes than those studied in this work. These data will be compared with pore-scale model predictions. The resulting data will be used to characterize the constitutive relationships between a_i, S_w and relative permeability and to verify and advance the mathematical models.

REFERENCES

1. Annable, M. D., Jawitz, J. W., Rao, P. S. C., Rai, D. P., Kim, H., and Wood, A. L. (1997) Field evaluation of interfacial and partitioning tracers for characterization of effective NAPL-water contact areas, Ground Water, 36(3), 495-502.

2. Alpak, F. O. and Lake, L. W. (1999) Validation of a modified carmen-kozeny equation to model two-phase relative permeabilities, presented at SPE conference, Houston, Texas.

3. Faisal Anwar, A. H. M., Bettahar, M., and Matsubayashi, U. (2000) A method for determining air-water interfacial area in variably saturated porous media, Journal of Contaminant Hydrology 43, 129-146.

4. Field, J. A., and Istok, J. D. (1998) Comment on estimation of nonaqueous phase liquid-water interfacial areas in porous media following mobilization by chemical flooding, Environmental Science and Technology, 32(23), 3836-3837.

5. Karkare, M. V., and Fort, T. (1996) Determination of the air-water interfacial area in wet unsaturated porous media, Langmuir, 12, 2041-2044.

6. Kruger, C. J., Barber, L. B., Metge, D. W. and Field, J. A. (1998) Fate and transport of linear alkylbenzenesulfonate in a sewage-contaminated aquifer: a comparison of natural-gradient pulsed tracer tests, Environmental Science and Technology, 32(8), 1134-1142.

7. Kim, H., and Rao, P. S. C. (1997) Determination of effective air-water interfacial area in partially saturated porous media using surfactant adsorption, Water Resources Research, 33(12), 2705-2711.

8. Saripalli, K. P., Kim, H., Rao, P. S. C., and Annable, M. D. (1997) Measurement of specific fluid-fluid interfacial areas of immiscible fluids in porous media, Environmental Science and Technology, 31(3), 932-935.

9. Schaefer, C. E., Dicarlo, D. A., Roberts, P. V., and Blunt, M. J. (1999) Determination of air-water interfacial area for drainage and imbibition in unsaturated porous media, American Society of Mechanical Engineers, Heat Transfer Division, (Publication) HTD Heat Transfer Division - 1999 ((The ASME International Mechanical Engineering

Congress and Exposition) Nov 14-Nov 19 1999 v364-2 1999 Nashville, TN, USA, Sponsored by: ASME, ASME Fairfield NJ USA p 93-97.

Experiment name	Type of porous media	Phase first loaded	Measurement of interfacial area
ww1	Water wet	water	Prim. drainage
ww2	Water wet	water	Sec. drainage
ow3	Oil wet	oil	Prim. drainage
ow4	Oil wet	water	Sec. imbibition

Table 7.1: Conditions of column experiments

Experiment name	Porosity	Saturated permeability, 10^{-5}, cm^2	Pore volume	Swr	Sor
ww1	0.35	4.29	39.5	25%	-
ww2	0.346	4.95	41	60%	18%
ow3	0.367	5.22	40.5	-	30%
ow4	0.36	3.34	40.6	22%	28%

Table 7.2: Results from column experiments

Setup for wettability tracer experiments

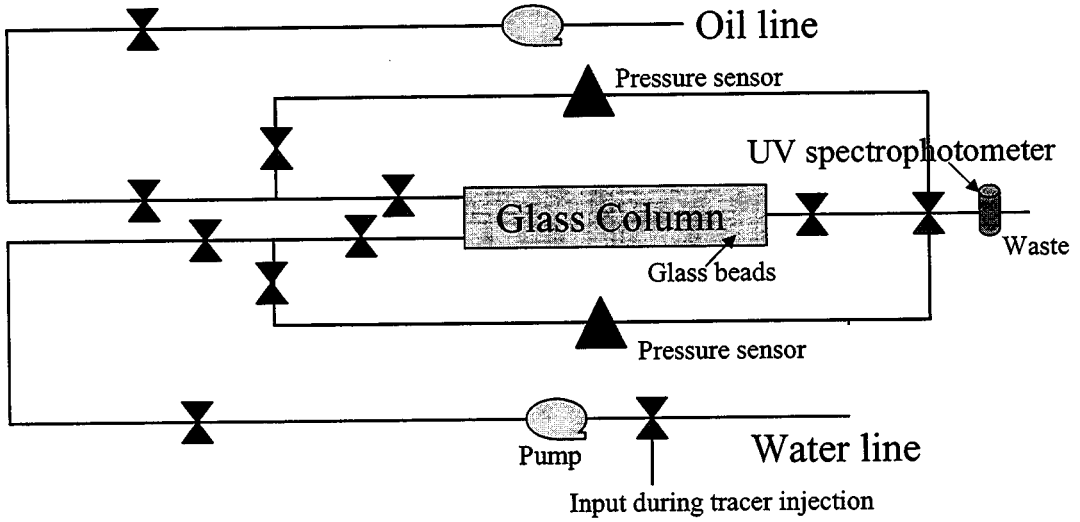

Figure 7.1 Experimental setup for column experiments

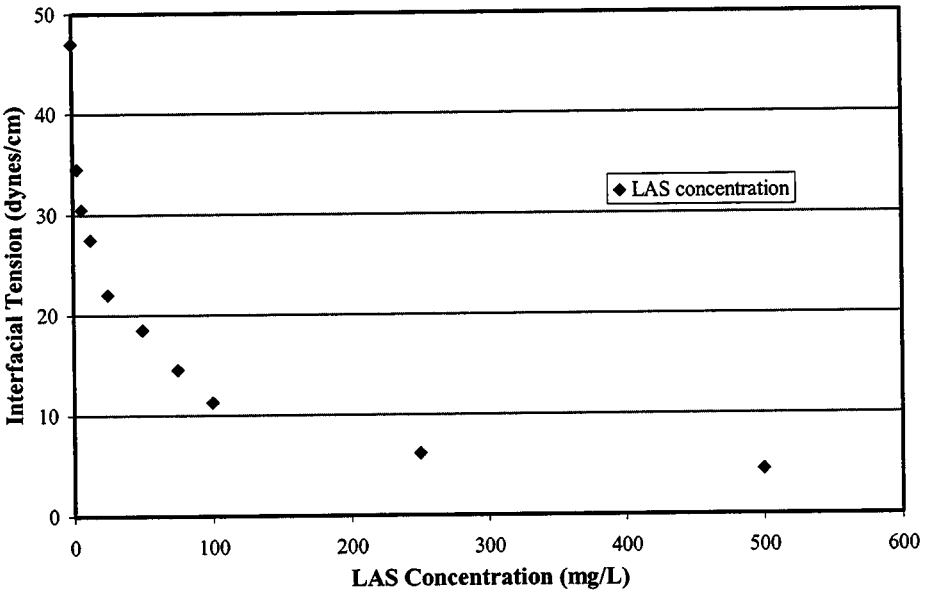

Figure 7.2 Interfacial tension of decane-LAS system as a function of LAS concentration.

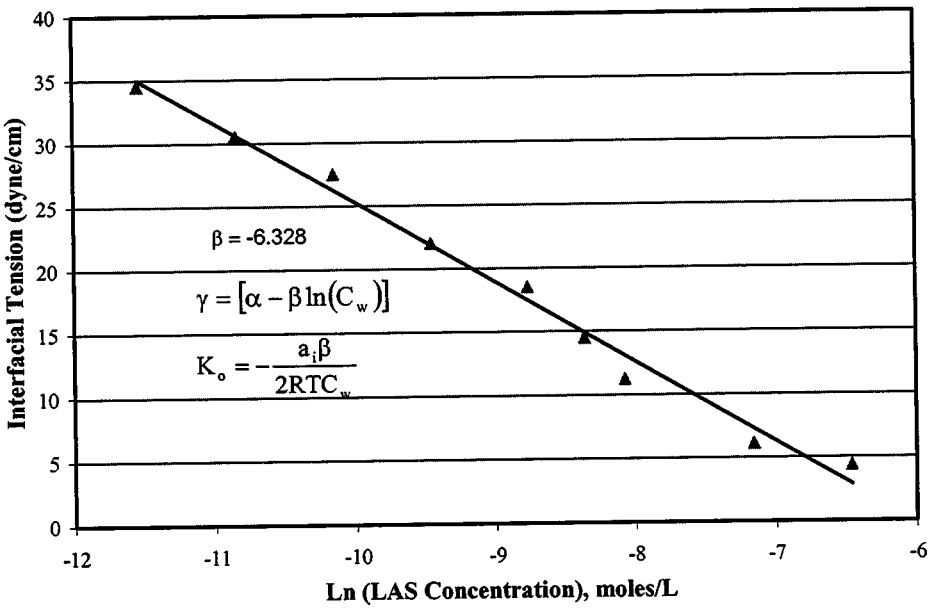

Figure 7.3 Interfacial tension plotted against Ln Concentration to obtain the slope for calculating the adsorption coefficient.

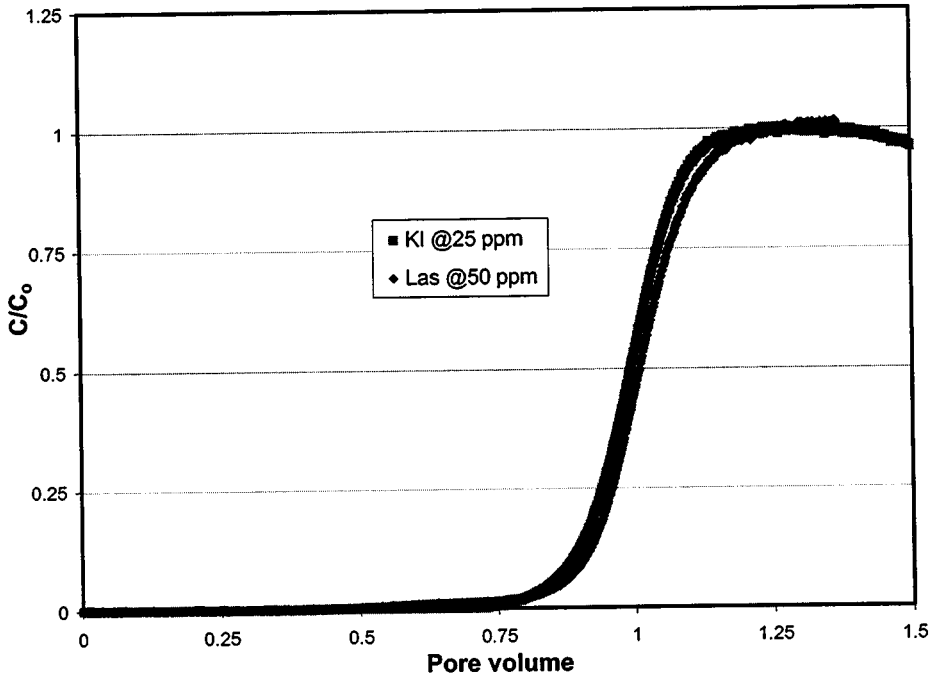

Figure 7.4 Comparison of effluent profile of LAS surfactant and KI in column.

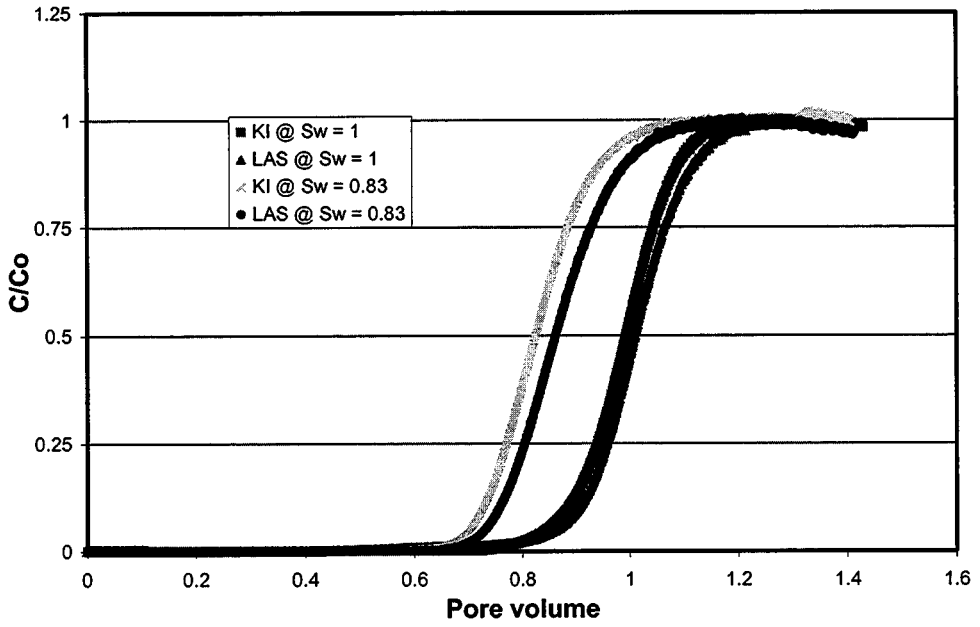

Figure 7.5 Comparison of effluent profile of LAS surfactant and KI showing the impact of residual decane in a column packed with water-wet glass beads.

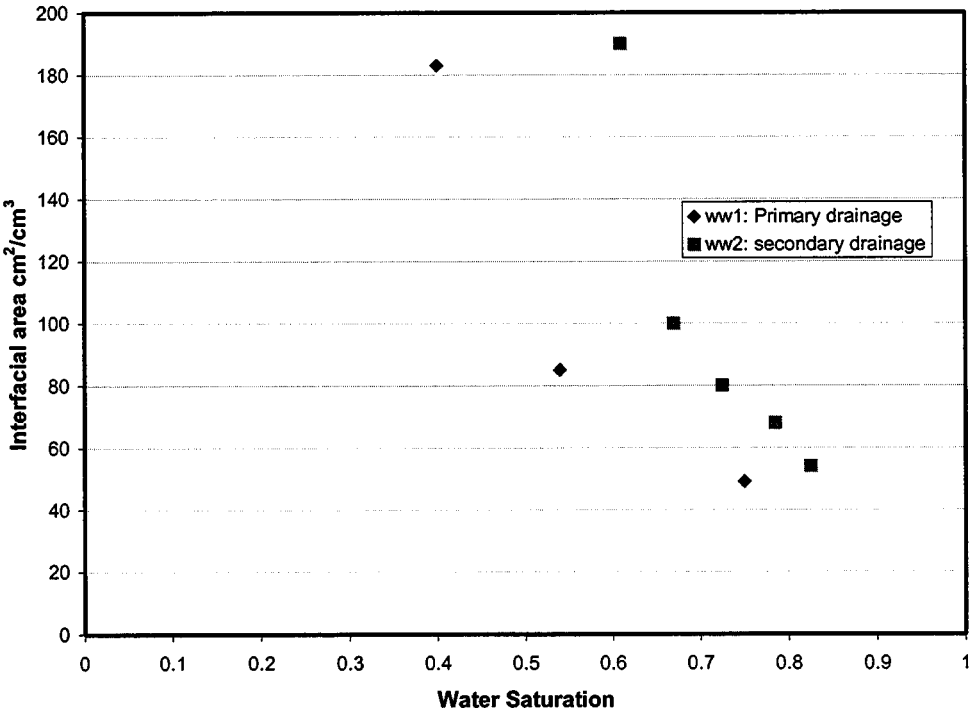

Figure 7.6 Change in interfacial area between water and decane as a function of saturation in a column packed with water wet glass beads.

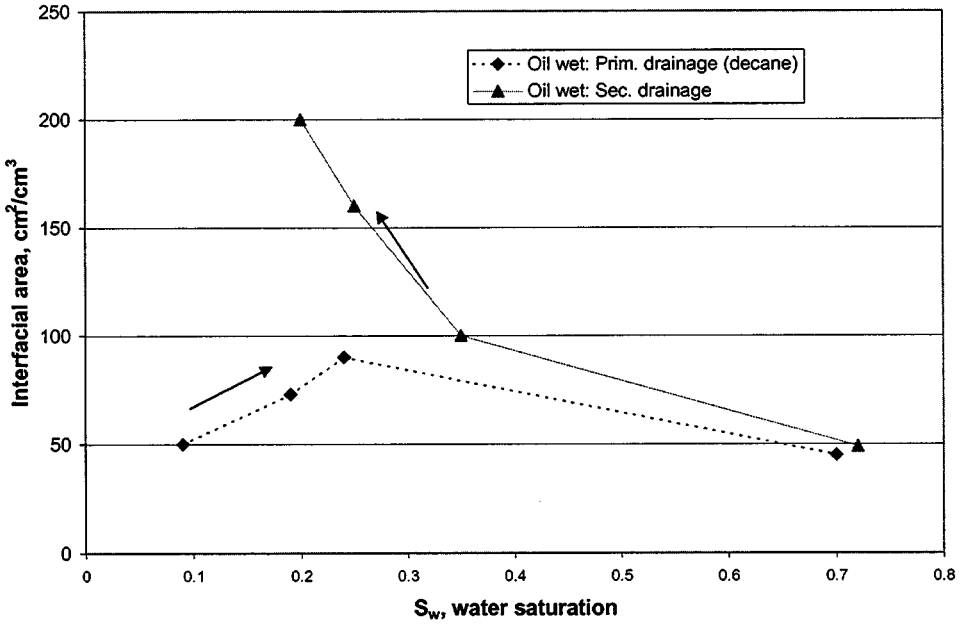

Figure 7.7 Change in interfacial area between water and decane as a function of saturation in a column packed with 0.4 μm oil wet glass beads.

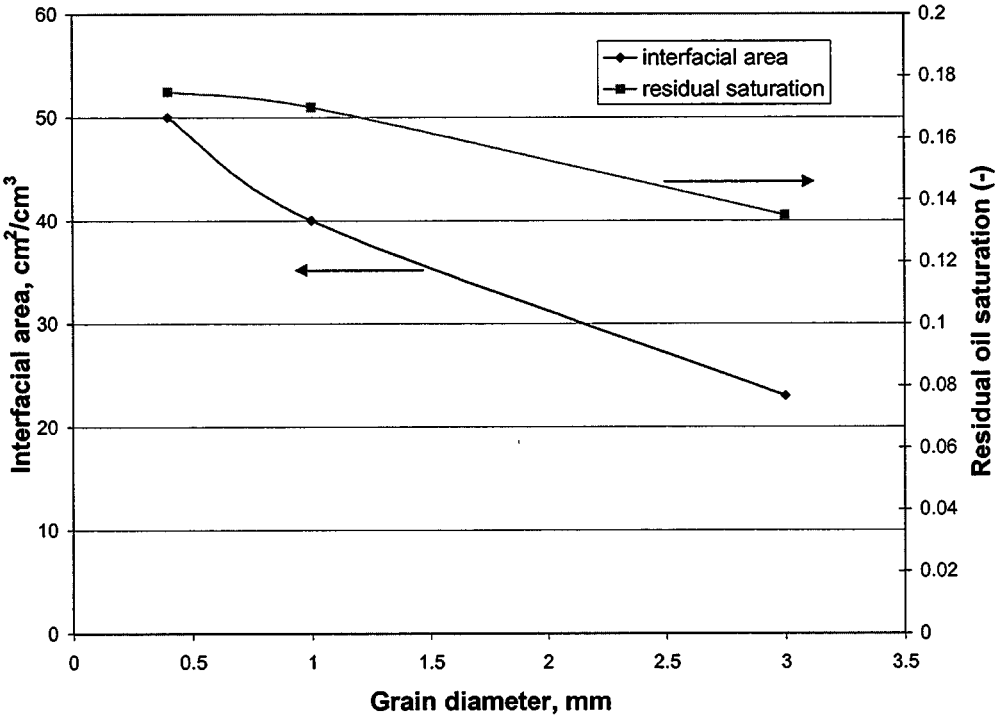

Figure 7.8 Change in interfacial area between water and decane at residual decane saturation as a function of glass bead size.

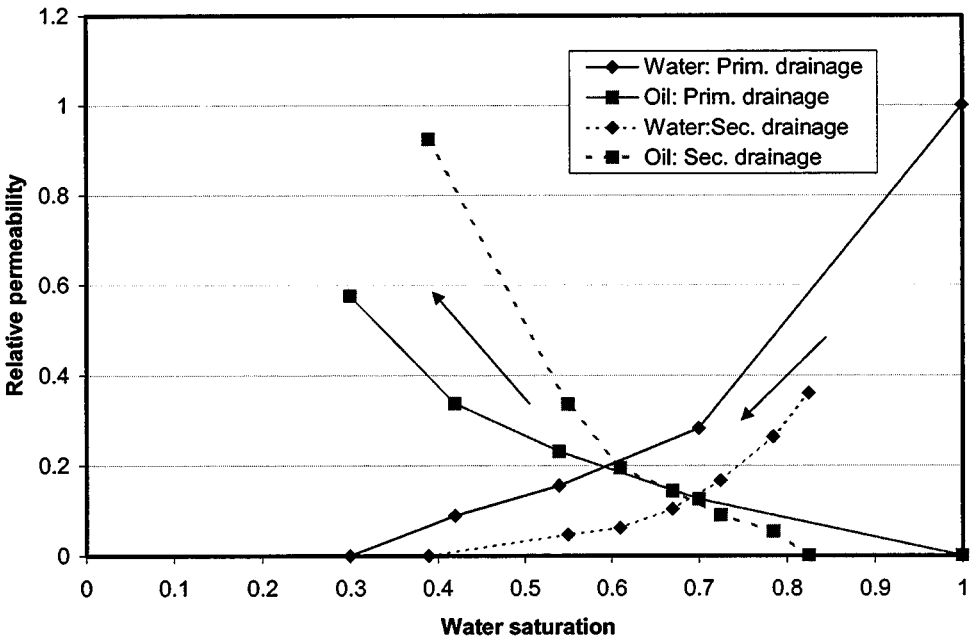

Figure 7.9 Relative permeability of water and decane as a function of saturation, measured in a column packed with water wet glass beads.

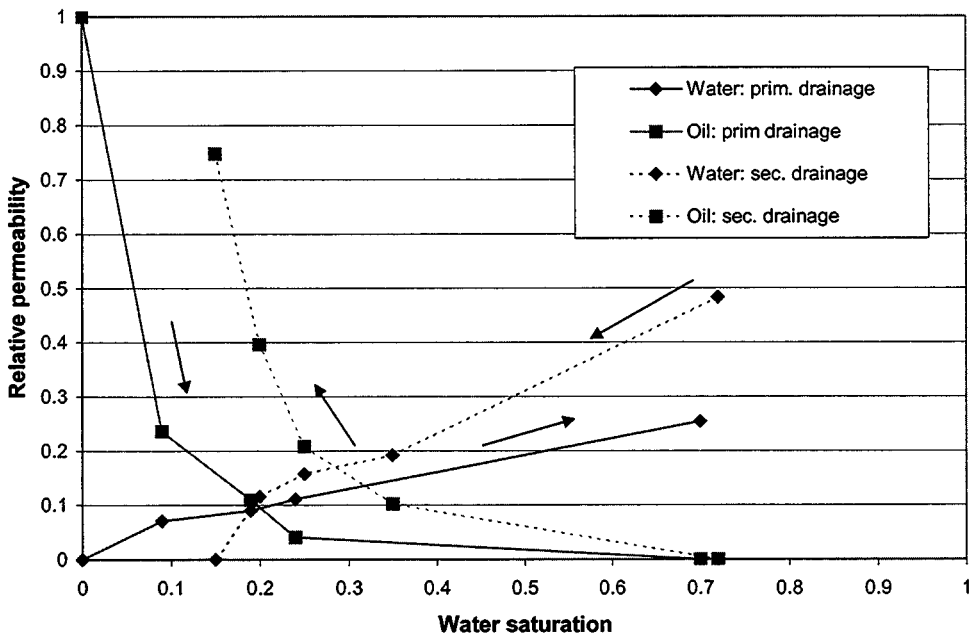

Figure 7.10 Relative permeability of water and decane as a function of saturation, measured in a column packed with oil-wet glass beads.

8. Using Transient Pressure Drop Measurements as an Indicator of Wettability

ABSTRACT

Core flood experiments were conducted on Berea sandstone to measure the transient pressure drop during drainage and imbibition in two-phase systems. Decane and 3% brine are used in the experiments. The pressure drop across water-wet core is measured, as a function of time and the data is history matched by a mathematical model. In the second phase of experiments, pressure drop across the cylindrical oil-wet core is measured at different time intervals and the data is history-matched by a mathematical model. The results of the history-match for both the water-wet and the oil-wet cases show a good fit. The relative permeability to oil and water can be obtained from the pressure drop transient by estimating the model parameters. A comparison of the water-wet and oil-wet pressure drop transients show a difference that can be used to characterize the wettability of a given rock.

INTRODUCTION

The relative permeability to oil and water in rocks is measured by experiments where the cylindrical rock core is flooded with the fluids. Often the experiments required to measure the relative permeability are very time consuming and require significant experimental setup. The proposed method of determining the relative permeability from transient pressure drop measurements provides a simple alternative to measuring the relative permeabilities and also gives us an idea of the effect of wettability on the flow characteristics. The proposed method takes advantage of the theoretical result where the pressure drop is derived analytically using the fractional flow theory and the constitutive equations for fluid flow in permeable media. The pressure drop across the core is related to the spatial integral of fractional flow and the relative permeability.

The relative permeability model assumed is a Corey exponent model where the relative permeability is an exponential function of the normalized saturation. The transient pressure drop across the core is dependent on the endpoint relative permeabilities and the exponent of the Corey model.

METHODOLOGY

Experiments were conducted on fluid flow through cylindrical cores, which were either oil wet or water wet (The details of the experimental sequence is presented in the next section). The pressure drop across the core was obtained with respect to time. Also the end point saturations were measured from the volumetric data collected during the experiments. This enables to determine the end point relative permeability for both the oil and the water phases. The flow rate and the dimensions of the cylinder are known quantities and therefore the only unknowns are the fractional flow and the relative permeabilities, both of which are functions of saturation. The relative permeability and the fractional flow are of course related and one could be obtained from the other. The fractional flow is therefore a generating function for relative permeability. The fractional flow can be obtained if we knew the exponents from the Corey model and also the endpoint saturation. The endpoint saturation is obtained from the experimental data on the cylindrical cores. However the exponents have to be obtained by an inverse procedure wherein a given value of exponent is assumed and the transient pressure drop curve is calculated. The calculated transient curve is then compared with the actual transient curve from the experiments and the exponents are continually adjusted to match the actual curve. This is nothing but an optimization procedure to find the best value of the exponents to fit the measured transient pressure drop curve. Therefore the measured pressure drop curves become generating functions for relative permeability curves.

EXPERIMENTAL METHODS

Fluids Used

The fluid systems (water/oil) were chosen with the objective of obtaining near equal mobility ratio displacement and also minimize pressure drop across the core. The aqueous phase used was brine (NaCl) at 3%v/v concentration. The oil phase used was decane.

Core Preparation

Two cylindrical cores (1 inch in diameter and 6 inches in length) were cut from a homogenous slab of Berea sandstone using tap water as the cutting fluid. The cores were dried in an air-oven at 100°C for at least 24 hours and then evacuated and saturated directly in the Hassler apparatus, which will later be used for the core flooding experiments. The

average core porosity was 21% and the absolute permeability was 132mD.

Berea sandstone in its original state is water-wet. To artificially render the cores oil-wet the cores were treated with a wettability altering agent, a 1% v/v solution of OTS (Octadecyltrichlorosilane). Details of the core treatment procedure are given in Appendix B.

Core flood experiments

Water-wet rock

The primary imbibition is conducted by saturating the core with brine situated in a burette. The saturation continues until there is no more change in the level of the burette. The amount of brine used to saturate the core is read from the burette and is used to calculate the porosity of the given core.

The primary imbibition is followed by a primary drainage where decane displaces the imbibed brine. Decane is injected using an ISCO pump at the same flow rate. The pressure drop is measured across the core periodically and the displaced brine is collected at the outlet of the core. The flooding is carried out for more than 25 pore volumes until the change in volume of brine collected is negligible. The residual saturation of brine is also calculated using a simple mass balance.

The primary drainage is followed by a secondary imbibition where brine is injected into the core from the same inlet using Beckman pump. The flow rate is maintained the same as and the pressure drop across the core is measured periodically. The displaced decane is collected at the outlet. Brine injection is performed for more than 25 pore volumes until the change in volume of decane collected is negligible.

Secondary drainage is carried out on the core by injecting decane at the same flow rate and the pressure drop across the core is recorded. The displaced brine is collected at the outlet to calculate the residual saturation of brine in the core.

Oil-Wet Rock

Two Berea sandstone cores A and B were made oil-wet by saturating them with OTS solution as described previously. Core A is saturated with decane during primary imbibition and followed by primary drainage, secondary imbibition and secondary drainage. The

pressure drop across the core is recorded periodically during each process and the displaced fluid is measured at the outlet to measure the residual saturation. Core B is imbibed (primary imbibition) with brine by evacuating the core and injecting brine using Beckman pump. The primary imbibition is followed by primary drainage where the imbibed brine is displaced by injecting decane using ISCO pump. The pressure drop across the core is measured and the volume of brine collected at the outlet is used to calculate the residual saturation.

RESULTS AND DISCUSSION

Figure 8.1 shows the pressure drop versus time data for primary drainage where decane is displacing the imbibed brine from the water-wet sandstone core. The Pressure drop achieves a peak value at breakthrough and subsequently flattens out at large pore volumes injected and is indicative of the occurrence of residual saturation. This pressure drop can be used to calculate the end point relative permeability of the core. The position of the peak of the curve depends on the fractional flow behavior of the fluids in the core and therefore indicative of the Corey exponents.

Similarly Figures 8.2 and 8.3 show the pressure drop history for secondary imbibition and secondary drainage. The pressure drop for secondary imbibition is high due to the wettability of the rock. For relatively water-wet rocks the flow of brine faces more resistance from the permeable media than does the oil flow.

Figures 8.4,8.5 and 8.6 show the primary drainage, secondary imbibition and the secondary drainage for the case of oil-wet Core-A. Note that the three curves are similar to the trends observed for the same processes in a water-wet curve. This is because the flow of a wetting fluid faces more resistance than a non-wetting fluid in permeable media irrespective of whether the fluid is oil or brine.

The Figures 8.7, 8.8 and 8.9 show the primary drainage where brine is imbibed rather than decane (unlike Core-A), secondary imbibition where decane replaces imbibed brine (unlike Core-A) and the secondary drainage where brine replaces decane (unlike Core-A) for an oil wet Core-B. The purpose of this inverse configuration of fluids is to enable comparison of two the pressure drop profiles for rocks, which differ only in wettability.

Figures 8.7, 8.8 and 8.9 show the comparison of the primary drainage curves between oil-wet

(Core-B) and water-wet cores. There is a large difference in the end point pressure drops between the two and this indicates the difference in wettability of the cores. Similarly there is a large difference in the end-point pressure drops between the oil-wet and water-wet cores for secondary imbibition and secondary drainage processes.

MATHEMATICAL MODEL AND SIMULATION

A mathematical model is proposed to describe the multi-phase fluid flow in the core and a relationship has been established between the Saturation and the distance along the flow in the core and also between pressure drop across the core and the time elapsed from injection of displacing fluid. The derivation of these relationships are discussed in the Appendix A. A numerical routine was created using Microsoft Excel Macro Programming to automatically history match the pressure history curves and obtain the Corey exponent factors.

RESULTS FROM SIMULATION

Figures 8.10 and 8.11 show the effect of Corey exponents and the Mobility ratio on the shape of the pressure drop history for a Berea sandstone core. The shapes show large sensitivity to the Corey exponents and the Mobility ratio. The effect of equal mobility ratio and piston like displacement is also shown.

Figures 8.12 and 8.13 show the history match of the experimental pressure drop data for a water-wet Berea sandstone core (secondary imbibition and secondary drainage). The Corey exponent parameters, which were estimated using the numerical history match routine, are listed in Table 8.1. Figures 8.14 and 8.15 show the theoretical simulation of the pressure drop history for the secondary imbibition process and secondary drainage process in an oil-wet core. The relative permeability curves for water-wet and oil-wet cores obtained are shown in Figures 8.16 and 8.17.

CONCLUSIONS

The studies have shown that the pressure drop measurements across the core during core flooding provides a way to calculate the relative permeabilities. The method to calculate the relative permeabilities is simple and may be less time consuming than the conventional techniques using centrifuges. The above method however needs to be substantiated by

calculating the relative curves for the same core by collecting the displaced fluids and computing the fractional flow curves simultaneous to pressure drop measurement. The change in wettability of rock leads to change in the pressure drop history curves, which means the pressure drop data also can provide valuable information regarding the wettability of a given rock material.

REFERENCES

1. Larry, Lake. W., *Enhanced Oil Recovery*, New Jersey, Prentice-Hall, 1989.
2. Johnson, E. F., Bossler, D. P., and Naumann, V. O., "Calculation of Relative Permeability from Displacement Experiments," *Journal of Petroleum Technology*, (January 1959) 61-63, *Transactions of the American Institute of the Mechanical Engineers,* 265.

Appendix A

Derivation of equation describing the saturation distribution and pressure drop in a one-dimensional two-phase immiscible displacement (oil displacing brine)

Constitutive equations (for any number of dimension):

Mass conservation equation equations:

$$\frac{\partial W_i}{\partial t} + \vec{\nabla} \cdot \overrightarrow{N_i} = R_i$$

$$W_i = \phi \sum_{j=1}^{Np} \rho_j S_j \omega_{ij} + (1-\phi)\rho_s \omega_{is}$$

$$\overrightarrow{N_i} = \sum_{j=1}^{Np} \left(\rho_j \omega_{ij} \overrightarrow{u_j} - \phi \rho_j S_j \overrightarrow{\overrightarrow{K_{ij}}} \cdot \overrightarrow{\nabla \omega_{ij}} \right)$$

$$u_j = -\lambda_{rj} \vec{\vec{k}} \cdot \left(\overrightarrow{\nabla p_j} + \rho_j \vec{g} \right)$$

$$p_j - p_n = p_{cjn}(S, \omega, x)$$

S_i - Saturation in phase i

ω_{ij} - Mass fraction of species i in j

ρ_i - Density of phase i

$\overrightarrow{\overrightarrow{K_{ij}}}$ - Dispersion tensor

$\vec{\vec{k}_{ij}}$ - Permeability tensor

p_i - Pressure in phase i at a given location

ϕ - Porosity of the permeable medium

p_c - Capillary pressure between two phases

Np - Number of phases(=2)

R_i - Reaction in phase i (=0)

Consider a one-dimensional flow and neglecting the effect of gravity and adsorption. Since the two phases are immiscible we have,

$\omega_{oo} = 1$

$\omega_{wo} = 0$

$\omega_{ww} = 1$

$\omega_{ow} = 0$

and making $u_i = uf_i$, where f_i is the fractional flow of phase i, we get,

$$\phi \frac{\partial S_o}{\partial t} + u \frac{\partial f_o}{\partial x} = 0$$

$$\phi \frac{\partial S_w}{\partial t} + u \frac{\partial f_w}{\partial x} = 0$$

Solving one of the above equations by method of characteristics give the saturation distribution of both the phases.

Therefore we solve for the oil phase saturation distribution.

$$X|_{So} = \frac{qt}{A\phi} \frac{\partial f_o}{\partial S_o}$$

The fractional flow derivative in the above equation can be estimated analytically by assuming a relative permeability model. In this case we assume the Corey model as detailed below.

$$k_{ro}\left(\overline{S_o}\right) = k_{ro}{}^{\max} \overline{S_o}^{no}$$

$$k_{rw}\left(\overline{S_o}\right) = k_{rw}{}^{\max} \left(1 - \overline{S_o}\right)^{nw}$$

where $\overline{S_o} = \dfrac{S_o - S_{or}}{1 - S_{or} - S_{wr}}$

We know that fractional flow is given by,

$$f_o = \frac{\frac{k_{ro}\mu_o}{\mu_w k_{rw}}}{1 + \frac{k_{ro}\mu_o}{\mu_w k_{rw}}}.$$

Substituting for the relative permeability expressions and after algebraic manipulations we get,

$$f_o = \frac{M_o \overline{S_o}^{no}}{\left(1-\overline{S_o}\right)^{nw} + M_o \overline{S_o}^{no}}$$

Where M_o is called the mobility ratio of oil and is given by,

$$M_O = \frac{k_{ro}^{max}\mu_w}{\mu_o k_{rw}^{max}}.$$

Writing equation for saturation distribution as,

$$X|_{So} = \frac{qt}{A\phi}\frac{\partial f_o}{\partial \overline{S_o}}\frac{\partial \overline{S_o}}{\partial S_o}$$

and after substituting for the derivatives we get,

$$X|_{So} = \frac{qt}{A\phi}\frac{M_o \overline{S_o}^{no-1}\left(1-\overline{S_o}\right)^{nw-1}\left[no+\overline{S_o}(nw-no)\right]}{\left[\left(1-\overline{S_o}\right)^{nw} + M_o \overline{S_o}^{no}\right]^2}\frac{1}{(1-S_{or}-S_{wr})}$$

From the above, after assuming suitable values of exponents and residual saturations, we can determine the saturation distribution with respect to distance and also time. However the above solution gives triple valued result for saturation, which can be corrected by doing a material balance around the displacing front.

The position of the displacing oil front, $X|_{sof}$ is given by solving for $\overline{S_{of}}$ from the equation,

$$\frac{M_o \overline{S_{of}}^{no-1}\left(1-\overline{S_{of}}\right)^{nw-1}}{\left[\left(1-\overline{S_{of}}\right)^{nw} + M_o \overline{S_{of}}^{no}\right]^2} = \frac{M_o \overline{S_{of}}^{no}}{\left[\left(1-\overline{S_{of}}\right)^{nw} + M_o \overline{S_{of}}^{no}\right]\left(\overline{S_{of}} + \frac{S_{or}}{(1-S_{or}-S_{wr})}\right)}$$

The pressure drop in the permeable medium is then given by,

$$\Delta p = \frac{q\mu_o}{kA}\int_0^{X_{sof}} \frac{f_o}{k_{ro}}dx + \frac{q\mu_w}{kA}\int_{X_{sof}}^{L} \frac{f_w}{k_{rw}}dx$$

Table-8.1 Calculated relative permeabilities, residual saturation and Corey exponents.

	Water Wet		Oil Wet	
k^o_{ro}	0.73		0.061	
k^o_{rw}	0.091		0.568	
S_{or}	0.303		0.266	
S_{wr}	0.4		0.413	
n_o	1.5	2.4	2	2.8
n_w	2.2	2	3	2
	*	**		

* -Calculated from the experimental transient pressure drop data for brine displacing decane (secondary imbibition).

** -Calculated from the experimental transient pressure drop data for decane displacing brine (secondary drainage).

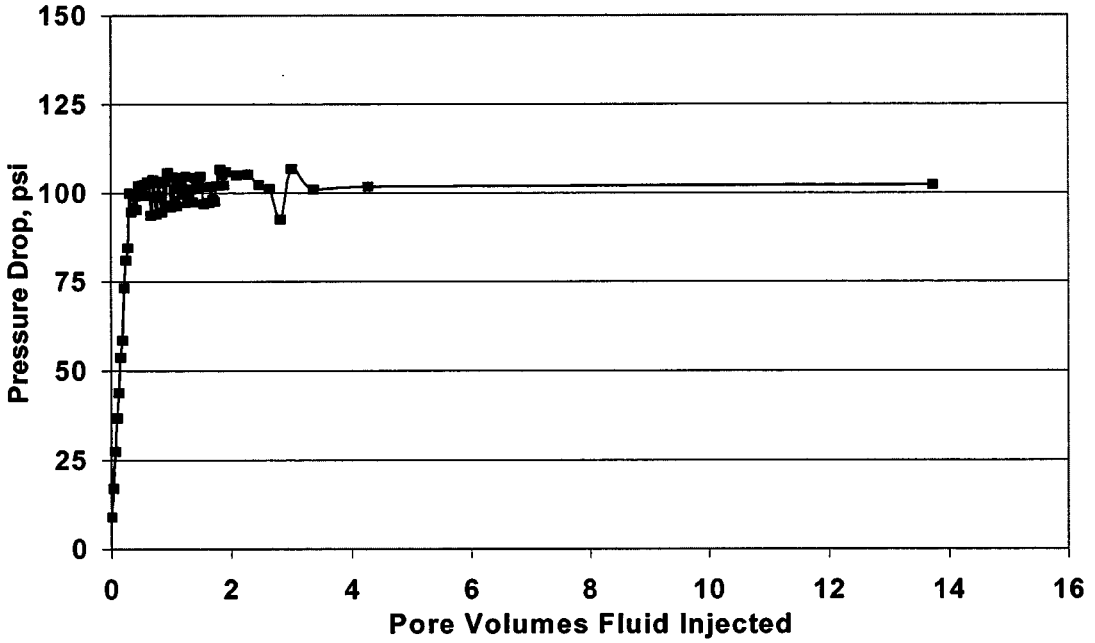

Figure 8.1 History of pressure drop across core for water-wet Berea sandstone (primary drainage, decane displacing brine).

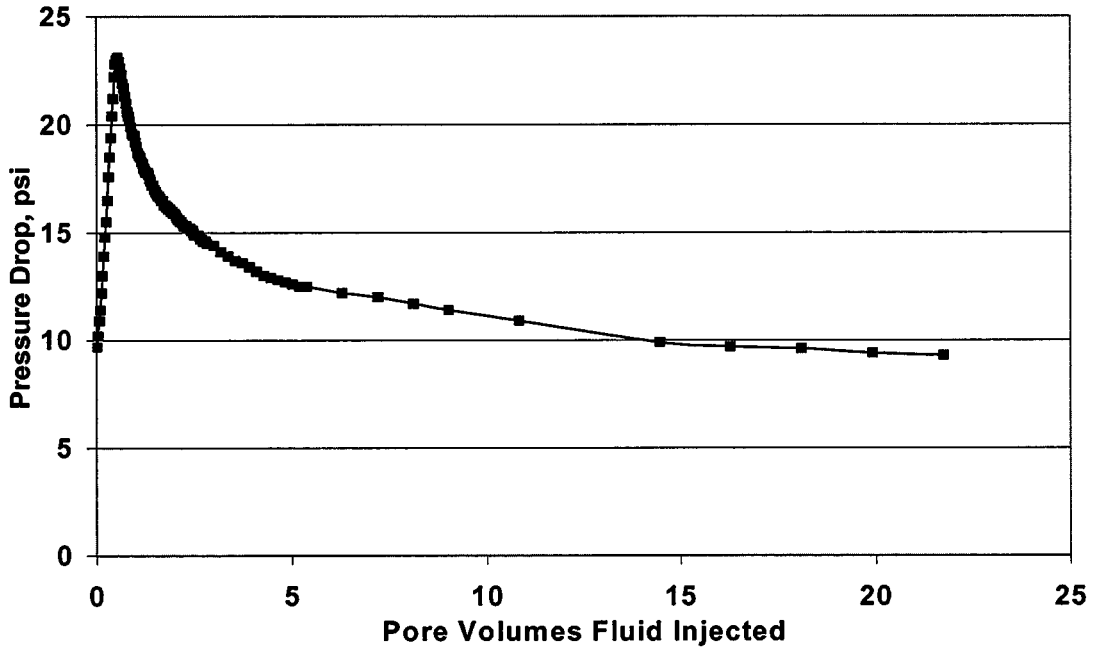

Figure 8.2 History of pressure drop across core for water-wet Berea sandstone (secondary imbibition, brine displacing decane).

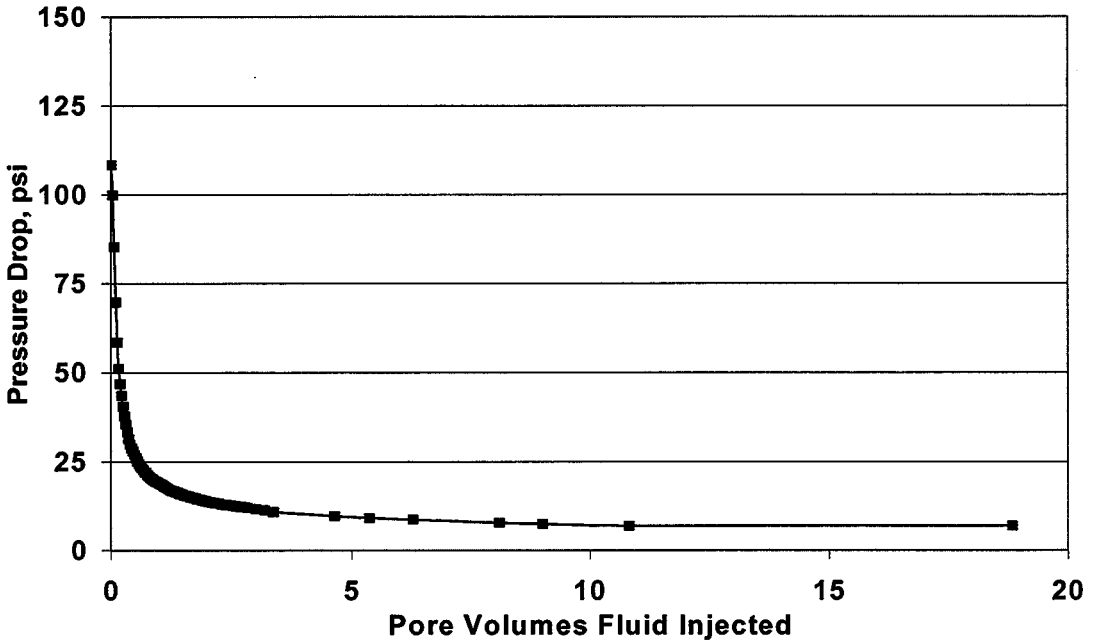

Figure 8.3 History of pressure drop across core for water-wet Berea sandstone (secondary drainage, decane displacing brine).

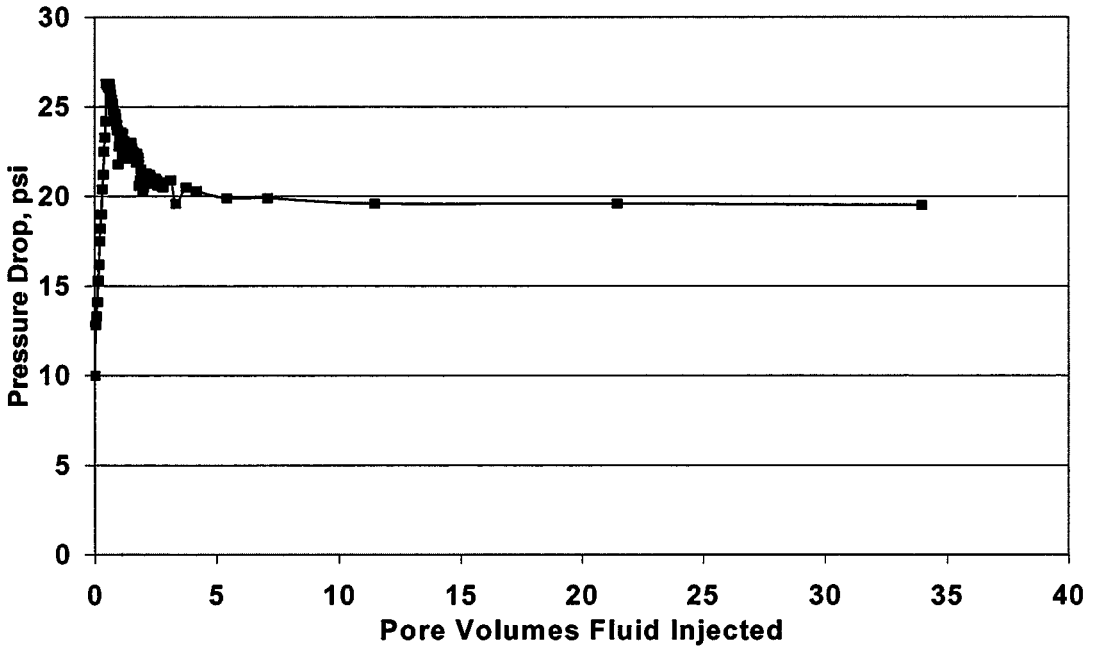

Figure 8.4 History of pressure drop across core for oil-wet (Core-A) Berea sandstone (primary drainage, brine displacing brine).

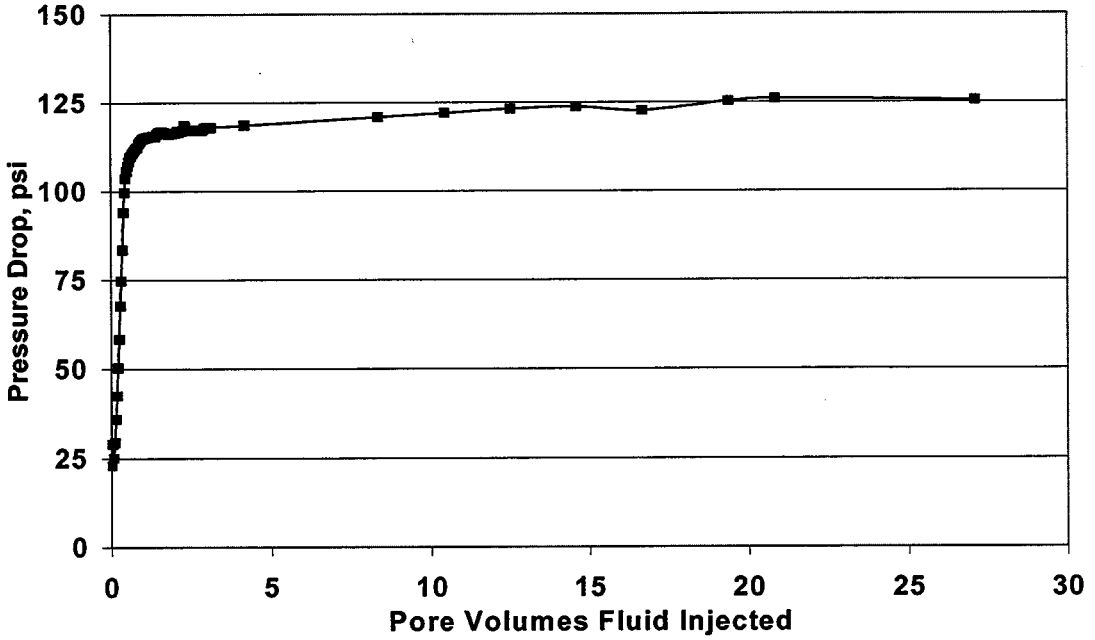

Figure 8.5 History of pressure drop across core for oil-wet (Core-A) Berea sandstone (secondary imbibition, decane displacing brine).

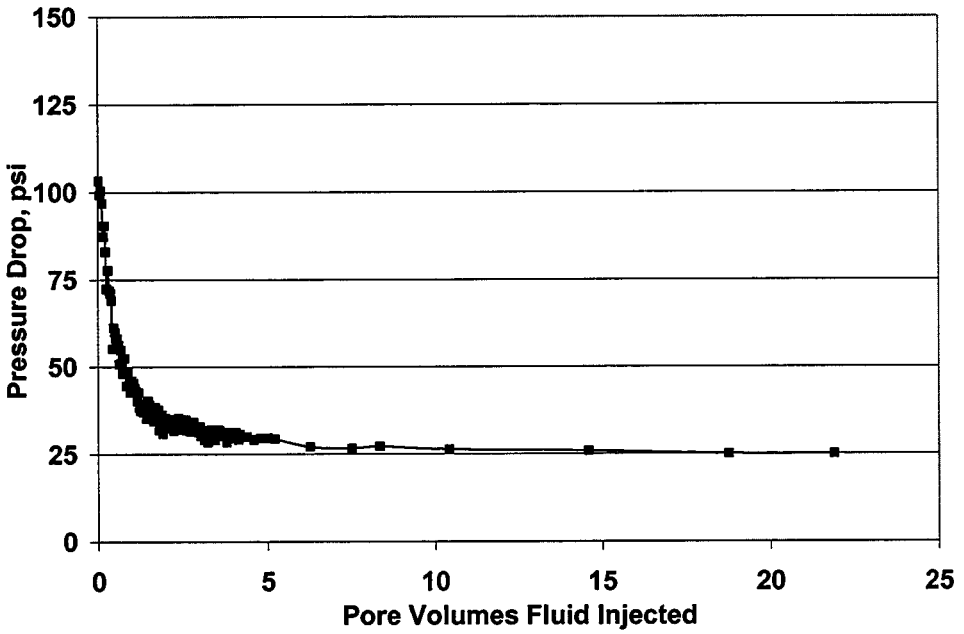

Figure 8.6 History of pressure drop across core for oil-wet (Core-A) Berea sandstone (secondary drainage, brine displacing decane).

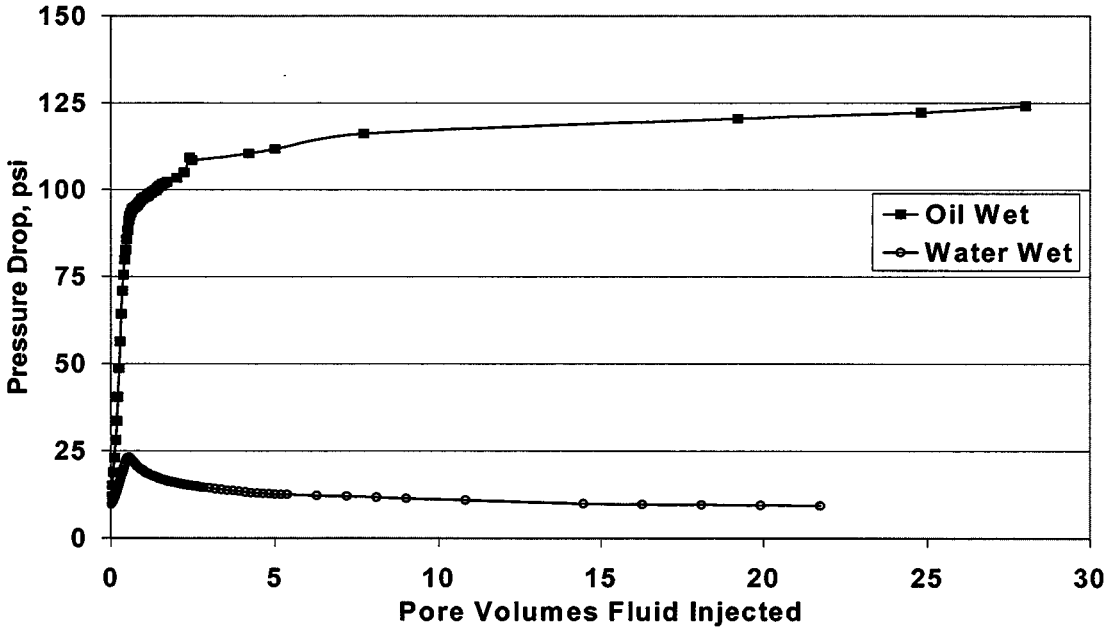

Figure 8.7 Comparison of pressure drop (across the core) history of oil-wet (Core-B) and water-wet cores (decane replacing brine).

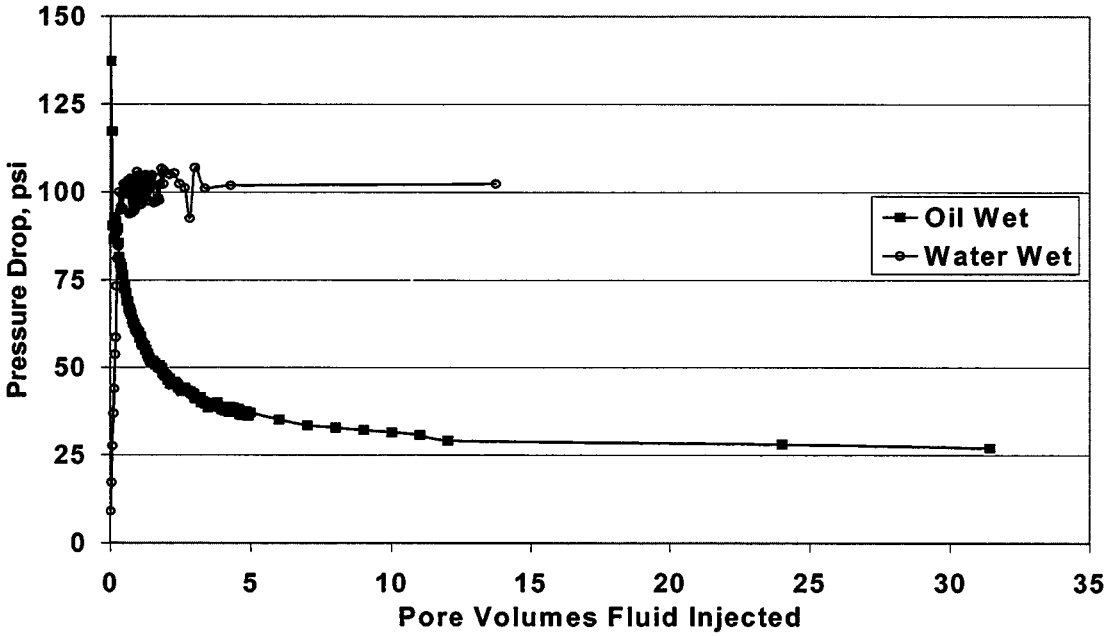

Figure 8.8 Comparison of pressure drop (across the core) history of oil-wet (Core-B) and water-wet cores (brine displacing decane). The core is initially at residual water saturation.

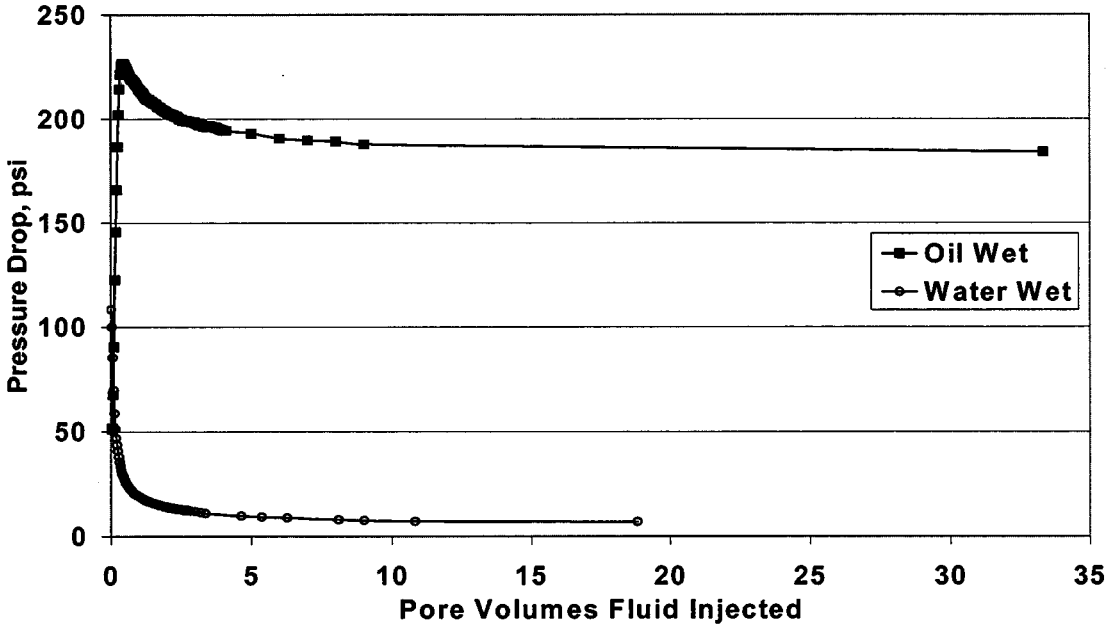

Figure 8.9 Comparison of pressure drop (across the core) history of oil-wet (Core-B) and water-wet cores (decane displacing brine). The core is initially at residual decane saturation.

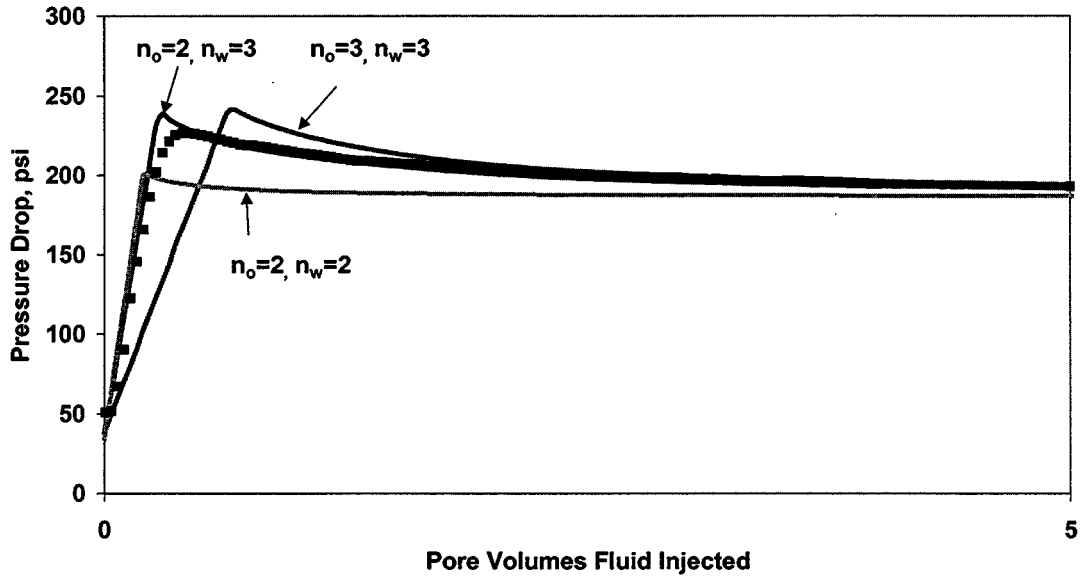

Figure 8.10 Effect of Corey exponents on pressure drop history of oil-wet (Core-A, decane displacing brine). The core is initially at residual decane saturation. The points represent the experimental data.

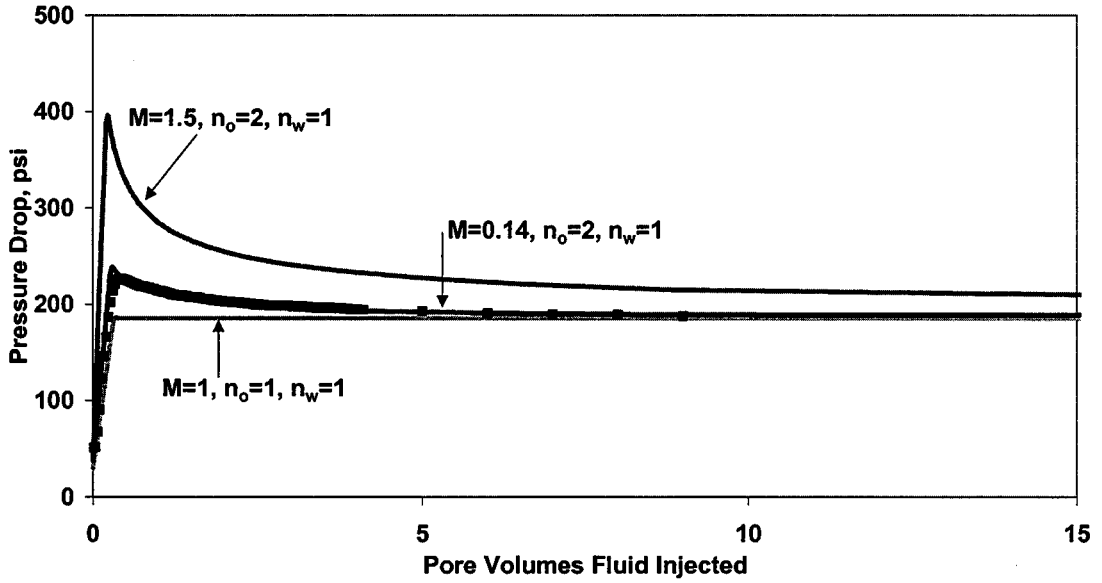

Figure 8.11 Effect of Mobility ratio on pressure drop history of oil-wet (Core-A, decane displacing brine). The core is initially at residual decane saturation. The points represent the experimental data.

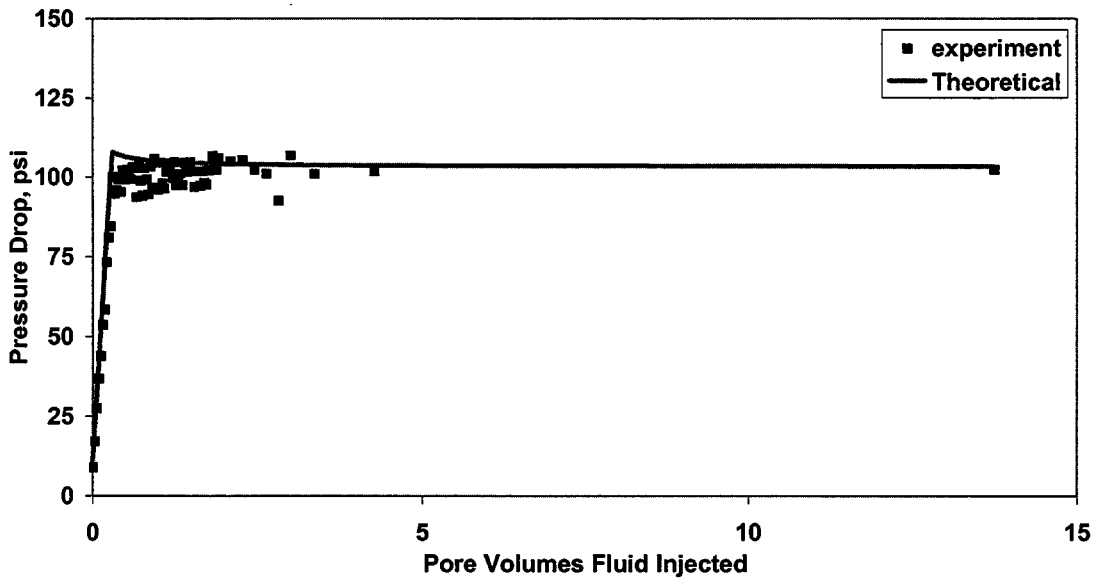

Figure 8.12 History match of secondary imbibition pressure (brine displacing decane) drop data (water-wet core).

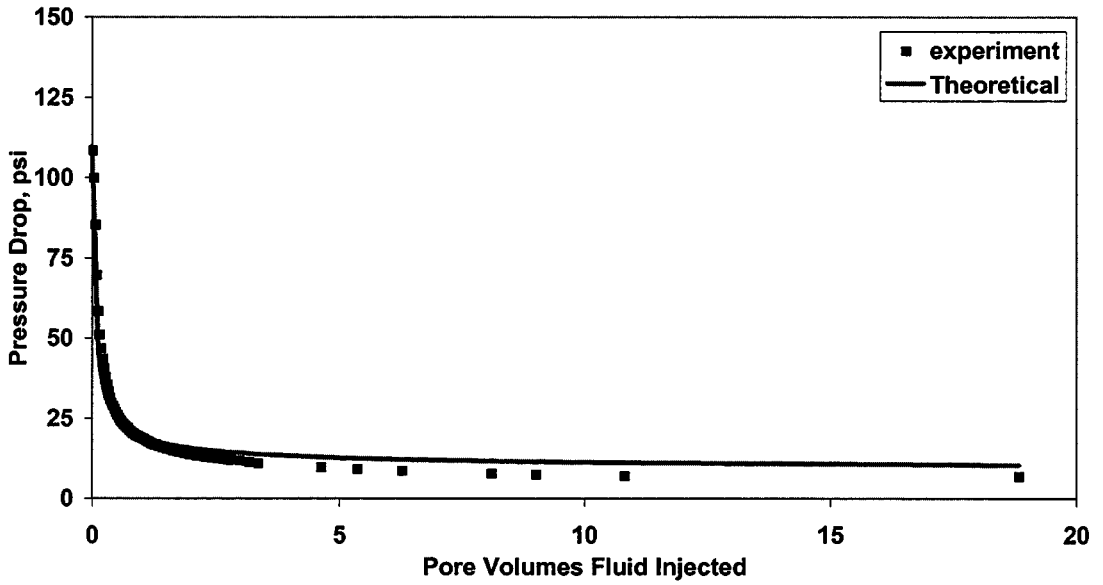

Figure 8.13 History match of secondary drainage pressure drop data (water-wet core).

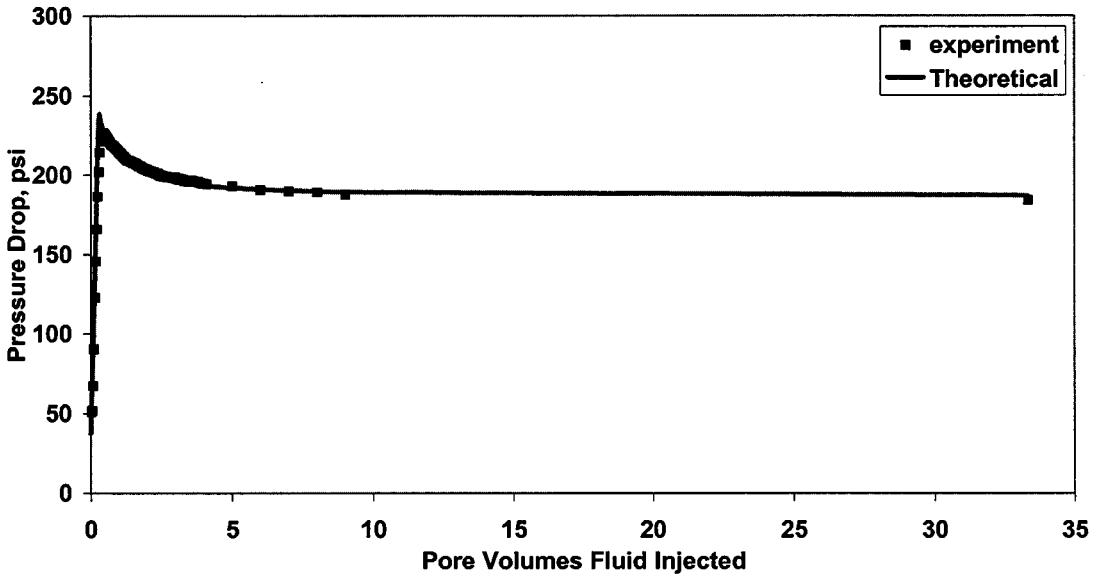

Figure 8.14 History match of secondary imbibition pressure drop data (oil-wet Core-A).

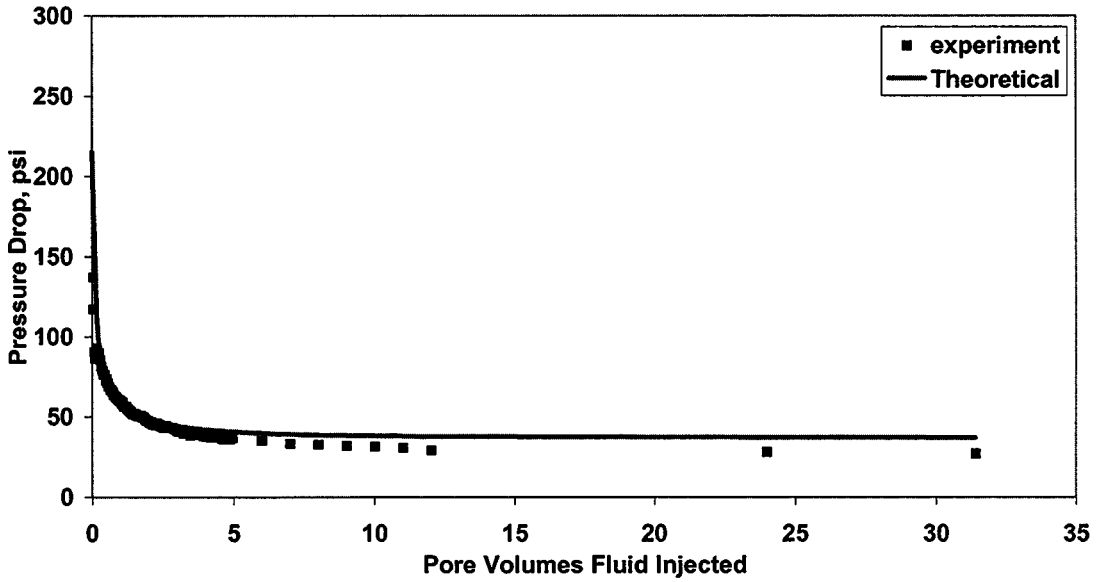

Figure 8.15 History match of secondary imbibition pressure drop data (oil-wet Core-A).

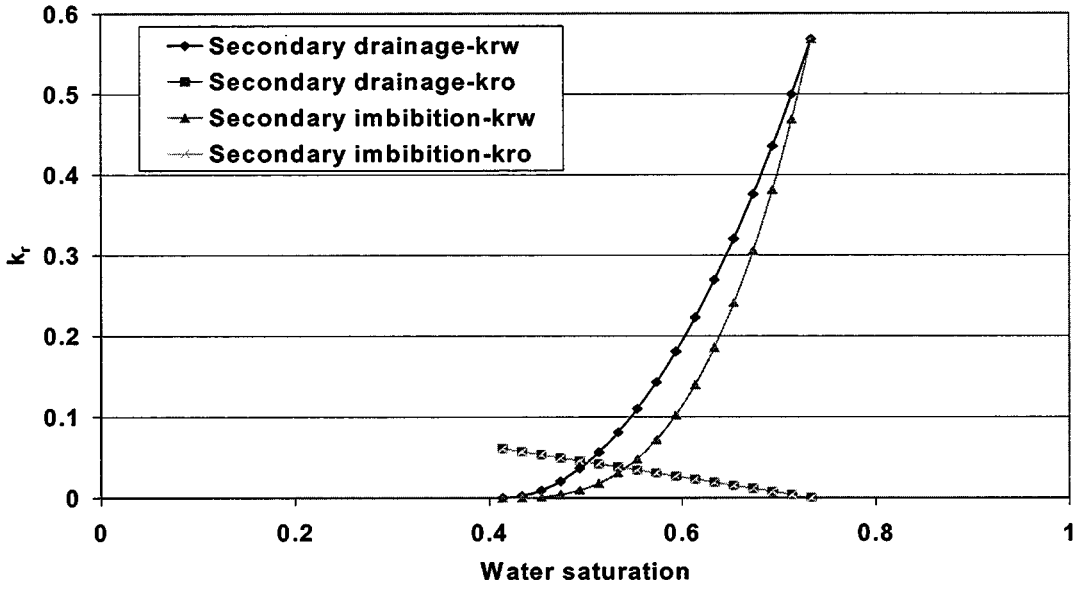

Figure 8.16 Oil-water relative permeability for oil-wet core.

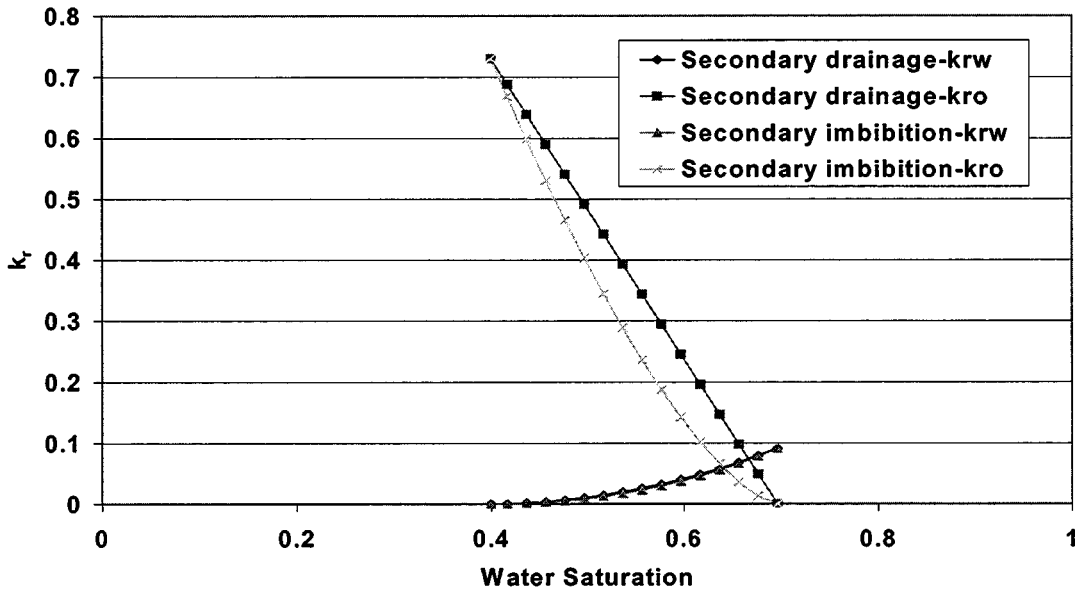

Figure 8.17 Oil-water relative permeability for water-wet core. These curves were generated by using end point relative-permeability, residual saturation and Corey exponents obtained by history matching the experimentally measured pressure drop profiles and residual saturation.